Studying Global and Local Star Formation Processes with Young Massive Stars in NGC 6946

Debby Tran

A dissertation
submitted in partial fulfillment of the
requirements for the degree of

Doctor of Philosophy

University of Washington

2024

Reading Committee:
Benjamin Williams, Chair
Emily Levesque, Chair
Jessica Werk

Program Authorized to Offer Degree:
Astronomy

University of Washington

Abstract

Studying Global and Local Star Formation Processes with Young Massive Stars in NGC 6946

Debby Tran

Co-Chairs of the Supervisory Committee:
Benjamin Williams
Astronomy

Emily Levesque
Astronomy

I analyze resolved near-ultraviolet (NUV) stellar photometry of star-forming galaxy NGC 6946 (The Fireworks Galaxy) taken with the Hubble Space Telescope's (HST) Wide Field Camera 3 (WFC3) with F275W and F336W filters to put new constraints on the relationships between the spatial distribution of ages, formation rate, masses, colors, and luminosity for massive stars and massive star clusters. In Chapter 2, we observe a correlation between age and density in the spiral arms and test diagnostics for star formation rate (SFR) and whether they are consistent with the unusually high observed rate of supernovae (10 in the past century). In Chapter 3, I modify a computer-vision algorithm to automate cluster candidate finding and produce a cluster and association candidate catalog. I measure the luminosity, effective radius, and color of each of the candidates. With the catalog obtained in Chapter 3, in Chapter 4, I constrain the cluster mass-radius relation and mass function of clusters. We measure the age of the clusters and determine the cluster formation efficiency of NGC 6946. We will publicly release this new clustering algorithm to the community and this observational data enabling detailed comparisons to numerical simulations. In Chapter 5, my future work, I discuss my progress and plans to measure an additional 13 bands ($\sim$200 visits) of archival optical and infrared (IR) HST WFC3 and Advanced Camera for Surveys (ACS)

photometry of individual stars and clusters covering some areas in NGC 6946. With the planned stellar photometry catalog, I will fit spectral energy distributions (SEDs) for over 8 million stars in NGC 6946 to investigate how local environments and large scale mechanisms influence the formation of stars.

TABLE OF CONTENTS

LIST OF FIGURES

LIST OF TABLES

ACKNOWLEDGMENTS

I cannot fully express my immense gratitude to everyone who's loved me into being, who has gotten me to where I am today, who has stood by and supported me. The acknowledgements listed here are just a fraction of what I wished I had the words to express. Before reading my acknowledgements, I would love for you to humor me in following in the footsteps of Mister Roger's Lifetime Achievement Awards acceptance speech. (Look it up if you haven't watched it before! It's worth it!) Each one of us has a community and loved ones who have gotten us to where we are today, both those who are with us now or have passed. I would like for you to take 10 seconds to think of being who has loved, supported, and cherished you. If you can, please let them know and show your appreciation for the wonderful impact they've made in your life. Life is too short for us to keep that to ourselves.

In roughly chronological order, I want to thank the people who have helped me get to this point in my academic journey, starting with my undergrad research advisor, Quinn Konopacky. I am so grateful to have worked with you as an undergrad at UC San Diego. Not only did my research experience teach me how to code, but you guided me through how to debug, present, and learn more as a researcher. I will forever be appreciative of the mentorship you provided me and have tried to do the same for others since then. To Shelley Wright, you were my favorite professor in undergrad. I learned so much about instrumentation, how light and telescopes work, and how to translate a research question into a plan for observation and further into information. Despite how exhausted I constantly was in undergrad, the knowledge that I've gained from you and your observation class has stuck so well in my mind because of your excellent teaching and helped me understand so much about why we astronomers do the things the way we do.

To the folks at the Washington Nanofabrication Facility, in particular, Mark Morgan, Mark Brunson, Derek Baker, Sarice Jones, Jean Nielsen, David Nguyen- thank you for giving me your time and expertise on my simple and yet weirdly hard project. All of you have been so wonderful, understanding, and supportive about this astronomy interloper at the facility who knew nothing about nanofabrication. It has been amazing to use all these cool tools, watch plasma and lasers work, sweat profusely in a clean room suit, and chat with each of you. I was so nervous the first time I used each of the tools, I genuinely thought I'd either break everything I touched or spill a bunch of random chemicals in the facility. The confidence that y'all have in working with the equipment and understanding that things just happen sometimes, has been so comforting in what felt very high-stakes. It's something I continue to admire, and strive to become better at. Kal Kadlec and Rishi Pahuja, thank you so much for going through the adventures of retrofitting KOSMOS with me.

To my committee- Ben Williams and Emily Levesque, I know you hear this all the time, but I'm so grateful to have done my dissertation with y'all. Ben, I appreciate how much guidance you've given me throughout the time we've worked together. Whenever I've been really stuck on a debugging issue, you've been so good about walking through the steps on how to solve the problem and suggesting different things to try. I definitely get very focused on trying to solve one thing, when in the bigger picture, it could be helpful to look at something else and zoom out to the bigger picture. Emily, thank you for making navigating the many hurdles of paperwork and the bureaucratic nonsense of academia a little easier.

Jess and Monika, thank you so much for taking the time out of your busy schedules to be on my committee. Jess- in particular! I appreciate so much how you were so willing to step in the last minute on the night before my general exam to substitute when another committee member couldn't make it due to an emergency.

Thank you to the staff at the main office who have kept everything running, particularly Tyneshia Valdez, Elisa Quintana, Ashley Detert, and Jess Ness.

To the anonymous reviewers who've read my papers, I appreciate you all so much - you've taken my writing and made it ten million times better.

I cannot fully express my immense gratitude to everyone who's loved me into being, who has gotten me to where I am today, and who has stood by and supported me. The acknowledgments listed here are just a fraction of what I wished I had the words to express. Before reading my acknowledgments, I would love for you to humor me in following in the footsteps of Mister Roger's Lifetime Achievement Awards acceptance speech. (Look it up if you haven't watched it before! It's worth it!) Each one of us has a community and loved ones who have gotten us to where we are today, both those who are with us now or have passed. I would like for you to take 10 seconds to think of being who has loved, supported, and cherished you. If you can, please let them know and show your appreciation for the impact they've made in your life. Life is too short for us to keep that to ourselves.

In roughly chronological order, I want to thank the people who have helped me get to this point in my academic journey, starting with my undergrad research advisor, Quinn Konopacky. I am so grateful to have worked with you as an undergrad at UC San Diego. You also guided me through how to debug, present, and uncover more as a researcher. I will forever appreciate your mentorship and have tried to do the same for others since then. To Shelley Wright, you were my favorite professor as an undergrad. I learned so much about instrumentation, how light and telescopes work, and how to translate a research question into a plan for observation and further analysis. Despite how exhausted I was in undergrad, the knowledge I've gained from you and your observation class has stuck so well in my mind. Your excellent teaching helped me understand why astronomers do things the way we do.

To the folks at the Washington Nanofabrication Facility: Mark Morgan, Mark Brunson, Derek Baker, Sarice Jones, Jean Nielsen, and David Nguyen- thank you for giving me your time and expertise on my simple and yet weirdly challenging project. All of you have been so understanding and supportive of this astronomy interloper at the facility who knew nothing

about nanofabrication. It has been amazing to use all these tools, watch plasma and lasers work, sweat profusely in a clean room suit, and chat with each of you. I was so nervous the first time I used each tool, I genuinely thought I'd either break everything I touched or spill a bunch of random chemicals in the facility. The confidence that y'all have in working with the equipment and understanding that things happen, has been so comforting in what felt very high-stakes. It's something I continue to admire and strive to become better at. Kal Kadlec and Rishi Pahuja, thank you so much for going through the adventures of retrofitting KOSMOS with me.

To my committee- Ben Williams and Emily Levesque, I know you hear this all the time, but I'm so grateful to have done my dissertation with y'all. Ben, I appreciate how much guidance you've given me throughout the time we've worked together. Whenever I got stuck on a debugging issue, you've been so good about walking through the steps of solving the problem and suggesting different things to try. I get hyperfocused on trying to solve a singular problem, and you helped me zoom out to see the bigger picture. Emily, thank you for making navigating the many hurdles of paperwork and the bureaucratic nonsense of academia a little easier.

Jess and Monika, thank you so much for taking the time out of your busy schedules to be on my committee. Jess- in particular! I appreciate how you stepped in at the last minute on the night before my general exam to substitute when another committee member couldn't make it due to an emergency.

Thank you to the staff at the main office who have kept everything running, particularly Tyneshia Valdez, Elisa Quintana, Ashley Detert, and Jess Ness.

To the anonymous reviewers who've read my papers, I appreciate you all so much - you've taken my writing and made it ten million times better.

Thank you to the Space Telescope Science Institute for awarding me the Hubble Archival Grant - this was my first time writing a grant proposal. I appreciate the confidence and

willingness to take a risk on my very ambitious research ideas and plans.

To the collaborators who have helped me throughout my thesis work, Margaret Lazzarini, O. Grace Telford, Brad Koplitz, Zhuo Chen, Tobin Wainer, Cliff Johnson, and Anil Seth: thank you so much for taking the time out of your busy schedules to help support me and our work together.

To the folks I worked with as undergrads, Ali Jones and Emerson W. Bowles. Thank you so much for trusting me to mentor you!

UW Astrograds - you all know I love y'all. I appreciate the support and friendship that you have given me in this community. Special shout out to the Graduates of Color in Astronomy and Physics who have made me feel less alone in grad school - thank you especially to Myles McKay for getting all of us together to have Chill Lunch. Thank you, y'all, for existing. Natalie Nicole Sanchez, Samantha Gilbert, and V Hurtado-Urrutia - thank you for being my awesome office mates.

To my accountabilibuds - Michelle Hu, Kayla Chun, Boeun Choi, Sam Garza, Lupita Mendoza Tovar, Brianna McKay, Myles McKay, Dino Bektesevic, Miles Currie. Thank you for consistently working and writing with me. The accountability sessions have been essential to this dissertation.

Thank you to UAW 4121! It is really hard to be a graduate student due to the many unnecessary hurdles in academia. You all made it feel like I wasn't being unreasonable to ask to be treated fairly. Thank you for helping us exist as humans during graduate school.

To my broader community in Washington State, specifically, the Washington Trails Association (Barbara, Meg, Judy - my wonderful teachers and mentors!!), VietQ, South King County and Eastside Mutual Aid, and Super Familia. I'm so lucky to have been in community with all of y'all and to work alongside you. It's been an honor to serve y'all and be supported by y'all. Gracias, obrigado, cảm ơn!

Thank you to the Duwamish, Tongva, and Kumeyaay people who, for thousands of years,

are and have been in relationship with the land I live/have lived on. My family has been unwelcome guests as refugees in the lands they've cared for, and I'm so grateful to be here. However, my ability to exist in their traditional lands is due to the many atrocities that were and continue to be committed against indigenous peoples: e.g. genocide, residential schools, kidnapping of children, destruction of culture, and the disappearing and murder of indigenous women. The least I can do is to continue to fight settler colonialism here and around the world. For those living on Duwamish lands, please join me in paying rent to Real Rent Duwamish or donate directly to the Duwamish Tribal Services and mutual aid funds to support the Duwamish people. The Tongva Taraxat Paxaavxa Conservancy is the first (of hopefully many more) plot of land to be returned to the original people of Los Angeles - please support their work to rematreate the land to the Tongva people. To stand against the same colonial violence happening across the world, support the BDS movement in boycotting and divesting from companies supporting Israel and the genocide of the Palestinian people. Please also support the (as I write this) several fundraisers to raise money for families in Palestine trying to escape before it is too late for them. For those in King County, please support the refugees from Congo, Angola, and Venezuela in getting safe housing. Follow South King County and Eastside Mutual Aid for more information.

Thank you to everyone (Dani Shapiro, Tolu Taiwo, Angela Lin, Michelle Hu, Diana Windemuth, Elijah Marrone, Neesha Pinnaduwage, Al Snow, Boeun Choi, Ash Rezai, Reanna Liaw, Tor Shimizu, Ricky Hougland, Hannah Bish, Vic Ly, Nicel Mohamed-Hinds, Audrey Kan, Brianna McKay, Myles McKay, Samantha Gilbert, and Tran Ton Nu) who has fed me and kept me alive through the last few weeks of my dissertation. There were a few months when I was not eating lunch or dinner and wouldn't eat unless I felt obligated to. I would not have made it to the point where you could read these words without you.

My friends, every one of you has made me a better person than I was when you met me. You all are full of love, kindness, laughter, and compassion, and have taught me to

be kind and patient with myself. I am so lucky to be your friend. In roughly alphabetical order: Al Snow, Alice Hsu, Angela Lin, Ash Rezai, Bethlee Lindor, Boeun Choi, Brianna McKay, Dani Shapiro, Diana Windemuth, Elijah Marrone, Hannah Bish, Kathyrn Neugent, Kayla Chun, Lauryn Williams, Lupita Tovar Mendoza, Makayla Wright, Michelle Hu, Myles McKay, Neesha Pinnaduwage, Nicel Mohamed-Hinds, Nicole Sanchez, Reanna Liaw, Rodolfo Garcia, Samantha Gilbert, Steven Stetzler, Tolu Taiwo, Tyneshia Valdez, V Hurtado-Urrutia, Vic Ly, Zeeshawn Kazi, AND MORE!!!

Mom, thank you for raising me. You've done so much with so little, and I owe so much of where I am in life to you. 多謝! To my ancestors and my family, we've come from so much struggle and hardship. I hope that everything I do honors everything you have done. It felt overwhelming when I became the first in our family to get a four-year college degree, the same when I became the first in our family to get a master's degree, and now a PhD. I cannot express the immensity of my gratitude for your hard work for me to get the education I have, particularly after how both Mom and Dad had to drop out of school during the Vietnam War.

To my pets, Pepperoni Tran and Bean Tran- thank you for your sweetness and for sticking with me throughout the good and the bad. You have seen me at my lowest and have loved me nonetheless. Marnie Tran, I miss you. Thank you for being the best dog anyone could ever ask for.

To my partner Tran Ton Nu, I'm so lucky we met. Thank you for your kindness, your humor, and your love. You've seen many of my ups and downs in the past two years of my dissertation time - I'm grateful you've stuck by me through everything. It's a joy and honor to be loved by you.

Thank you, thank you, thank you to everyone who has seen and loved me through my life. I love you all.

DEDICATION

To my dad, *Quang Andy Tran*, grandma, *Liên Sam*, and dog *Marnie Tran* - who all passed away during the course of this thesis. I wish you would have been able to see me become the first person with a doctorate in our family.

Chapter 1

INTRODUCTION

Our universe is made up of dark energy, dark matter, and baryons. Baryons, the tiny percentage of the universe we can directly observe, make up the (personal opinion) most wonderful parts of life- the sun, the trees, our loved ones. Yet despite the thousands of years that people have been able to observe these baryons, there is still so much to learn about them. One of the big questions is: how does baryonic matter evolve over cosmic time?

One of the ways track the changes in baryonic matter is by studying stars, star formation (SF), and its many processes in local star forming regions all the way out to high-redshift galaxies. Most of the active fuel for star formation is in the form of cold gas traced by HI and H2. Molecular gas density as a function of redshift is remarkably similar to the star formation rate density (Lilly et al., 1995; Madau et al., 1996; Genzel et al., 2010; Péroux & Howk, 2020). Understanding their relationship allows us to witness the evolution of baryons over cosmic time.

Cold gas collapses into giant molecular clouds (GMCs) forming a reservoir of neutral molecular and atomic hydrogen gas, the primary ingredient for star formation. Between 75-90% of GMCs form stars, with young ($\lesssim$ 3 Myr) GMCs less likely to form stars (Blitz, 1993; Heyer & Dame, 2015; Miville-Deschênes et al., 2017). Within GMCs, there is a complex, nonlinear, interdependent set of processes determining how, where, and when exactly star formation is induced. Inside such clouds, self-gravity becomes the primary driver of collapse, fragmenting the cloud down to star-forming clumps. These clumps accrete more and more gas until the densities become high enough for hydrogen to fuse, forming stars. As stars undergo fusion, they create metals, or elements heavier than helium, in their stellar interiors, eventually expelling them back into the interstellar medium (ISM) via winds and supernovae.

These metals are necessary for the formation of dust, which plays a big role in catalyzing the formation of molecules for star formation, and enriches the environment around sites of star formation. (Lee et al., 2022)

While the process of SF described above seems simple, at each stage and spatial scale, there are multiple unique driving forces determining the distribution of stars, the masses of the stars (initial and final), what happens to the natal cloud, etc. This process is so complex that despite how much we've learned in the decades of study and observation across the full range of the electromagnetic spectrum, we have yet to develop a robust, unified model of star formation and galaxy evolution that the spatial scales, the variety of galactic environments, and phases of star formation that we observe. This is due in part to the initial formation of stars is often completely obscured by the dust of the surrounding cloud, making these young stages hard to observe the newly formed stars until this dust has been removed or destroyed by feedback. To further add complexity, the local process of stellar birth depends on the supply, distribution, and stability of cloud-scale (on the order of 100 pc) cold gas, which depends on large-scale galaxy dynamics operating at scales 10 to 1,000 times bigger, such as spiral arm features, perturbations from satellite galaxies, or accretion of fresh gas from the cosmic web (Kennicutt, 1998a; Dobbs et al., 2006; Dobbs, 2008; Leroy et al., 2008, 2013; Meidt et al., 2013, 2020). As much as local star formation is influenced by the wider galactic neighborhood, star formation at small scales significantly impacts the global scale. Stellar feedback (in the form of radiation, winds, supernova, etc.) creates a hierarchy of nonlinear feedback loops that impact interstellar medium (ISM) dynamics across a wide range of physical scales (Hopkins et al., 2014; Lopez et al., 2014; Walch et al., 2015; Gnedin, 2016; Rahner et al., 2017; Olivier et al., 2021). These gas and dust motions determine the chemical and thermal state of the ISM, which affects subsequent star formation (Klessen & Glover, 2016). The interplay of all these complex processes make it clear that the many processes that drive, regulate, and extinguish star formation operate together over a vast range of stellar, interstellar, galactic and circumgalactic scales.

Molecular clouds, the densest and most opaque regions of the ISM, span scales of $\sim$1

pc - 100 pc across. The largest molecular clouds, GMCs, can individually create thousands of young stars. Many forces are at play within the GMC itself depending on the density of the cloud and scale we are interested in: magnetic fields, cooling via collisions, protostellar feedback, thermal pressure, turbulence, etc. There are many unanswered questions about this stage at which subregions of GMCs collapse: What causes the formation of these individual star forming regions? How does the gas cool? Is it just the free-fall collapse or are there other processes that factor in? Does star formation in clouds take place over many dynamical times of molecular clouds (i.e. turbulent crossing time or gravitational free-fall time) at high integrated star formation efficiency (integrated fraction of gas that turns into stars)? Or does it take place over a single dynamical time and achieves only a low star formation efficiency?

The Kennicutt-Schmidt law (Schmidt, 1959, 1963; Kennicutt, 1998b, 1989), is an empirical relation between surface density of molecular gas to the star formation rate (SFR) per unit area (Equation 1.1 that well describes SF on scales larger than 500 pc (Kennicutt et al., 2007; Bigiel et al., 2008; Leroy et al., 2013). This relation is well-derived from a balance of macro and statistical properties of these regions, such as self gravity, density, stellar feedback, cooling, and heating, setting the slope and normalization (Ostriker et al., 2010; Ostriker & Shetty, 2011; Hopkins et al., 2014; Hayward & Hopkins, 2017; Semenov et al., 2017; Krumholz et al., 2018; Orr et al., 2018; Semenov et al., 2019).

$$\Sigma_{SFR} \propto \Sigma_{gas}^{N} \quad ; \quad N = 1 - 1.5 \tag{1.1}$$

In their review, Girichidis et al. (2020) summarizes the different macroscopic mechanisms in play depending on the gas surface density: low ($\lesssim 10 M_{\odot}/pc^2$), intermediate ($\sim 10 - 100 M_{\odot}/pc^2$), and high ($\gtrsim 100 M_{\odot}/pc^2$) (Bigiel et al., 2008; Daddi et al., 2010; Genzel et al., 2010; Kennicutt & Evans, 2012). Cooling and heating drives the slope of the Kennicutt-Schmidt law in the low density regime, ignoring metallicity-dependence (Schaye, 2004; Krumholz et al., 2009a,b; Ostriker et al., 2010; Hayward & Hopkins, 2017), where the heating from massive stars is proportional to SFR density, while cooling driven by collisions

is proportional to gas density to the second power. Setting these equal to one another, gives N=2 in the low density regime. At higher gas surface densities, the gas is supersonically turbulent. The turbulent energy dissipation rate and the momentum injection rate by stellar feedback, omitting the Toomre Q (Toomre, 1964) stability parameter, are the primary factors in setting the slope (Ostriker & Shetty, 2011; Faucher-Giguère et al., 2013; Kim & Ostriker, 2015; Orr et al., 2018). In the intermediate regime, the slope is predicted to be N=1, while in the high density regime, N=2, which is in qualitative agreement with Kennicutt & Evans (2012). Because this relation is an ensemble average of the population of molecular clouds and star-forming regions in each galaxy, each with its own highly dynamical processes, models derived from microscopic processes within individual clouds are not suited for comparison to this law (Kruijssen et al., 2019).

However, to understand the micro physical processes induce star formation within GMCs and how they connect to the macro processes, many compare their SF models for individual cloud-scales to the Kennicutt-Schmidt law, even with the stochasticity introduced by time evolution of individual molecular clouds and star forming regions (Schruba et al., 2010; Liu et al., 2011; Feldmann et al., 2011; Kruijssen & Longmore, 2014). Which process is the primary cause of a subregion of the cloud becoming so overdense that its gravitational potential energy exceeds the kinetic energy of the gas? Kravtsov (2003); Li et al. (2005) use the probability distribution of gas density to suggest that the fraction of high density gas varies with overall density. Tan (2000) models star formation induced by cloud-cloud collisions. Another theory put forth is that the magnetic fields within star forming regions support the clouds from collapsing rapidly, however Crutcher (1999); Bourke et al. (2001); Padoan et al. (2004) show through observations in the Milky Way and statistical indicators that they are likely not strong enough. Finally, Krumholz & McKee (2005) proposes that regions where local gravitational potential energy overcomes supersonic turbulence, observed in GMCs (Fukui et al., 2001; Engargiola et al., 2003; Mac Low & Klessen, 2004; Elmegreen & Scalo, 2004; Rosolowsky & Blitz, 2005), forming stars. Despite these complicated and non-linear processes involved in individual star formation, the global process of star formation in

galaxies still follow simple relations. (AMAZING!)

Regardless of which process primarily induces star formation, once the cloud collapses due to self-gravity, thermal pressure, and magnetic fields become less significant factors (Girichidis et al., 2020). The cloud contracts and new stars are born (Krumholz & McKee, 2005; Dobbs et al., 2014; Chevance et al., 2020a). Girichidis et al. (2020) hypothesizes that many individual regions could collapse simultaneously, explaining why stars tend to form in clusters and associations (Lada & Lada, 2003; Bressert et al., 2010; Kruijssen, 2012). Compact star clusters usually form inside more extended associations of young stars (Feitzinger & Galinski, 1987; Maíz-Apellániz, 2001; Lada & Lada, 2003; Elmegreen et al., 2006; Elmegreen, 2008; Portegies Zwart et al., 2010; Krumholz et al., 2018) as a part of hierarchical structure for star formation that resembles the distribution of dense interstellar clouds (Scalo, 1985; Fleck, 1996; Elmegreen & Falgarone, 1996; Cartwright & Whitworth, 2004).

Where and how quickly stars form are determined by flow patterns in the ISM and are influenced by the energy and momentum input from massive stars (Mac Low & Klessen, 2004; McKee & Ostriker, 2007; Hennebelle & Falgarone, 2012; Federrath, 2013). Two models have been proposed for what determines masses of the resulting stars, competitive accretion (Bonnell et al., 2001) and fragmentation induced starvation (Peters et al., 2010a; Girichidis et al., 2012; Kruijssen et al., 2012). In the competitive accretion model, gas is funneled into the center of the gravitational potential and thus centrally located stars acrete the most mass, while with turbulent fragmentation, new stars accrete the in-flowing gas, depriving central stars of material. The details of accretion flow, turbulence, available gas, onset of stellar activity and protostellar feedback determines which model is favored (Peters et al., 2010b; Girichidis et al., 2011; Geen et al., 2015).

Because young stars inherit the spatial properties, kinematics, and dynamics of their natal gas, we can learn more about their formation histories (knowledge which is obscured by dust) by studying distribution of young stars over time. Thus, by quantifying the spatial correlation as a function of cluster mass, we can constrain cluster formation models. For example, Elmegreen et al. (2020) found that more massive and irregularly-shaped (non-

centrally concentrated) LEGUS clusters were systematically bunched together compared to lower mass clusters in low-mass galaxies. However, this was not present in high-mass galaxies nor centrally-concentrated clusters. This could point to differences in cluster formation and scattering in shallow gravitational potentials of low-mass galaxies. Mutual cluster attraction leading to the coalescence in dense regions might also be indicated (Lahén et al., 2019). This phase in which young stars form and remain embedded lasts approximately 2-7 Myr - roughly 20 percent of total cloud lifetime (Kim et al. (2023); Whitmore et al. (2023), and references therein).

When these stars form, feedback in the form of protostellar outflows, radiation, stellar winds, and supernoavae inhibit star formation, keeping the integrated star-formation efficiency low, at a few percent. This eventually leads to the dissolution of birth clouds after about a dynamical time (10-30 Myr) (Walch et al., 2012; Dale et al., 2013; Kruijssen et al., 2019; Chevance et al., 2020b). Not only is supply of gas being depleted by the stars, it can also pushed out of the galactic disc to form a fountain flow or escape from the galaxy as a wind (Hill et al., 2012; Walch et al., 2015; Girichidis et al., 2016). Mass outflow rates, which are comparable to SFR, strong dynamical impact on the evolution of galaxies and the redistribution of gas in the ISM (Naab & Ostriker, 2017; Somerville & Davé, 2015; Veilleux et al., 2005). Hot turbulent gas, enriched with metals, then forms the reservoir from which the next molecular clouds form. It is important to note that the cycle of gas in the ISM is a continuous process in which different regions of the ISM pass through hot, warm, and cold phases at different rates.

Stellar feedback is not only disruptive. Pressure waves, ejected material, and turbulence created by feedback can also locally trigger the onset of gravitation collapse and there by cause star formation by increasing the gas density and accelerating cooling. This impact of stellar feedback is hard to measure. In the recent decade, high resolution imaging of molecular gas in nearby galaxies (Sun et al., 2018) and new methods (Kruijssen et al., 2018) trace the spatial offset between tracers of molecular gas and massive star formation to quantify the underlying cloud life cycle (Schruba et al., 2010; Kreckel et al., 2018; Schinnerer et al.,

2019). In the local galaxy population, molecular clouds have dynamical time of 10-30 Myr with low star formation efficiencies (1-10%) (Kruijssen et al., 2019; Chevance et al., 2020b). Understanding star formation requires us to understand a multi-scale system: the individual stars, clusters, clouds, galaxies, and their relationships.

So with all this background, what exactly am I doing with this dissertation? My main interest is in how stars form as a function of their different environments. How are are the properties of individual stars determined by the properties of the medium from which it forms? What processes determine the physical conditions within star-forming regions? How is the SFR determined by properties of the natal GMC or ISM of the galaxy? What determines the mass and spatial distribution of forming stars?

To answer all these questions, we look to young massive stars and clusters, which can be observed at greater distances and thus a wider variety of galaxies and their individual environments. Massive stars are defined as stars 8 solar masses and above, and for the purposes of this thesis, we define "young" to be less than 25 Myr. Because they are short-lived, massive stars directly show where recent star formation is happening (Kennicutt, 1998a; Donas et al., 1987). These younger populations are more likely to inform us on their history of formation. Obtaining high spatial resolution data of these young massive stellar populations is necessary to overcome the challenge of large dynamic range in studying their indivdual and cluster formation.

Unfortunately, there are two particularly difficult obstacles for these studies. First, massive stars are difficult to observe, particularly while they're forming because: they are short-lived; they emit a large portion of their spectrum in the UV which cannot be easily observed from the ground; they can be often obscured by dust; and there are few of them. Second, because of this observational challenge, complex selection effects make it difficult to generally apply results, such as cluster mass functions, derived for very specific cases.

Because of these observational constraints, there is not enough data for good statistics on young massive star populations. Data from relatively close, face-on spiral galaxies with high star formation rate is ideal for getting a large, well spatially-distributed sample of young

massive stars to probe the wide range of galactic environments. Unfortunately, extragalactic resolved star photometry is difficult because we must observe these young, massive stars in the UV with incredibly high spatial resolution.

Excitingly, NGC 6946 has the potential to help us overcome these difficulties. It is a nearby, well-studied starburst face-on spiral galaxy (Figure 1.1). Because of the active star formation and the 10 supernovae that have been observed in the past century (Prieto et al., 2008), earning it the nickname The Fireworks Galaxy, it has been extensively observed in multiple bandpasses (Eibensteiner et al., 2022; Koplitz et al., 2021) to study its molecular gas, dust, and supernova remnants. Strangely, despite being an ideal galaxy to study star and cluster formation and galactic structure with approximately 200 HST visits of multi-wavelength data, no one has ever characterized the stellar populations across NGC 6946. These stellar populations, particularly the young massive stars and their clusters, are the missing piece to the full picture of star formation in this galaxy with well-mapped molecular gas, supernova remnants, and black holes.

In the next few chapters, we attempt to answer the questions posed above with this wonderful dataset. In Chapter 2, we measure the spatially-resolved star formation history of NGC 6946, test the diagnostics for star formation rate, and analyze the local star formation history of specific regions of interest. In Chapter 3, I modify a computer-vision algorithm to automate non-parametric cluster candidate finding. We measure the luminosities, effective radii, and colors of the cluster and association candidates found. In Chapter 4, I constrain the cluster mass-radius relation and mass function of clusters, measure the age of the clusters, and determine the cluster formation efficiency of NGC 6946. In Chapter 5, I outline my future work of aligning over 200 HST visits to obtain the spectral energy distributions of over 8 million stars in NGC 6946 and measure their spectral parameters.

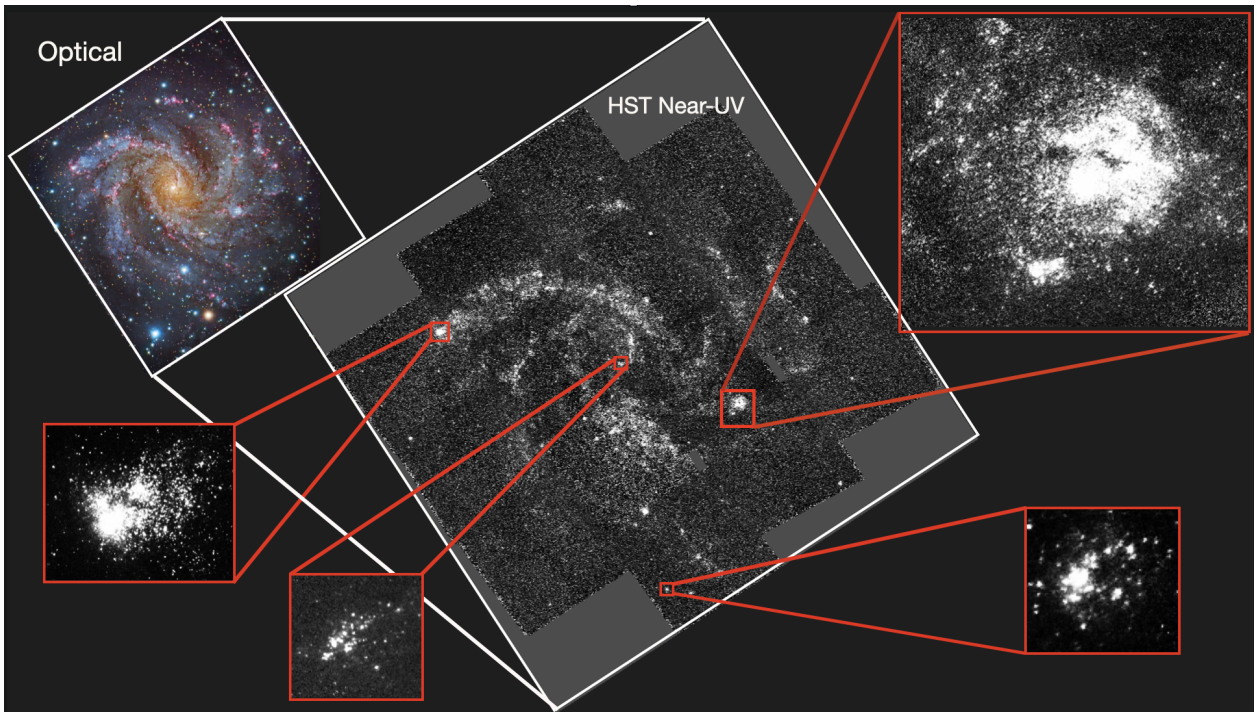

Figure 1.1 Example mosaic image of NGC 6946 in HST's WFC3/UVIS filter F336W with a few clusters (out of approximately 1600 clusters in the UV) identified and shown in postage stamps. A cropped optical composite image is included in the top left for context, with data taken from Subaru Telescope, National Astronomical Observatory of Japan, and the Hubble Legacy Archive.

Chapter 2

SPATIALLY-RESOLVED RECENT STAR FORMATION HISTORY IN NGC 6946

In this chapter, I focus on using near-UV (NUV) photometry of over 80,000 young massive stars in NGC 6946 obtained with Hubble Space Telescope (HST) Wide Field Camera 3 (WFC3) F275W and F336W filters to characterize the structure, the distribution of the young massive stellar population, and their formation histories in their diverse range of environments across the galaxy. The bulk of this work was published in a refereed paper as Tran et al. (2023).

2.1 Introduction

Star formation rate (SFR) is one of the defining characteristics in determining the current evolutionary state of a galaxy. The SFR strongly affects evolution through metal production (Larson, 1974), gas consumption (Kennicutt, 1983; Chiappini et al., 1997), cold gas content (Kauffmann & Haehnelt, 2000), and feedback in the galaxy (de Rossi et al., 2009). Thus, SFR is a key property in tests of galaxy evolution models (Tinsley, 1980; Kennicutt, 1998a; Kauffmann & Haehnelt, 2000). Because of its significance, many methods of measuring star formation rate with observational data have been developed, such as measuring UV emission from young ($\lesssim$ 10 Myr) massive stars (Kennicutt, 1998a; Kennicutt & Evans, 2012), Hα emission from the youngest ($\lesssim$ 5 Myr) massive stars (Kennicutt, 1983; Shivaei et al., 2015), and estimating SFR from the rate of core-collapse supernova (ccSN) (Eldridge & Xiao, 2019), which probes SFR at timescales at which stars supernova (30-100 Myr ago). These methods probe a range of timescales, making direct comparisons between SFR measured with different indicators challenging. Star formation histories (SFHs) avoid this problem by providing the

SFR over time, allowing us to compare and calibrate SFR measurements obtained with different methods, while revealing how galaxies change over time.

Even more powerful are spatially-resolved star formation histories, which provide both temporal and spatial information. With these, we can trace local mechanisms that could be triggering star formation. For nearby galaxies with resolved stellar photometry, we can construct and fit observed color-magnitude diagrams (CMDs) to infer a star formation history for a specific region, assuming a specific initial mass function (IMF), stellar evolutionary model, binary fraction, and distribution of dust. By tiling together SFHs from multiple regions, we can construct a spatially-resolved star formation history for a galaxy. This kind of work has been done in the Small and Large Magellenic Clouds (Harris & Zaritsky, 2004, 2009), M31 (Williams, 2003; Lewis et al., 2015), M33 (Lazzarini et al., 2022), and M81 (Choi et al., 2015).

In this paper, we apply this technique to NGC 6946, which has been widely studied due to its active star formation (Schinnerer et al. (2007) classify it as a circumnuclear starburst) and the high frequency of supernovae in the past century (Sauty et al., 1998; Meier & Turner, 2004; Schinnerer et al., 2007; Murphy et al., 2011; Kennicutt et al., 2011; Botticella et al., 2012; Tsai et al., 2013; Gorski et al., 2018; Eldridge & Xiao, 2019; Eibensteiner et al., 2022). Among these studies, there have been inconsistent measurements of the galaxy's global star formation rate, ranging widely from 3-12 $M_{\odot}$/yr, due to the diverse methods of measuring star formation rate and wide range of different distances used. Throughout this paper, we use a distance of 7.83 ± 0.29 Mpc (Murphy et al., 2018) and an inclination of 32.8° (de Blok et al., 2008). Murphy et al. (2011) has explored the accuracy of these various diagnostics for a sample of regions in NGC 6946, finding discrepancies of up to factors of 5. To better constrain the recent star formation history across the entire galaxy, we have carried out a NUV HST survey to obtain photometry of the young massive stellar population of NGC 6946. This dataset provides the most detailed and complete probe to date of the global, localized, and episodic star formation in NGC 6946.

In Section 2.2, we present the HST observations, alignment of the data, photometry,

artificial star tests for measuring photometric uncertainties, gridding schema, and method for measuring star formation rates. In Section 2.3, we present the recent star formation rates, the reliability of the SFRs at the youngest and oldest time bins, total stellar mass formed over the past 25 Myr, and foreground and differential extinction of each cell. In Section 2.4, we discuss two highly star-forming regions of interest, the decline in global star formation rate, and the correlation between stellar density and age. In Section 2.5, we summarize our methods and findings.

2.2 Observations and Data Analysis

Observations for this program (GO-15877; PI Levesque et al. (2019)) were obtained between May 11 2020 and November 21 2021 using HST's WFC3 Ultraviolet- (UVIS) channel in filters F275W and F336W. Details of the observations are found in Table 2.1. NGC 6946 was imaged in a 4x4 grid excluding the northernmost and southernmost regions (Figure 2.1). This covers all of the UV-bright regions and the locations of observed core collapse supernovae. Each neighboring pointing overlaps at the edges to ensure there are no gaps in the catalog due to poorer photometric quality at the edges. Each pointing in both filters was dithered with small offsets to control for hot pixels and cosmic rays. Unfortunately, even with the careful selection of observing strategy, there are two small gaps of $10'' \times 1'$ and $30'' \times 1'$ approximately centered at 20:34:39.40 +60:06:80 and 20:34:25.00 +60:08:80, respectively. These gaps are due to adjusting the rotation of two pointings to obtain a sufficient number of guide stars. Upon comparison with existing optical data, there do not appear to be dense star clusters in these two gaps.

Table 2.1. Details of Fields Observed

Field Name	R.A. (hh:mm:ss.sss)	Dec (°°:′′:′′′.′′′)	Filters	Exposure Time (s)	Number of Exposures	Date (YYYYMMDD)	Roll Angle (PA_V3)
NGC6946-2	20:35:06.007	+60:12:48.93	F275W	1432	2	20201106	257.0
NGC6946-2	20:35:06.007	+60:12:48.93	F275W	1414	2	20201106	257.0
NGC6946-3	20:34:38.218	+60:12:59.17	F275W	1432	2	20201109	256.5
NGC6946-3	20:34:38.218	+60:12:59.17	F275W	1414	2	20201109	256.5
NGC6946-4	20:35:19.114	+60:10:49.51	F275W	1432	2	20201110	255.7
NGC6946-4	20:35:19.114	+60:10:49.51	F275W	1414	2	20201110	255.7
NGC6946-5	20:34:51.355	+60:10:59.92	F275W	1432	2	20201103	257.0
NGC6946-5	20:34:51.355	+60:10:59.92	F275W	1414	2	20201103	257.0
NGC6946-6	20:34:23.591	+60:11:09.97	F275W	1432	2	20201103	257.0
NGC6946-6	20:34:23.591	+60:11:09.97	F275W	1414	2	20201103	257.0
NGC6946-7	20:35:32.194	+60:08:50.01	F275W	1432	2	20201112	257.0
NGC6946-7	20:35:32.194	+60:08:50.01	F275W	1414	2	20201111	257.0
NGC6946-8	20:35:04.464	+60:09:00.59	F275W	1432	2	20201112	253.5
NGC6946-8	20:35:04.464	+60:09:00.59	F275W	1414	2	20201112	253.5
NGC6946-9	20:34:36.730	+60:09:10.81	F275W	1371	2	20210504	75.5
NGC6946-9	20:34:36.730	+60:09:10.81	F275W	1390	2	20210504	75.5
NGC6946-10	20:34:09.061	+60:09:21.20	F275W	1432	2	20200515	73.0
NGC6946-10	20:34:09.061	+60:09:21.20	F275W	1414	2	20200515	73.0
NGC6946-11	20:35:17.548	+60:07:01.19	F275W	1432	2	20201112	253.0
NGC6946-11	20:35:17.548	+60:07:01.19	F275W	1414	2	20201112	253.0
NGC6946-12	20:34:49.842	+60:07:11.57	F275W	1432	2	20201113	253.0
NGC6946-12	20:34:49.842	+60:07:11.57	F275W	1414	2	20201113	253.0
NGC6946-13	20:34:22.203	+60:07:22.13	F275W	1432	2	20200511	73.0
NGC6946-13	20:34:22.203	+60:07:22.13	F275W	1414	2	20200511	73.0
NGC6946-14	20:35:02.928	+60:05:12.26	F275W	1432	2	20201107	257.0
NGC6946-14	20:35:02.928	+60:05:12.26	F275W	1414	2	20201107	257.0
NGC6946-15	20:34:35.318	+60:05:22.98	F275W	1362	2	20211114	257.0
NGC6946-15	20:34:35.318	+60:05:22.98	F275W	1361	2	20211115	257.0
NGC6946-2	20:35:06.007	+60:12:48.93	F336W	880	3	20201106	257.0
NGC6946-3	20:34:38.218	+60:12:59.17	F336W	880	3	20201109	256.5
NGC6946-4	20:35:19.114	+60:10:49.51	F336W	880	3	20201110	255.7
NGC6946-5	20:34:51.355	+60:10:59.92	F336W	880	3	20201103	257.0
NGC6946-6	20:34:23.591	+60:11:09.97	F336W	880	3	20201103	257.0

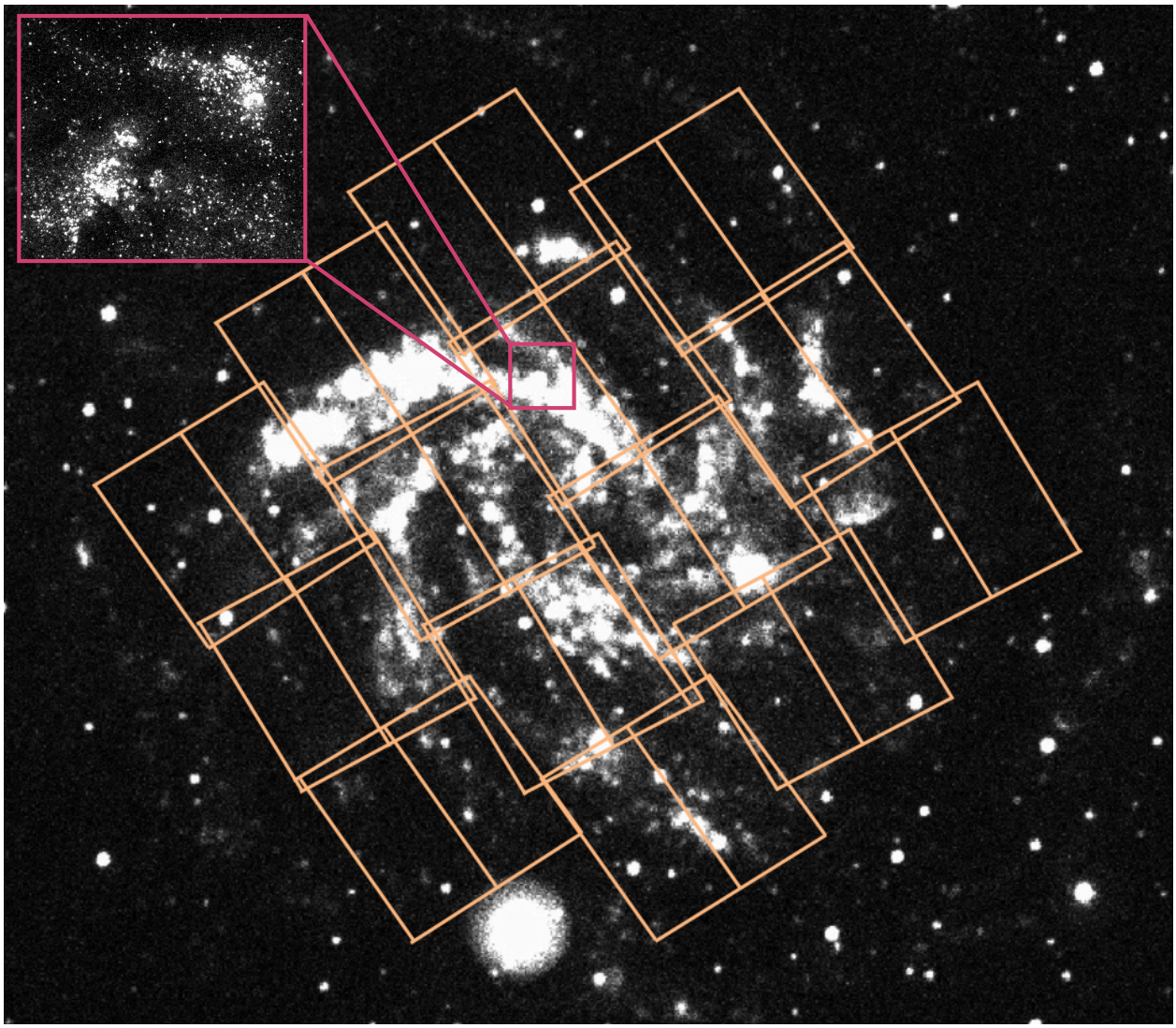

Figure 2.1 Yellow boxes showing HST footprint of the 14 pointings of our data overlaid on a GALEX NUV image from the GALEX Nearby Galaxies Survey (NGS; Gil de Paz et al. (2007) and references therein). In the magenta thumbnail is an example of what the resolution of the HST data in F336W to illustrate the high spatial resolution that allowed us to get spatially-resolved stellar photometry.

Table 2.1 (cont'd)

Field Name	R.A. (hh:mm:ss.sss)	Dec (°°:′′:′′′′.′′′′)	Filters	Exposure Time (s)	Number of Exposures	Date (YYYYMMDD)	Roll Angle (PA_V3)
NGC6946-7	20:35:32.194	+60:08:50.01	F336W	880	3	20201111	257.0
NGC6946-8	20:35:04.464	+60:09:00.59	F336W	880	3	20201112	253.5
NGC6946-9	20:34:36.730	+60:09:10.81	F336W	865	3	20210504	75.5
NGC6946-10	20:34:09.061	+60:09:21.20	F336W	880	3	20200515	73.0
NGC6946-11	20:35:17.548	+60:07:01.19	F336W	880	3	20201112	253.0
NGC6946-12	20:34:49.842	+60:07:11.57	F336W	880	3	20201113	253.0
NGC6946-13	20:34:22.203	+60:07:22.13	F336W	880	3	20200511	73.0
NGC6946-14	20:35:02.928	+60:05:12.26	F336W	880	3	20201106	257.0
NGC6946-15	20:34:35.318	+60:05:22.98	F336W	870	3	20211114	257.0

Note. — Config Mode - WFC3/UVIS Imaging

2.2.1 Source Detection and Photometry

HST WFC3 NUV photometry were measured using DOLPHOT (Dolphin, 2000, 2016), a stellar photometry package using point spread function (PSF) fitting, described in detail in Williams et al. (2014). We generated separate catalogs for each of the 14 overlapping pointings using the same DOLPHOT parameters as in Williams et al. (2014). We then combined all of the measurements into a single catalog, described in Section 2.2.2. In this catalog, we identified sources as reliable, high quality photometry using the metrics of sharpness$^2 < 0.2$; crowding < 0.7; signal-to-noise ratio (SNR) > 4 in both F275W and F336W; and F275W-F336W color $<$ -1.3, as anything blueward of this color is unphysical for young massive stars, see Figure 2.3 for comparison with Padova isochrones. For the analysis in the paper, we used $\sim$ 81,000 sources that passed the aforementioned quality cuts. The brightest single stars in the Padova log(age)=6.6 isochrone (Marigo et al., 2008), the youngest age we could fit, had a F336W magnitude of 20, so sources with magnitudes brighter would be likely blends. These likely blends, which are noted in the catalog, were included in our analysis as we were interested in the high crowding regions. The impact of including the blends is further discussed in Section 2.3.4.

2.2.2 Astrometry and Foreground Stars

Using the high quality photometry, we cross-match our stellar catalog to *Gaia* Data Release 2 (*Gaia* DR2; Gaia Collaboration et al. (2016); Gaia Collaboration et al. (2018)). We shifted each frame by the median of the residuals of the sources matched between our catalog and *Gaia* DR2. The residuals have mean magnitudes on milliarcsecond scales in both right ascension and declination, which is roughly a hundred times smaller than a WFC3 UVIS pixel. The values of the overlapping sources were then averaged.

After finding *Gaia* matches, we removed likely foreground stars from our analysis. First, we utilized the matched *Gaia* sources to remove anything with a measured proper motion, as it is a likely foreground star. Then, we applied the following F275W-F336W color cuts to remove brighter, redder sources that are likely foreground stars: F336W $<$ 21, color $>$ 0.7; F336W $<$ 22, color $>$ 1; F336W $<$ 22.5, color $>$ 2; F336W $<$ 23, color $>$ 2.5. The photometric catalog used in this paper can be found as a High Level Science Product in MAST (the Mikulski Archive for Space Telescopes) via doi: 10.17909/gveq-8820.

2.2.3 Spatial Mapping

To recover the spatially-resolved SFH, we first divide our full photometric catalog into a custom grid pattern (Figure 2.2), allowing us to recover the SFH in each grid cell independently. We choose a grid pattern such that the size of the cell is based on the stellar density of the cell, which helps equalize the number of stars per cell. This gridding schema ensures the denser regions are divided into finer spatial bins, or cells, taking advantage of the large number of stars available for age constraints. Conversely, the less dense regions are divided into coarser cells to ensure each cell has enough stars to measure reliable ages (see Section 2.3.5 for details).

To generate the cell vertices, we implemented a quadtree algorithm, which operates as follows. First, it counts the number of stars in the specified region. If the number of stars in the region is higher than a certain threshold (100 stars in this study), then it will subdivide

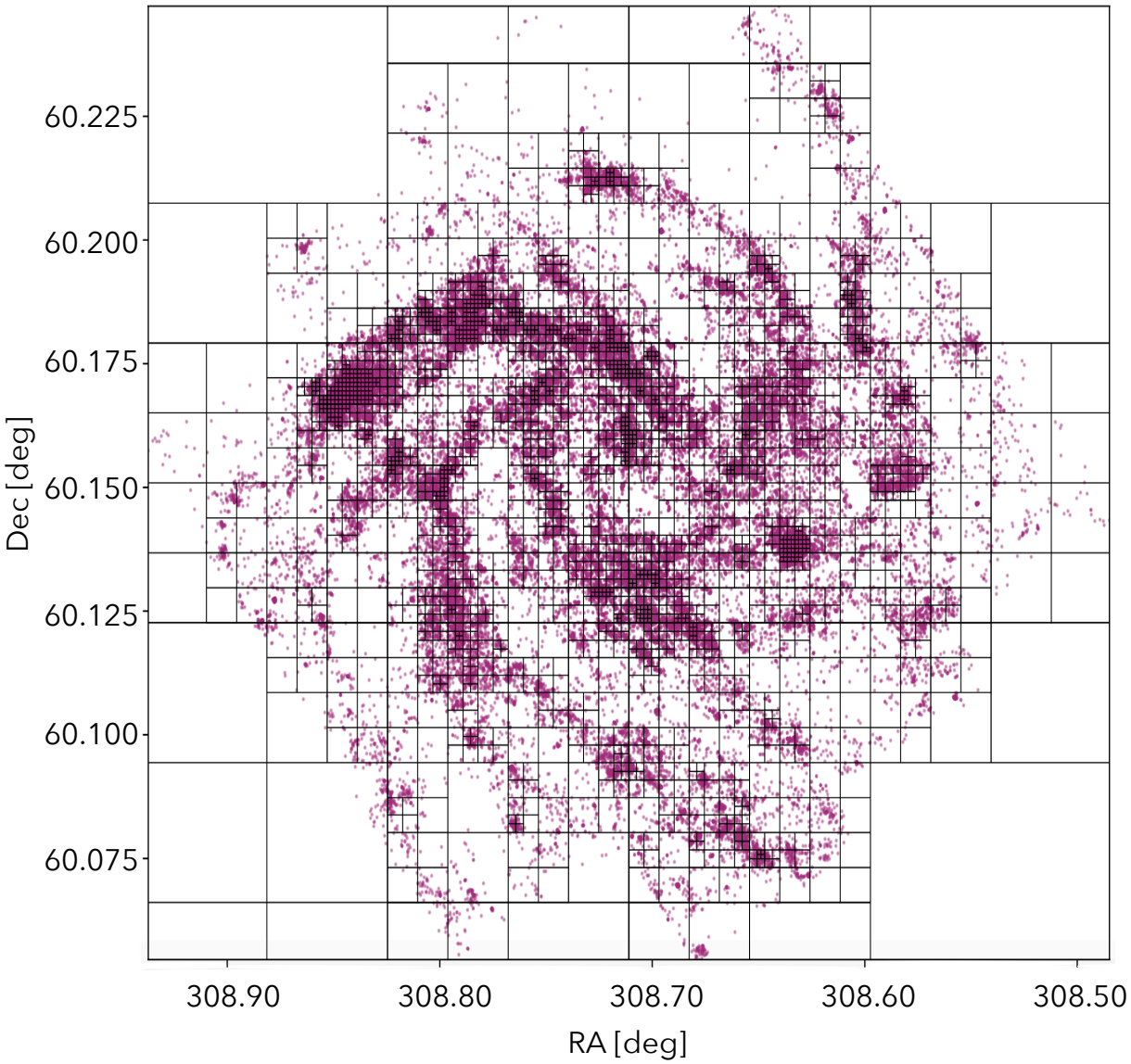

Figure 2.2 Grid pattern determined via quadtree with the positions of the good quality stars in pink. The quadtree algorithm works by iteratively subdividing regions that exceed a set number of stars into four equal squares until it hits a minimum cell size of 3"x3" (100 pc x 100 pc), which is roughly the size of clusters. For more details on our implementation of the quadtree algorithm, see Section 2.2.3

into four equal parts. This iterates until it hits a minimum cell size, which is roughly $3'' \times 3''$ ($\sim$ 100pc $\times$ 100pc), chosen because that is the approximate size of clusters in NGC 6946.

2.2.4 Artificial Star Tests and Completeness

We use artificial star tests (ASTs) to measure the effects of noise, crowding, and bias on the photometry. We injected artificial stars into regions of the galaxy of different stellar densities to assess how well artificial stars of different colors and magnitudes are recovered as a function of stellar density. The input and recovered colors and magnitudes are included as a parameter in the derivation of the SFHs (Section 2.2.5) to account for these biases.

Because the impacts of crowding are largely density-dependent, we must ensure that our ASTs are fully sampling the wide range in the environment. For each cell, we calculate a stellar density by taking the number of stars that pass the quality cut described in Section 2.2.1 above 25 mag in the F336W filter in the cell and dividing it by size of cell in arcsec^2. We attempted several ways of binning the cells by density, but ultimately separated them into a low density regime (cells with densities less than 11.5 stars/arcsec^2) and a high density regime (cells with densities greater than 11.5 stars/arcsec^2). We illustrate the differences in the depth of the observed data in the low and high density regimes in Figure 2.3.

We further bin these cells by density to generate at least 20,000 artificial stars per density bin to ensure that we have a sufficiently fine grid of artificial stars of different colors and magnitudes. These artificial stars were then run through DOLPHOT and flagged as recovered or unrecovered. Artificial stars are defined as recovered if they pass the same quality cuts we apply to our dataset, described in Section 2.2.1. For each density bin, we divided recovered and unrecovered stars into bins of width of 0.2 magnitude. We then convolved the ratio of recovered to unrecovered stars with a boxcar function to smooth this ratio and interpolated the magnitudes at which 50%, of the stars are recovered, or simply the 50% completeness limits. The F275W and F336W 50% completeness limits define the magnitude ranges that we fit with models to obtain star formation history measurements, as described in detail in Section 2.2.5.

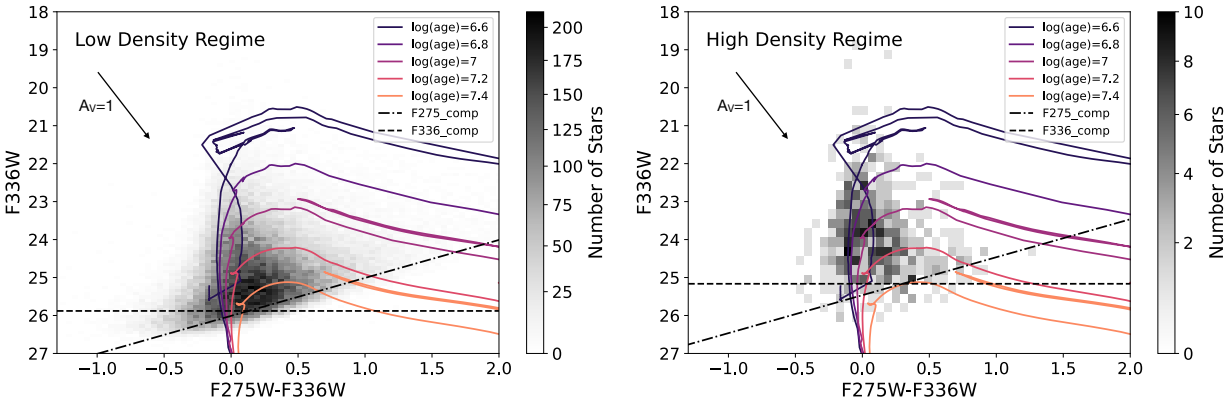

Figure 2.3 Left: The binned observed color-magnitude diagram of all the stars in density bins between 0-11.5 stars/arcsec^2. Right: The binned observed CMD of all stars in density bins between 12-17 stars/arcsec^2. On both CMDs, isochrones with log(age)=6.6 to log(age)=7.4, the F275W and F336W 50% completeness, and an A_V=1 vector are overplotted.

We took the mean of the 50% completeness limits in the low density regime to smooth over some of the stochasticity ($\pm$ 0.1 mag variation in both filters) and determined a mean 50% completeness of 26.02 and 25.88 in the F275W and F336W filters, respectively (Figure 2.4). With so few of the cells in the high density regime, it was computationally feasible to run these artificial star tests for those individual high density cells to determine the cell's individual completeness limit.

2.2.5 Derivation of the SFHs

We used the CMD-fitting code, MATCH (Dolphin, 2002), to derive the star formation history of each cell. For each cell, MATCH creates Hess-diagrams or binned CMDs of stars in the cell. MATCH then takes user-defined ranges in age, metallicity, distance, extinction, IMF, and binary fraction to create individual synthetic CMDs for each possible combination of parameters. The individual CMDs generated from given parameters are linearly combined to form composite CMDs, which are compared to the observed CMDs. The best-fit composite synthetic CMDs are then used to infer what ages and metallicities make up the observed cell

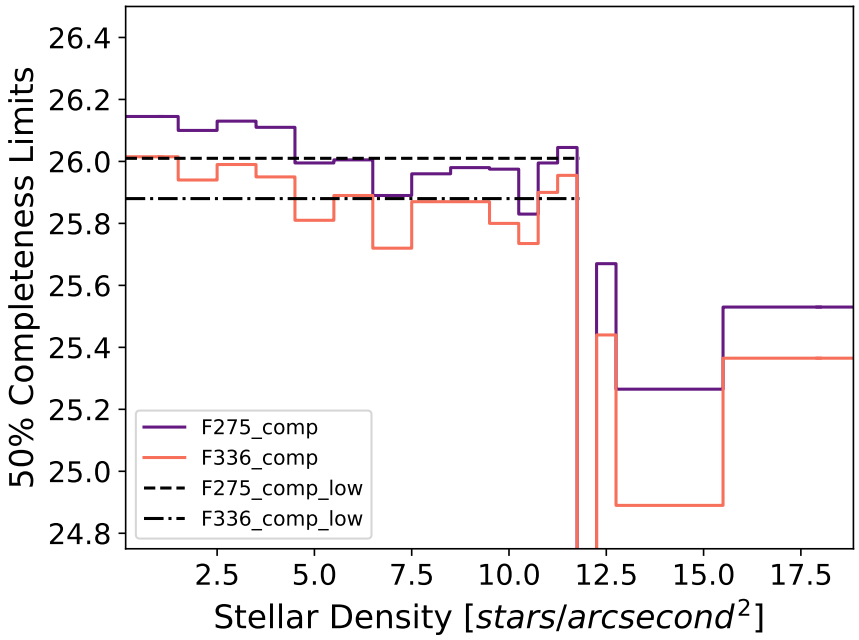

Figure 2.4 50% completeness limits in both F336W and F275W plotted as a function of stellar density. The mean completeness limit of the low density regime is overplotted in the dashed lines. There are no stars with densities between 11.5-12 and are thus not plotted.

and its resulting star formation history.

We choose a Kroupa IMF (Kroupa, 2001), binary fraction of 0.35, and the Padova stellar evolutionary models (Marigo et al., 2008; Girardi et al., 2010). We use the distance of 7.83 ± 0.29 Mpc to be consistent with Murphy et al. (2018), who used the same CMD-fitting technique. Because of the short timescale, we fix the metalliciities to be between log(Z)= -0.5 to 0.1 and fix the most recent time bins to have near solar metallicities. The youngest age we could fit was log(age)=6.6. As seen in Figure 2.3, the NUV data barely graze the log(age)=7.5 isochrone for the low density bin and the log(age)=7.4 isochrone for the high density bin. However, for completeness, we fit up to ages of log(age)=7.5. For a more detailed discussion on the reliability of the age range fit, see Sections 2.3.4 and 2.3.5. A summary of these parameters is provided in Table 2.2.

First, we determine the best fit values of foreground extinction (A_V) and differential, or

Table 2.2. MATCH Fitting Parameters

Parameter	Values
IMF Model	Kroupa
Evolutionary Models	Padua2006
Distance	7.83 ± 0.29 Mpc
Distance Modulus	29.47 ± 0.079
A_V	0.8-2.2, steps of 0.1
log(Z)	-0.5 - 0.1, steps of 0.1
Binary fraction	0.35
F336W step size	0.1
F275W-F336W step size	0.05
CMD smoothing param	3
F275-F336W	-1.3-3.3
Ages (log(yr))	6.6-7.4 for $\rho < 11.5$
	6.6-7.5 for $\rho \geq 11.5$
Age step size	0.1

Note. — ρ = stellar density in stars/arcsec^2

circumstellar, extinction (dA_V) of each cell by running SFH calculations over a coarse grid of A_V and dA_V with A_V between 0.8 to 2.2 with the parameters in Table 2.2. Finding the highest likelihood value of A_V and dA_V, we then redo the same SFH calculations over a finer grid of values in 0.05 increments to find the best fit A_V and dA_V, described in detail in Lewis et al. (2015). Second, we adopt the best fit A_V and dA_V and rerun the SFH calculations to determine the best fit star formation rate and metallicity per time bin in each cell. Third, we measure the uncertainties of the star formation rates and metallicities by running a hybrid Monte Carlo algorithm, described in detail in Section 2.2.6. We then combine the SFH of each cell to create a spatially-resolved map of NGC 6946's star formation history, presented in Section 2.3.1.

2.2.6 Uncertainties

There are a few systematic uncertainties associated with this analysis. First, the choice of binary fraction could have a systematic impact our results. For consistency with other work deriving the recent SFH of galaxies (Lewis et al., 2015; Lazzarini et al., 2022), we adopt a binary fraction of 0.35, knowing that massive stars have a binary fraction greater than 0.7 (Sana et al., 2012). Lewis et al. (2015) showed that uncertainties introduced by choice of binary fraction are small compared to the uncertainties due to dust. Second, choice of stellar evolutionary model has a systematic impact on our results. Lazzarini et al. (2022) showed that the SFH measured using the Padova versus MIST models differed at ages less than 20 Myr. However, results from individual cells fit with both models agreed within less than 1%. Third, choice of IMF could impact our results. For consistency, we used the Kroupa IMF, which has been widely used for measuring star formation rate in NGC 6946.

To characterize the random uncertainties, we used a hybrid Monte Carlo (MC; Duane et al. (1987)) implemented within MATCH. These uncertainties scale with the number of stars in each cell, where more stars in a cell result in lower random uncertainties. From each cell's CMD, we generate 10,000 possible SFHs. We then calculate the 1-sigma error by calculating the 68th-percentile of the samples for the cell.

2.3 Results

In Table 2.3, we present the best fit star formation rates per time bin, number of stars in the cell (N), area in arcsec^2, mean age of the population, A_V, and dA_V, along with their cell indices and vertices. The mean age of the population in each cell is only included for a convenient reference. Some cells can be have a bimodal or trimodal age distribution, so please use this mean age with caution. Some numbers in this table have been rounded to save space, but the full machine readable table for all 2658 cells contain the measurements with full precision.

2.3.1 Star Formation Rate and Mass Maps

In Figure 2.5, we present maps of the spatially-resolved star formation rate for NGC 6946 in linear time bins, and include a color image from the unWISE catalog (Meisner et al., 2022)) in W1 and W2 filters to illustrate that the star formation in the youngest ages is mostly recovered despite the dust and we are not missing much embedded star formation. For every time bin, labeled in the upper left corner of each panel, we create maps with the best fit star formation rate setting the value of intensity of each pixel. These rates are then converted to star formation rate intensity by dividing by the area of the cell in corrected for the inclination of 32.8 degrees (de Blok et al., 2008). In Figure 2.6, we present the spatially-resolved star formation history for NGC 6946 with log time bins for higher time resolution at younger ages.

Table 2.3. Sample of SFRs over Time

i	RA-E $^\circ$	Dec-N $^\circ$	RA-W $^\circ$	Dec-S $^\circ$	N	Area $''^2$	SFR 0-6.7 1e-3$M_\odot/yr$	SFR 6.7-6.8 1e-3$M_\odot/yr$	SFR 6.8-6.9 1e-3$M_\odot/yr$	SFR 6.9-7.0 1e-3$M_\odot/yr$
8	308.51220	60.150921	308.48380	60.136787	17	2588.9	$0.00^{+0.14}_{-0.00}$	$0.00^{+0.57}_{-0.00}$	$0.00^{+0.64}_{-0.00}$	$0.06^{+0.62}_{-0.06}$
9	308.51220	60.165054	308.48380	60.150921	6	2588.9	$0.00^{+0.10}_{-0.00}$	$0.00^{+0.41}_{-0.00}$	$0.00^{+0.36}_{-0.00}$	$0.00^{+0.38}_{-0.00}$
12	308.59740	60.263989	308.48380	60.207455	18	41422.6	$0.00^{+0.22}_{-0.00}$	$0.00^{+1.11}_{-0.00}$	$0.00^{+1.22}_{-0.00}$	$2.01^{+0.00}_{-1.98}$
14	308.54060	60.136787	308.51220	60.122654	7	2588.9	$0.23^{+0.10}_{-0.20}$	$0.00^{+0.78}_{-0.00}$	$0.00^{+0.64}_{-0.00}$	$0.00^{+0.78}_{-0.00}$
15	308.54060	60.150921	308.51220	60.136787	60	2588.9	$4.29^{+0.81}_{-1.76}$	$0.00^{+7.40}_{-0.00}$	$0.00^{+5.96}_{-0.00}$	$10.0^{+0.07}_{-9.62}$
16	308.54060	60.165054	308.51220	60.150921	54	2588.9	$1.95^{+0.27}_{-1.05}$	$0.00^{+3.11}_{-0.00}$	$0.00^{+3.32}_{-0.00}$	$2.42^{+1.80}_{-2.42}$
17	308.54060	60.179188	308.51220	60.165054	40	2588.9	$1.15^{+0.69}_{-0.67}$	$0.00^{+4.72}_{-0.00}$	$7.30^{+2.64}_{-4.74}$	$0.00^{+5.01}_{-0.00}$
18	308.56900	60.108520	308.54060	60.094387	41	2588.9	$0.00^{+0.91}_{-0.00}$	$0.00^{+14.1}_{-0.00}$	$57.3^{+0.21}_{-27.7}$	$0.00^{+16.6}_{-0.00}$
19	308.55480	60.115587	308.54060	60.108520	3	647.2	$0.12^{+0.11}_{-0.12}$	$0.00^{+0.76}_{-0.00}$	$0.00^{+0.67}_{-0.00}$	$0.00^{+0.62}_{-0.00}$
20	308.55480	60.122654	308.54060	60.115587	6	647.2	$0.00^{+0.24}_{-0.00}$	$0.00^{+1.21}_{-0.00}$	$2.25^{+0.52}_{-1.83}$	$0.00^{+1.29}_{-0.00}$

Note. — Note: The RA-NE, Dec-NE, RA-NW, Dec-NW, RA-SE, Dec-SE, RA-SW, and Dec-SW columns have been condensed down to RA-E, RA-W, Dec-N, Dec-S columns to save space in this thesis. The Tran et al. (2023) and machine readable table contain these columns. Some of the values have been rounded to save space. The machine readable table provided will have the full precision. Area listed is not corrected for inclination. i= index; N = number of stars

Table 2.4. Sample of SFRs over Time - (cont'd)

SFR 7.0-7.1 1e-3$M_\odot/yr$	SFR 7.1-7.2 1e-3$M_\odot/yr$	SFR 7.2-7.3 1e-3$M_\odot/yr$	SFR 7.3-7.4 1e-3$M_\odot/yr$	A_V	dA_V	Age Myr
$1.19^{+0.12}_{-1.04}$	$0.00^{+0.64}_{0.00}$	$0.00^{+0.58}_{0.00}$	$0.00^{+0.90}_{0.00}$	0.80	0.00	11.1
$0.00^{+0.43}_{-0.00}$	$0.00^{+0.42}_{-0.00}$	$1.04^{+0.26}_{-0.83}$	$0.00^{+0.86}_{0.00}$	0.95	0.05	17.8
$0.00^{+1.22}_{-0.00}$	$0.00^{+1.20}_{-0.00}$	$0.00^{+2.76}_{0.00}$	$5.80^{+0.21}_{5.80}$	0.95	0.30	18.9
$0.00^{+0.82}_{-0.00}$	$0.00^{+0.09}_{-0.00}$	$0.00^{+1.88}_{0.00}$	$0.00^{+4.20}_{0.00}$	1.35	0.00	4.4
$0.00^{+8.68}_{-0.00}$	$0.00^{+13.9}_{-0.00}$	$17.5^{+3.98}_{17.5}$	$0.00^{+31.6}_{-0.00}$	1.20	1.05	13.2
$0.00^{+2.81}_{-0.00}$	$3.37^{+2.82}_{-2.83}$	$0.00^{+5.23}_{0.00}$	$11.9^{+10.1}_{8.37}$	1.40	0.00	17.5
$0.00^{+6.28}_{-0.00}$	$13.4^{+0.00}_{-11.7}$	$0.00^{+15.6}_{0.00}$	$0.00^{+46.4}_{0.00}$	1.50	0.05	11.3
$0.00^{+13.3}_{-0.00}$	$0.00^{+11.0}_{-0.00}$	$0.00^{+16.7}_{0.00}$	$0.00^{+37.0}_{0.00}$	1.50	1.50	7.1
$0.00^{+0.53}_{-0.00}$	$0.00^{+0.82}_{-0.00}$	$1.24^{+2.02}_{0.92}$	$0.00^{+2.81}_{0.00}$	1.40	0.00	16.6
$0.00^{+1.17}_{-0.00}$	$0.00^{+1.23}_{-0.00}$	$0.00^{+1.96}_{0.00}$	$0.00^{+4.79}_{0.00}$	1.45	0.00	7.1

Note. — Note: The RA-NE, Dec-NE, RA-NW, Dec-NW, RA-SE, Dec-SE, RA-SW, and Dec-SW columns have been condensed down to RA-E, RA-W, Dec-N, Dec-S columns to save space in this thesis. The Tran et al. (2023) and machine readable table contain these columns. Some of the values have been rounded to save space. The machine readable table provided will have the full precision. Area listed is not corrected for inclination. i= index; N = number of stars

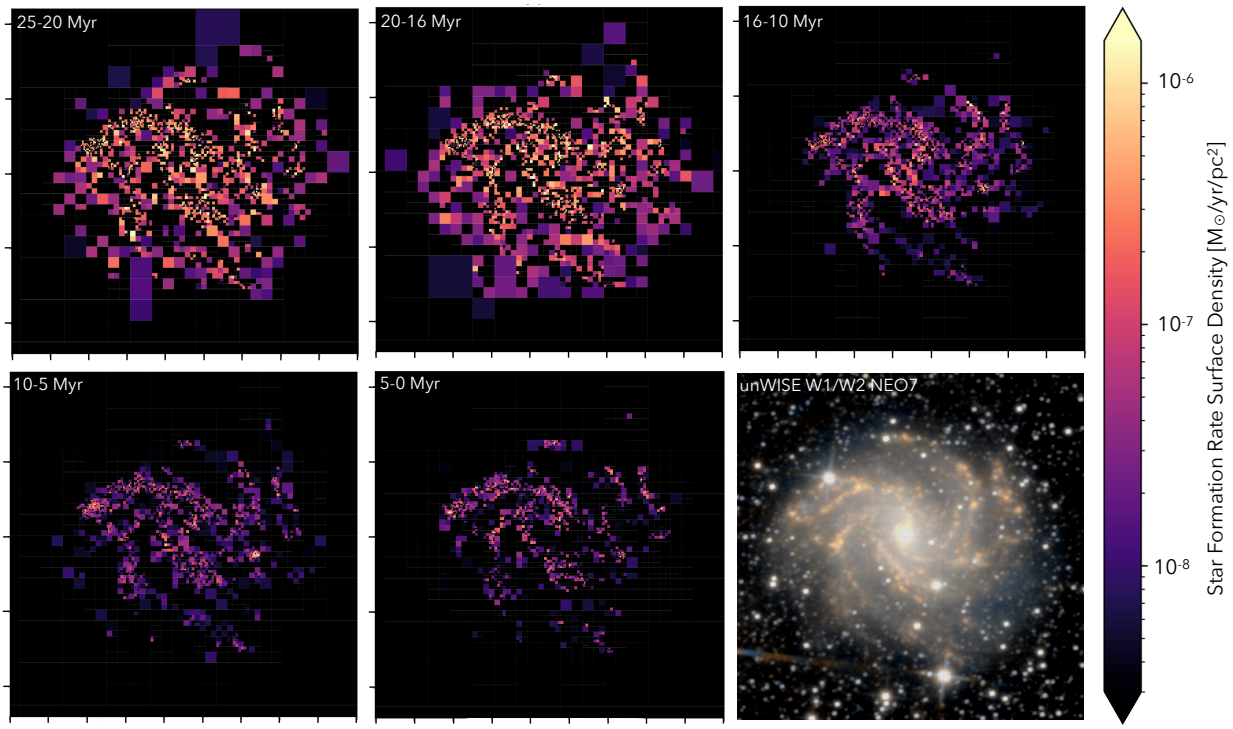

Figure 2.5 Maps of the spatially-resolved star formation rate as a function lookback time with linear time bins (RA=[60.03-60.226],dec=[308.50,308.95]). Each subfigure has the same dimensions, tick marks, and extent as Figure 2. We include a color image from the unWISE catalog (Meisner et al., 2022) in W1 and W2 filters from NEO7, taken from legacysurvey.org.

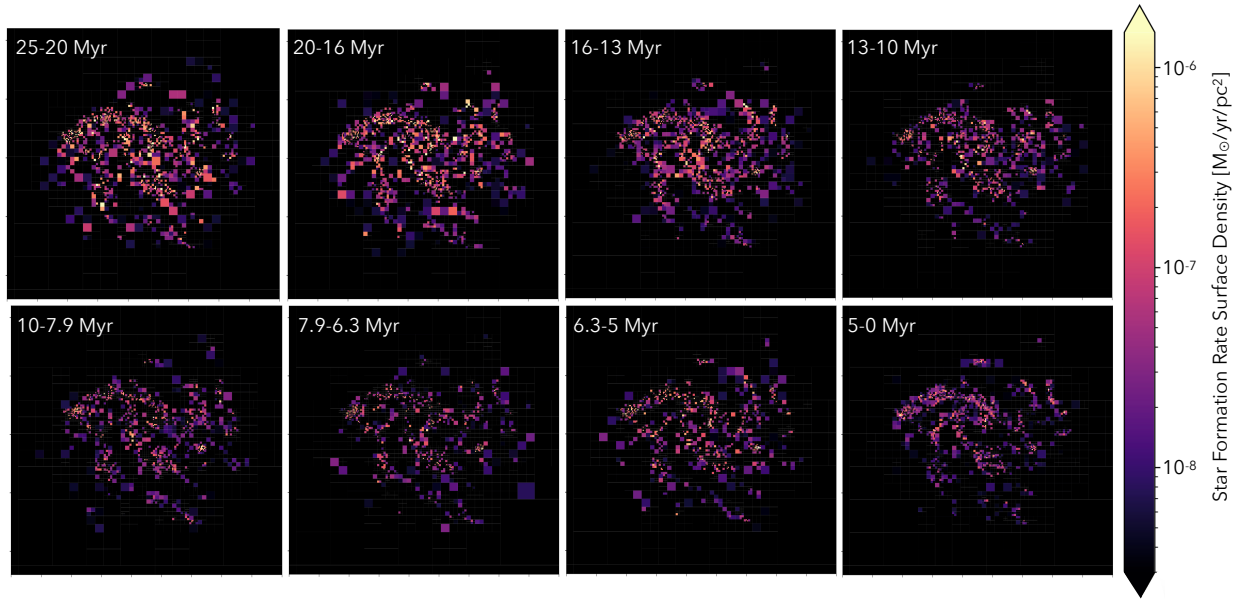

Figure 2.6 Maps of the spatially-resolved star formation rate as a function lookback time with logarithm time bins (RA=[60.03-60.226],dec=[308.50,308.95]). These plots use the same data as Figure 2.5, but use logarithm time bins to produce better time resolution at recent times. Each subfigure has the same dimensions, tick marks, and extent as Figure 2.

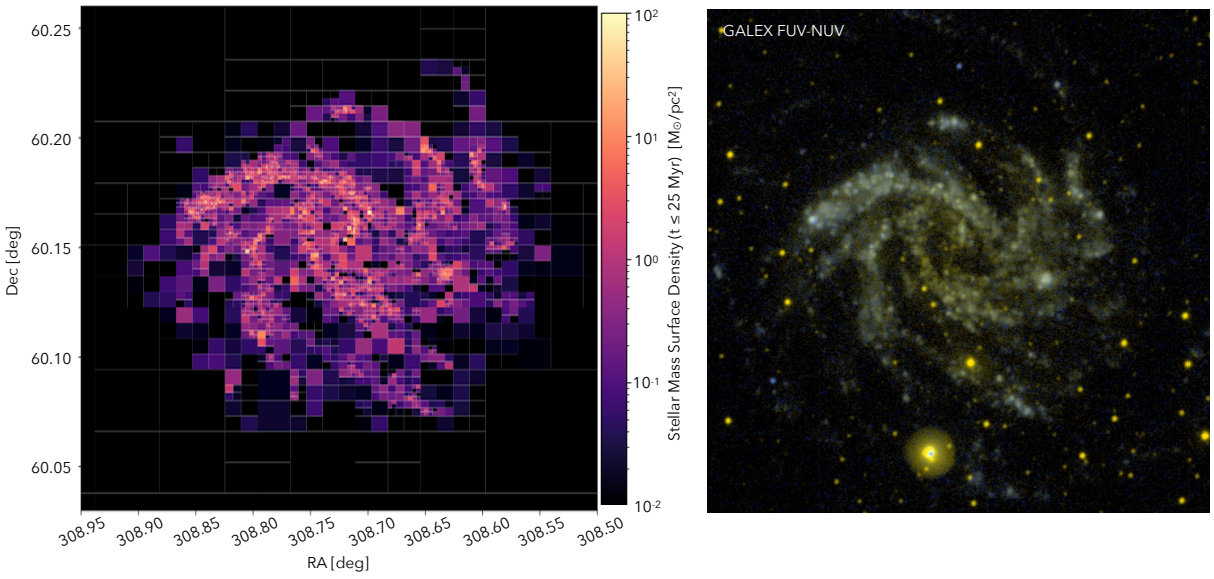

Figure 2.7 Left: Total stellar mass formed per unit area in the past 25 Myr. Right: GALEX NUV-FUV color image taken from legacysurvey.org.

We integrate the time bins to calculate the total mass formed over the last 25 Myr. In the left panel of Figure 2.7, we show the resulting mass surface density map. A majority of the recently formed mass is in the spiral arms, though there is a significant population of young stars outside of the spiral arms. The spatial distribution of the mass formed traces the resolved UV photometry of the galaxy fairly well. Our data and mass map look far more extended, particularly in the northwest and southeast arms, than the GALEX color image (right panel of Figure 2.7) due to the increased sensitivity of our data (Figure 2.1). Our methods seem to be more sensitive to older star formation than that of GALEX (which would probe <10Myr), as these features appear most prominently in the 16-20 Myr time bins of Figures 2.5 and 2.6.

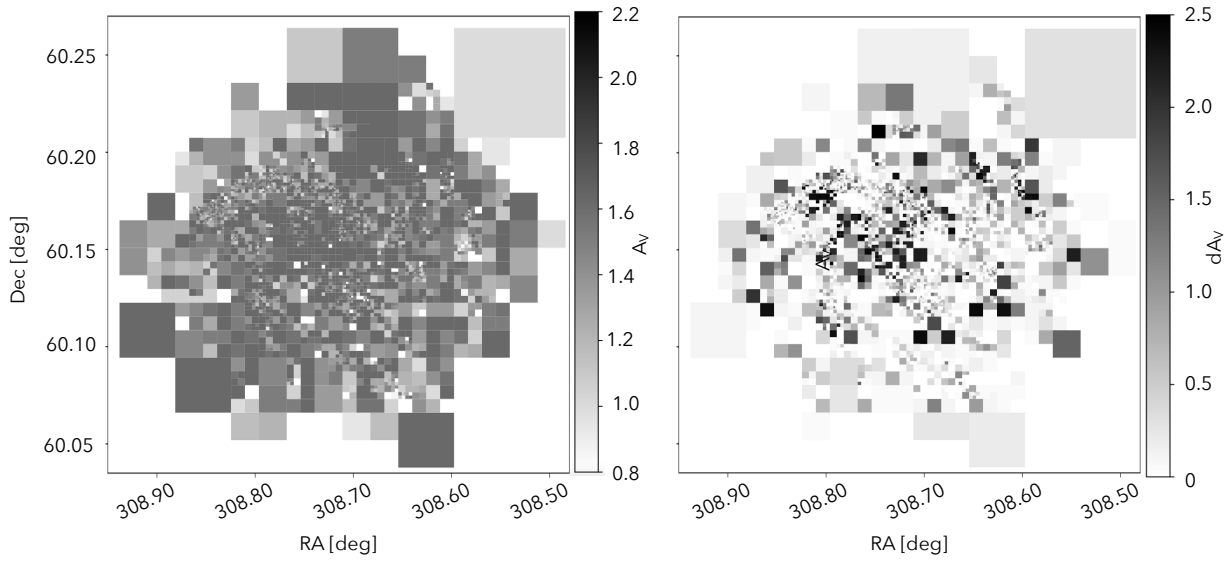

Figure 2.8 Left: Best fit foreground extinction A_V of NGC 6946. Right: Best fit differential extinction dA_V of NGC 6946.

2.3.2 Extinction Maps

We recovered foreground extinction fairly uniform with mean of 1.4 and standard deviation of 0.3 (Figure 2.8, left panel). This is slightly higher than the extinction of A_V=0.938 from Schlafly & Finkbeiner (2011). We present the differential extinction map in the right panel of Figure 2.8. The areas of high differential extinction are in the spiral arms and appear to be very clumpy. Approximately 17% of the cells have high measured differential extinction (dA_V >1), which could mean that we cannot detect some of the older stars in those grids. For more detail, see Section 2.3.5. The measured differential extinction show no correlation with ages measured in Section 2.4.2.

Table 2.5. Global SFR over Time

Time Bin [Myr]	Time Bin [log(yr)]	SFR $[M_\odot/yr]$
4-5	6.6-6.7	$4.93^{+0.22}_{-0.23}$
5-6.3	6.7-6.8	$7.21^{+0.58}_{-0.52}$
6.3-8	6.8-6.9	$4.37^{+0.42}_{-0.36}$
8-10	6.9-7.0	$5.80^{+0.45}_{-0.40}$
10-12.5	7.0-7.1	$7.33^{+0.70}_{-0.66}$
12.5-16	7.1-7.2	$12.81^{+1.04}_{-0.95}$
16-20	7.2-7.3	$22.84^{+2.67}_{-3.18}$
20-25	7.3-7.4	$23.82^{+3.81}_{-2.81}$

2.3.3 Global SFH

To derive a global star formation history for the galaxy, at each time bin, we integrate the SFR over all cells. We calculate the uncertainties due to the number of stars in the cells by adding the uncertainties of each spatial bin in quadrature. Then we bootstrap the uncertainties across spatial bins by sampling the number of cells 10,000 times with replacement to account for uncertainties due to binning the stars into cells. We then add the uncertainties obtained via bootstrapping to the random uncertainties in quadrature. We present these global star formation rates in Table 2.5 and plot them in Figure 2.9.

To obtain the star formation rates in the past 10 Myr, we integrated the star formation rates over time to obtain total mass formed in the past 10 Myr, then divided that total mass by 10 Myr. We calculated the uncertainties by adding the uncertainties of each time bin in quadrature. We find the global star formation rate over the past 10 Myr to be roughly constant at $5.31^{+0.88}_{-0.78} M_\odot$/yr, shown in Figure 2.9. We did the same for the global star formation rate 16-25 Myr ago, obtaining an SFR of $23.38^{+4.65}_{-4.25} M_\odot$/yr. The SFR 16-25 Myr ago was roughly five times larger than the current ($\leq$ 10 Myr) star formation rate, with a monotonically decreasing SFR in the 6 Myr in between the two epochs.

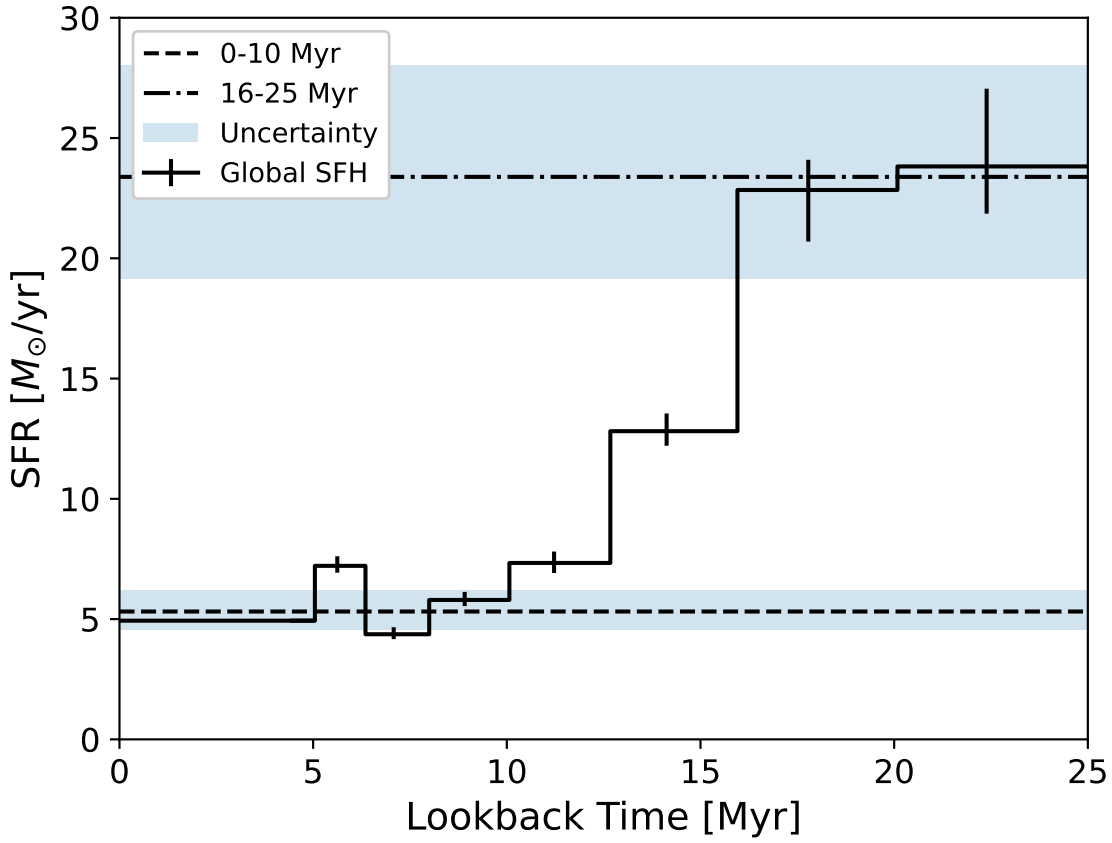

Figure 2.9 Coadded star formation rates across all spatial bins as a function of lookback time. The global star formation rate is much higher 16 Myr ago and has decreased in to be a more steady rate in the past 10 Myr.

2.3.4 Reliability of the Younger Time Bins

As with SFR measurement techniques that rely on UV data, dust is a big challenge to measuring young star formation. Stars are born from giant molecular clouds and are obscured by dust until a massive star forms, ionizes its birth cloud, clears out the material (Lada & Lada, 2003). This makes young stars incredibly challenging to observe. Our technique requires that the young stars are observable to measure star formation. The uncertainties due to dust for SFRs older than 8 Myr decrease significantly. Young stellar clusters emerge from the giant molecular clouds on timescales of 8 Myr, with very few stars remaining embedded after that (Corbelli et al., 2017). Additionally, upon visual inspection of WISE and GALEX images (Figures 2.5 and 2.7, respectively), the star formation in the 0-5 Myr time bin seems well recovered. This suggests that it is unlikely that a significant fraction of the star formation is being missed, though additional measurements of SFR using infrared are necessary better constrain the impacts of dust.

We check the impact of the blends on the reliability of the SFR in the young time bins. Our choice to include the 16 sources flagged as blends in 14 cells had been made to include as many young stars as possible in our MATCH fits. We ran MATCH again on two of these cells removing the blends from the observed CMD. We find that there is no impact on the measured SFH of these two cells. However, without the blends, the uncertainty of the SFR in the youngest time bin decreased by two orders of magnitude. The inclusion of the blends in our CMD-fitting gives us more conservative uncertainties on the SFRs of the younger time bins.

Additionally, we compare the SFR measurements to that from the literature. The current SFR is consistent with SFRs measured via methods probing the youngest stars. Previous measurements of the SFR within the last 5 Myr from Hα measurements find an SFR of $\sim$ 4 $M_{\odot}$/yr (no reported uncertainties, Sauty et al. (1998)) and 5.7 $\pm$ 1.7 $M_{\odot}$/yr Botticella et al. (2012), which both agree with our measurement of $4.93^{+0.22}_{-0.23}$ (Table 2.5, row 1) within uncertainties. Kennicutt et al. (2011) measured a $\lesssim$ 5 Myr SFR of $\simeq$ 7.1 $M_{\odot}$/yr with $H\alpha$

and 24 μm observations, with no uncertainties reported. This higher star formation rate is more consistent with our SFR in the 5-6.3 Myr time bin of $7.21^{+0.58}_{-0.52}$ (Table 2.5, row 2). Measurements of the SFR obtained with far-ultraviolet (FUV) tend to probe timescales over the past 10 Myr. Botticella et al. (2012) measures a FUV SFR 9.1 $\pm$ 2.7 $M_{\odot}$/yr, which is more consistent with our measurements of the SFRs 10-16 Myr ago, $7.33^{+0.70}_{-0.66}$ and $12.81^{+1.04}_{-0.95}$ (Table 2.5, rows 5-6).

2.3.5 Reliability of Older Time Bins

Another challenge of utilizing UV data to measure star formation rates is that UV primarily probes young star formation, as seen in Figure 2.3 where the log(age)=7.4 isochrone lies very close to the completeness limit of our data. This limitation is reflected in the high uncertainties (at least an order of magnitude higher than the rest of the time bins) in the star formation rate in the oldest time bin, in Table 2.5. Thus we exclude the log(age)=7.4-7.5 time bin from the our analysis in the paper. In addition, we perform several tests to check the reliability of the SFR in the two oldest time bins (log(age)=7.2-7.3 and log(age)=7.3-7.4) by simulating model CMDs from the resulting SFRs.

We perform tests to check the impact of our chosen completeness limits on our measured star formation rates in the two oldest time bins. First, we check that the model CMDs created accurately model the observed CMDs for a selection of cells at varying stellar densities. We create these model CMDs by using the same parameters (i.e. completeness limits, binary fraction) we used to fit the star formation histories, as well as the output best fit metallicities and star formation rates from our results. We then check that the model has enough stars in the oldest two time bins log(age)=7.2-7.3 and log(age)=7.3-7.4 to allow for good measurements.

We also test for density-dependent effects which might arise due to the brighter completeness limit in the highest density regimes. We want to ensure that the measured SFRs of the oldest two time bins is consistent with the number of stars in their observed CMDs and reflect an accurate measurement. We check this by performing two tests. First, to measure

the minimum expected percentage of older stars, we simulate constant star formation histories at different constant SFRs to measure the percentage of older (log(age)=7.2-7.4) stars out of the total (log(age)=6.6-7.4) at varying stellar densities. To check the impact of the input SFR on the percentage of older stars, we choose an SFR of 13.17 $M_{\odot}$/yr (the average global SFR), 0.1 $M_{\odot}$/yr (the highest measured SFR of a cell), and 0.005 $M_{\odot}$/yr (an average SFR value in a cell). We present the resulting systematics from these tests below (Table 2.6). There is some stochasticity in the percentage of modeled older stars for a constant SFH at SFR=0.005 $M_{\odot}/yr$ likely due to the small numbers of stars in the model. Second, we measure the percentage of observed stars that fell in the two oldest time bins for varying stellar densities in a selection of spatial cells that have a spike in SFR in the older time bins. For the highest stellar densities ($\geq$ 12 stars/arcsec^2), the log(age)=7.2-7.3 and 7.3-7.4 time bins contain 20 $\pm$ 10% of the total number of stars, whereas the lower stellar density bins have 26 $\pm$ 10% of the total number of stars. Fortunately, there are only 5 cells that have these high densities, which is not significant enough to impact the high measured global SFR in the older time bins. The lower density bins have a sufficient percentage of stars above the minimum expected percentage to have the accurate SFRs measured in the oldest time bins, appearing to be less impacted by the completeness limit concerns than the 5 cells in the high density regime.

Finally, we compare the SFR measured in the oldest time bins to that obtained via supernova rates, which probes older star formation, from 30 Myr (assuming single star evolution) to 100 Myr (assuming binary star evolution; Jennings et al. (2014); Smartt (2009); Zapartas et al. (2021)) and requires an SFR of at least 12.1 $\pm$ 3.7 $M_{\odot}/yr$ Eldridge & Xiao (2019). We convert the measured SFR, ψ(t), of the two oldest time bins to an estimated core-collapse supernova rate, R(t)$_{CC}$. We utilize the formalism from Blanc & Greggio (2008), using the same assumptions (all stars in the suitable mass range $m_u^{CC} - m_l^{CC}$ supernova, the number fraction of stars that supernova in the time range and number of stars per unit mass of the stellar generation do not vary with time, since the time range we are looking at is very short) and resulting equation (Equations 2.1 and 2.2) from Botticella et al. (2012).

Table 2.6. Percentage of Modeled Older Stars for Simulated Constant SFH at SFR of 13.17 $M_\odot$/yr (the average global SFR), 0.1 $M_\odot$/yr (the highest measured SFR of a cell), and 0.005 $M_\odot$/yr (an average SFR value in a cell)

Density Bin [stars/arcsec^2]	SFR = 13.17 $[M_\odot/yr]$	SFR = 0.1 $[M_\odot/yr]$	SFR = 0.005 $[M_\odot/yr]$
0-2	18%	18%	25%
2-4	18%	19%	15%
4-6	18%	18%	14%
6-8	17%	18%	15%
8-10	17%	17%	20%
10-11	17%	16%	10%
11-12	18%	17%	22%
12-13	15%	11%	3%
13-18	14%	11%	19%

$$R(t)_{CC} = K_{CC} \times \psi(t) \tag{2.1}$$

where

$$K_{CC} = \frac{\int_{m_l^{CC}}^{m_u^{CC}} \phi(m)\, dm}{\int_{m_l}^{m_u} m\phi(m)\, dm} \tag{2.2}$$

For consistency, we choose the IMF, $\phi(m) \propto m^{-\alpha_i}$, to be the Kroupa IMF ($\alpha_0 = +0.3,\ 0.01 \leq m/M_\odot < 0.08;\quad \alpha_1 = +1.3,\ 0.08 \leq m/M_\odot < 0.50;\quad \alpha_2 = +2.3,\ 0.50 \leq m/M_\odot$), Kroupa (2001)). We utilize the minimum progenitor masses to supernova for log(age)=7.2-7.3 to be 11.73 $M_\odot$ and log(age)=7.3-7.4 for 10.28 $M_\odot$ from the Padova stellar evolutionary models (Marigo et al., 2008) used in the calculation of the SFH.

For log(age)=7.2-7.3, we derive a core-collapse supernova rate of $0.15^{+0.02}_{-0.02}$ SN/yr. For log(age)=7.3-7.4, a ccSN rate = $0.19^{+0.03}_{-0.02}$ SN/yr, with uncertainties only propagated from SFR in the two time bins. This doesn't account for the systematic uncertainties due to the IMF and estimated progenitor mass. We estimate the uncertainty due to choice of IMF

by comparing the ccSN rates obtained with the high-mass IMF from Weisz et al. (2015). The ccSN rate obtained for log(age)=7.2-7.3 is $0.09^{+0.01}_{-0.01}$ SN/yr and $0.12^{+0.02}_{-0.02}$ SN/yr for log(age)=7.3-7.4, which is more aligned with the observed supernova rate of 0.1 SN/yr (Eldridge & Xiao, 2019). A 6% change in the slope of the IMF changes the ccSN rate by 60%, dominating the uncertainty of this calculation. We estimate the uncertainty due to progenitor mass by selecting progenitor masses from two additional stellar evolutionary models, PARSEC (Bressan et al., 2012) and Geneva (Ekström et al., 2012), and taking the standard deviation the ccSN rate obtained with the three different models. The uncertainty due to choice of progenitor mass is 0.7% and 4% for log(age)=7.2-7.3 and log(age)=7.3-7.4, respectively.

2.4 Discussion

In Section 2.4.1, we analyze two regions with high recent star formation and present their star formation histories. Finally, in Section 2.4.2, we examine the relationship between stellar density and age.

2.4.1 Local Star Formation History

We analyze two regions with high star-forming activity, the Hodge Complex (Hodge, 1967) roughly centered at 20:34:34.80 +60:08:18.60 and the HII region at the tip of the northeast spiral arm roughly centered at 20:35:22.57 +60:10:14.70. The cells of the regions of interest used in this analysis are flagged in the machine readable table.

To obtain the star formation histories of these regions, we sum the star formation rates of each cell in the region per time bin. We then add the random uncertainties in quadrature. The locations of the regions and their star formation histories are presented in Figure 2.10.

The Hodge Complex is a super star cluster containing multiple young star clusters and has been extensively studied due to the high concentration of star formation Sánchez Gil et al. (2009); Efremov et al. (2007); Efremov & Moiseev (2016). We present the star formation history of this region in the lower left corner of Figure 2.10. This region appears to have

constant star formation over the past 6.3-25 Myr with a peak in star formation in around 5-6.3 Myr and drop in star formation in the most recent 5 Myr. Interestingly, despite being a mere 1295 square arcseconds, which is 0.05% of the total size of our coverage area, this tiny region contains 3% of the total mass formed up to 6.3 Myr and 1.8% of the total mass formed up in the past 25 Myr. This region has had a more recent star formation episode than seen for the globally decreasing star formation rate.

Another region of interest is the HII region in tip of the northeast spiral arm. Unlike the Hodge Complex, the star formation history of this region roughly follows the star formation history of galaxy. Similar to the Hodge Complex, this small region of the galaxy contains a significant portion of the recent star formation in the galaxy. Despite it being 0.05% of our total coverage (roughly 1334 square arcseconds), this region contains 5.6% of total mass of NGC 6946 formed in the last 6.3 Myr and 3.9% over the last 25 Myr. There is a large peak in older star formation 20-25 Myr ago relative to the flatter SFH in the past 20 Myr. Since the global SFH has a more gradual decrease in SFR over time, we check that this peak in SFR is not due to a systematic related to completeness. We check SFRs of the locations with the highest stellar density and find 1.5% of SFR in oldest time is attributed to those high density regions, making an insignificant contribution to the high SFR.

Ultimately, these regions of interest are only a small portion of the young star formation in NGC 6946. This points to overall star formation across the galaxy contributing to the peak in the global SFH.

2.4.2 Density versus Age

Initially, we measured the characteristic age of the population in each cell by randomly sampling their star formation histories 50,000 times. We then obtain 16th, 50th, and 84th percentile time bins. Due to the the double peak distribution of many of the star formation histories, we found no correlation between stellar density and characteristic age for this population.

Thus instead of looking at the characteristic age of the population, we find the youngest

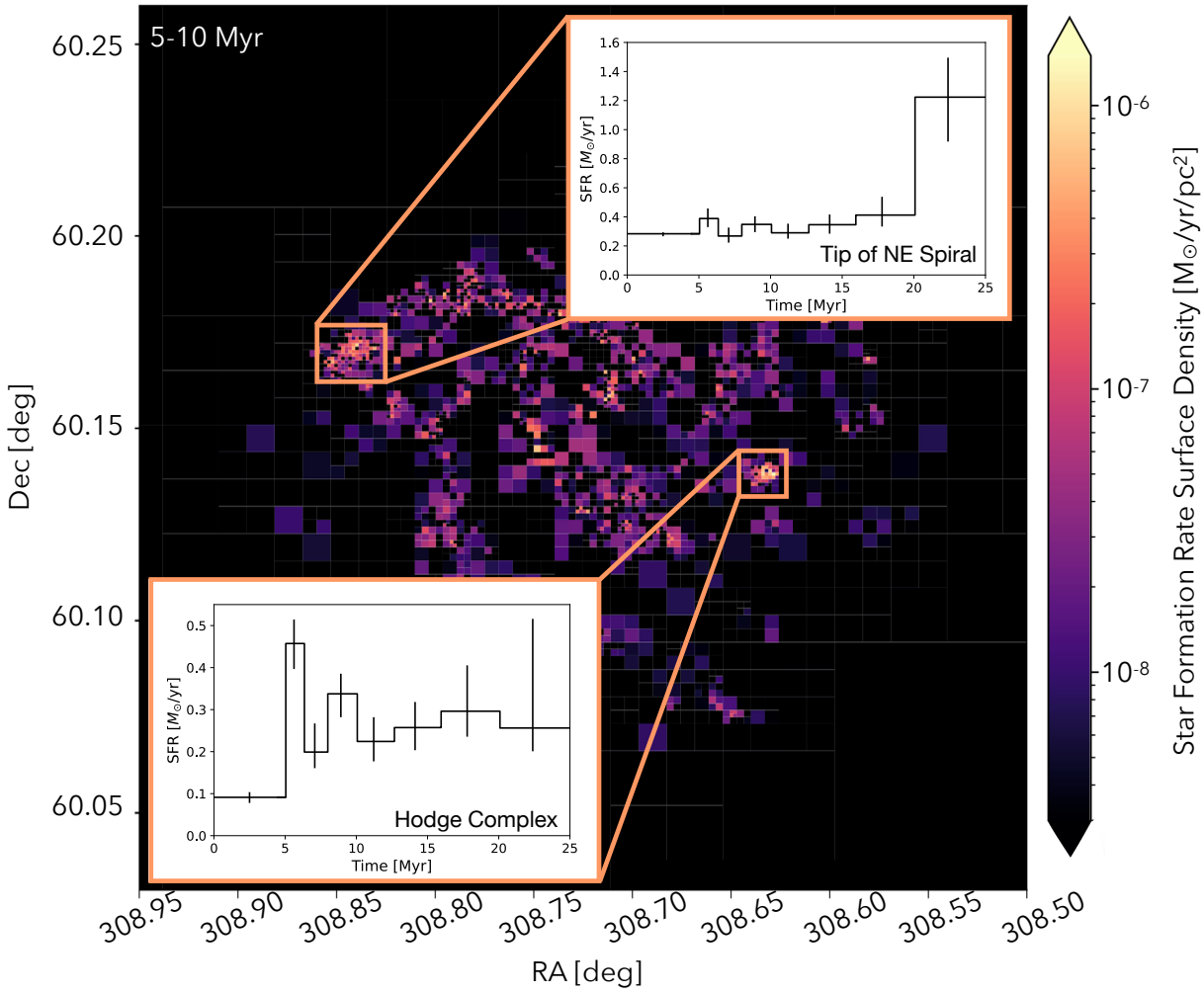

Figure 2.10 Coadded star formation histories of two regions of interest, the large HII region in the northeast spiral arm and Hodge Complex, with the approximate locations of the regions used in the local star formation history. Exact indices of the regions used in the star formation history calculations are flagged in the machine readable table.

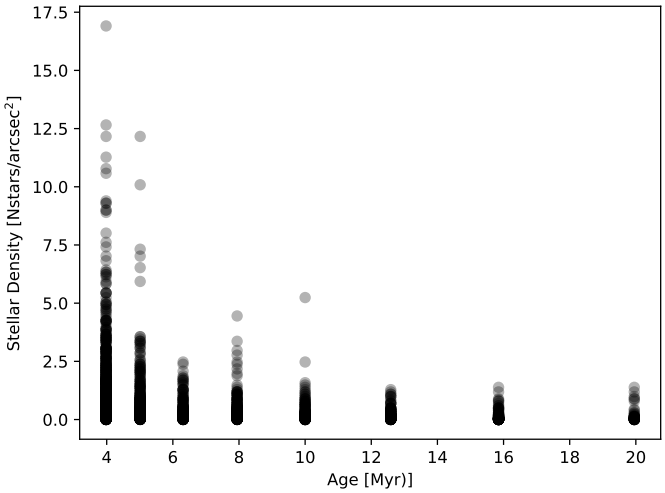

Figure 2.11 This plot shows the relationship between the age of the youngest detectable population, described in Section 2.4.2, and the stellar density, described in Section 2.2.4, where each point represents a cell. There seems to be a correlation between stellar density and the youngest ages detected, where the younger the stars in the cell are, the more dense that cell is. This correlation seems to flatten after 12 Myr.

age bin in which we detect star formation in each cell, using the following criteria: the SFR of the age bin is at least 3% of the total star formation rate, the age bin contains 1% of the total mass formed, and and the lower bound SFR uncertainty of that time bin must be greater than or equal to zero. In Figure 2.11, we see that the youngest detected population are denser, with the stellar density remaining between 0-2.5 stars/arsec^2 after 12 Myr. A possible explanation is that stars have migrated from their initial site of formation over 12 Myr to populate the field. This is consistent with the timeline of stars emerging for their giant molecular clouds by roughly 8 Myr (see Section 2.3.4) then populating the field over time. More work will need to be done to confirm that stellar migration is being observed. We plan to model this in our future work.

2.5 Conclusions

In this paper, we presented the spatially-resolved star formation history of NGC 6946 in the last 25 Myr, measured using resolved NUV stellar photometry. We implemented a quadtree algorithm to devise a spatial grid, and we measured the SFH independently for each cell using CMD-fitting. We summarize our main findings below.

- We measure the global SFR over the last 25 Myr to be $13.16^{+0.91}_{-0.79} M_{\odot}/yr$.

- 16-25 Myr ago, the SFR was $23.38^{+2.43}_{-2.11} M_{\odot}/yr$. The SFR then monotonically decreases between 10-16 Myr, reaching a steady recent SFR in the past 10 Myr of $5.31^{+0.18}_{-0.17} M_{\odot}/yr$.

- We present the star formation histories of the Hodge Complex and the HII region at the tip of northeast spiral arm. Both contain a higher amount of recent star formation than expected for regions of their size. The Hodge Complex shows more recent star formation relative to the declining global star formation.

Chapter 3

AUTOMATED COMPUTER VISION CLUSTER AND ASSOCIATION CANDIDATE IDENTIFICATION IN THE FIREWORKS GALAXY

In this chapter, I apply additional analysis to the stellar photometry detailed in the previous chapter. I discuss my analysis technique for finding young star clusters in NGC 6946, specifically by creating an automated cluster and association candidate identification algorithm. I test this algorithm on using near-UV (NUV) photometry of high signal to noise sources in NGC 6946 obtained with Hubble Space Telescope (HST) Wide Field Camera 3 (WFC3) F275W and F336W filters. I identify 767 cluster and association candidates, fit the measured cluster luminosity function and discuss the trend in radii and brightness of clusters as a function of galactocentric radii. The bulk of this work has been submitted for peer review publication.

3.1 Introduction

Large, high-quality datasets of young massive star clusters for individual galaxies are essential for studying stellar, cluster, and galaxy evolution as well as star and cluster formation across different galaxies. In particular, they are useful for studying the luminosity function, mass function, radius-age mass relationship, radius-age relationship, the fraction of stars formed in long-lived clusters (Γ) for young massive stars (Johnson et al., 2012; Fouesneau et al., 2014; Johnson et al., 2015; Krumholz et al., 2019; Choksi & Kruijssen, 2021; Grudić et al., 2021; Brown & Gnedin, 2021). While the cluster luminosity function has been shown to be similar for different galaxies, the age and mass functions are far more varied depending on the age and mass bins utilized for the functions, in addition to evidence of high mass truncation at

cluster masses of $\sim 10^4 - 10^6 M_\odot$ (Whitmore, 2003; Larsen, 2006; Chandar et al., 2010; Messa et al., 2018; Gieles et al., 2006; Adamo et al., 2015; Johnson et al., 2017; Wainer et al., 2022).

In addition to their application for comparing star formation in different galaxies, catalogs of star clusters and associations are vital for studying the process of star formation within individual galaxies. For example, star formation in the central disks of galaxies tends to be more well-studied than star formation in the outer disks of galaxies. However, inner and outer disk environments have very different stellar surface densities and gas properties. The clusters detected in the outer disks of NGC 628, NGC 5457, and NGC 6946 (Yadav et al., 2021) tend to be more compact and significantly fewer in number. To fully characterize the differences between clusters at different galactic radii, we must have a large selection clusters that probe a wide range of galactic environments.

One of the most difficult challenges in producing star cluster and association catalogs is the complex selection effects intrinsic to identifying clusters which leads to difficulty interpreting cluster statistics. For example, within the Milky Way, the dust within the disk and the edge-on orientation of the disk makes it difficult to identify overdensities in the crowded the night sky. Moreover, projection effects make it very challenging to discern if the stars are gravitationally-bound. Outside of the Milky Way, to fully sample clusters in galaxies beyond the Local Group, the galaxy must be relatively face-on to minimize crowding and extinction and the stars within must be fairly well-resolved. For galaxies at these distances, we currently can only resolve the brightest, youngest, most massive clusters, making associations challenging to distinguish from clusters (Krumholz et al., 2019). These limitations create a barrier to directly compare results between galaxies with a wide range of distances and physical properties. As we push to resolve structures at larger distances with the new era of space telescopes, we must develop methods to quickly and repeatably identify populations of clusters.

To solve these issues, astronomers have had to get incredibly creative with the way we study star-forming regions. There have been several different automated methods developed to obtain star cluster and association catalogs - nearest neighbors (Gouliermis et al., 2010),

minimum spanning tree MST (Cartwright & Whitworth, 2004; Bastian et al., 2007), two-point correlation functions (Elmegreen, 2018), kernel density estimation (KDE) isopleths (Gouliermis et al., 2017), dendrograms (Rodríguez et al., 2019; Larson et al., 2020), single concentration index (Holtzman et al., 1992; Whitmore et al., 1993; Adamo et al., 2017; Cook et al., 2019), multiple concentration index (Thilker et al., 2022), and watershed method (Larson et al., 2023). However, the gold standard in cluster identification remains via identification by eye, as frequently done via citizen science (Johnson et al., 2012, 2015, 2022). With the variety of methods of identification and without a standard definition of what constitutes a "cluster" (see discussion in Johnson et al. (2015)), it is difficult to apply results derived for very specific cases and directly compare measurements between galaxies.

Our work is focused on the youngest and most massive clusters where there remains debate on whether a power law or Schechter (1976) function best fits the mass function (Gieles, 2009; Larsen, 2009; Chandar et al., 2010; Whitmore et al., 2010; Bastian et al., 2012; Turner et al., 2021; Wainer et al., 2022). To quantify what the functional form of the cluster mass function is, we need a large and well-characterized sample of young massive clusters across each galaxy using a method that can be applied to a range of galaxy types at different distances.

We make a major step forward in this endeavor by developing a search algorithm for a sample of young massive star clusters with resolved UV imaging. In the UV, massive stars, which have relatively short hot main-sequence lifetimes, outshine the older cool stars that dominate the galaxy stellar mass and crowd redder bands. After finding this sample of young clusters, we measure the physical parameters (luminosity, colors, etc.) of the stars within the clusters. We then measure the characteristics of the ensemble to constrain theories of cluster formation and evolution (Tran et al. in prep).

We modify and test a computer vision-based algorithm on NGC 6946, otherwise known as the Fireworks Galaxy, a face-on galaxy 7.8 Mpc away (Anand et al., 2018; Murphy et al., 2018; Johnson et al., 2023) with a high rate of supernovae and star formation, indicating there should be many young clusters within it. There are several young star-forming regions

detected throughout the galaxy, including several in the outer parts of its spiral arms, allowing for comparisons of clusters within the galaxy itself (Barnes et al., 2012; Yadav et al., 2021). Using the Kernel Density Estimation technique as applied by (Gouliermis et al., 2017; Larson et al., 2023) and resolved NUV photometry from the FUVS catalog (doi: 10.17909/gveq-8820) with a resolved young massive stellar population of approximately 81,000 (Tran et al., 2023), we create a computer vision algorithm to identify star cluster and association candidates.

This paper is structured as follows. In Section 3.2, we discuss the NUV HST observations and selection of sources for the cluster detection algorithm. In Section 3.3, we discuss the method and testing of the computer vision-based cluster candidate identification algorithm. In Section 3.4, we present the luminosities, colors, and radii of each cluster and resulting luminosity and the radii as a function of the galactic radii. In Section 3.5, we discuss the spatial distribution of luminosities and radii of the clusters. We compare the measured cluster luminosity function with those measured in different galaxies.

3.2 Observations and Source Selection

To probe the youngest resolved stars in NGC 6946, we utilize the Fireworks UltraViolet Survey photometric catalog, found in MAST at 10.17909/gveq-8820. This catalog is obtained from resolved NUV imaging taken in Hubble Space Telescope's (HST) Wide Field Camera 3 (WFC3) Ultraviolet (UVIS) channel in F275W and F336W filters. We use these images to obtain the integrated photometry of the detected cluster and association candidates. For more details on the observations (GO-15877; PI Levesque et al. (2019)), source detection, and photometry, see Tran et al. (2023).

We utilize the high signal to noise ratio (SNR ≥ 4) sources of the catalog as input for the algorithm. Unfortunately when applying quality cuts typical for resolved stellar catalogs, the majority of stars are removed from the central regions of clusters. Crowding makes it difficult to reliably fit a point spread function to stars in the center, but these poor measurements are still of value for measuring stellar densities. Because our method relies on stellar density maps of the galaxy, having a significant number of stars removed from the centers of clusters

makes measurements of stellar density less reliable. On the other hand, using a raw catalog with no quality cuts adds a lot of random noise into the data. Our simple SNR cut serves as a compromise between these two potential input source catalogs. This high SNR catalog is solely used for identifying the locations and contours of star-forming regions. To characterize the identified cluster candidates, we will utilize the catalog with additional quality cuts applied so that only reliable stellar brightness is used.

3.3 Cluster Candidate Identification Algorithm

There are many existing cluster candidate identification algorithms. However, the various methods have wide ranges in computational time and reliability for clusters that are highly hierarchical in structure (Schmeja, 2011) and are greatly dependent on data quality. Having a quicker and general scheme that works in a semi-resolved regime will be more useful for our large, resolved dataset. For this reason, we adapt a computer vision algorithm used for edge detection, Canny (1986). Instead of utilizing the typical implementations of Canny on imaging data (i.e. Tran et al. (2022)), we adapt the algorithm to be used on a map of stellar density obtained via Kernel Density Estimation (KDE), similar to methods in Gouliermis et al. (2017); Larson et al. (2023). This adapted algorithm allows us to obtain the edges of the clusters, allowing us to approximate which stars lie within the bounds of the cluster, rather than the usual method of applying a circular aperture. Because we only use young massive stars, these clusters often have asymmetric morphologies. Edge detection algorithms have been shown to better resolve substructures in such complex datasets, while humans are better at recognizing general patterns in the same data, similar to Gaussian edge detectors (McIlhagga, 2018). This distinction becomes important when there likely are clusters hidden within OB associations in our dataset.

In the rest of this section, we detail the creation and testing of artificial clusters inserted into the data, by-eye identification of cluster candidates in the real and synthetic clusters, the description of the algorithm, the detection of false positives, the input and output photometry of the synthetic clusters, and the completeness of the cluster/association catalog as a function

of age, mass, radius, magnitude, density, and color.

3.3.1 Synthetic Clusters

Prior to testing the algorithm on our observations, we create and insert artificial clusters into a section of the galaxy with a wide range of stellar densities. We choose a section of the galaxy to prevent fatigue from being a factor in by-eye cluster identification. Since we know the exact magnitudes and locations of the clusters and their stars, we can use these artificial clusters as a ground truth to test how well people can identify clusters by eye and the algorithm's performance at NGC 6946's distance and wavelength regime of this study. One thousand artificial clusters were generated by sampling the Kroupa initial mass function (Kroupa, 2001), from $10^3 - 10^6 M_\odot$, and populating Parsec isochrones from log(age/yr) = 6.6-7.5 (Costa et al., 2019b,a; Nguyen et al., 2022). using an extinction of $A_V = 0.938$ from Schlafly & Finkbeiner (2011), distance modulus of 29.4 from Anand et al. (2018); Murphy et al. (2018); Johnson et al. (2023). We removed the post-AGB stars from the Parsec V2.0 models since they were giving us unrealistically bright magnitudes and saturating the images. However, this only impacts clusters older than log(age/yr)=7.9, and therefore does not impact the quality of the artificial clusters. While we generated clusters with masses larger than $10^{5.75} M_\odot$, these clusters were ultimately excluded as they were not representative of our data upon visual inspection. Figure 3.3.1 summarizes the parameters applied to the fake clusters.

The synthetic sample covers a wide range of masses (likely to fully encompass the scope of potential cluster masses). The age range was chosen based off of work from Tran et al. (2023), where they detail the limits of the youngest and oldest age bins. The effective radii of the clusters are sampled directly from the effective radii distribution of M31 young cluster sample placed at the distance of NGC 6946. The distribution of the stars within the clusters are randomly sampled from a King profile (King, 1962) with tidal radius to core radius ratio of 30, which is the median value of Milky Way globular clusters. We recognize that young clusters tend to be less centrally concentrated than globular clusters, where the King profile

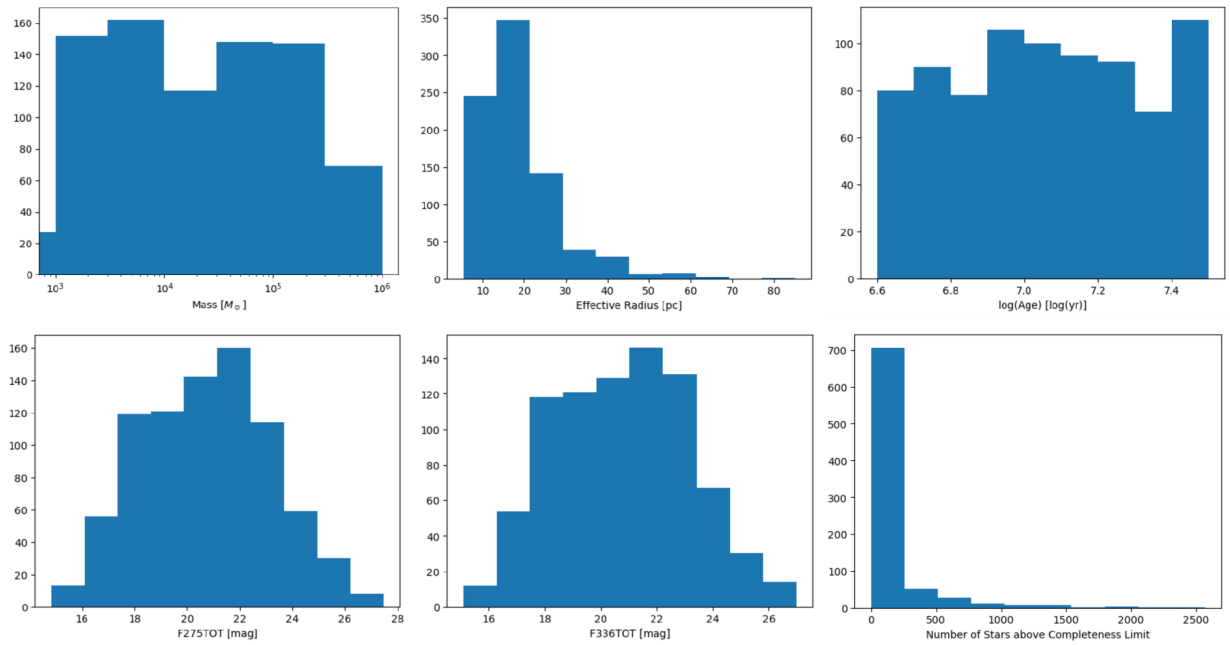

Figure 3.1 Top Left: Input masses ranging from $10^3 - 10^6$, Top Middle: Effective radius with majority of the clusters with radii less than 20 parsecs, Top Right: Roughly flat age distribution, Bottom Left: Integrated F275W magnitude, Bottom Middle: Integrated F336W magnitude, Bottom Right: Number of stars above completeness limit of 26 mag in both F275W and F336W, with completeness limits taken from Tran et al. (2023)

is derived. However, this simple distribution is the easiest way to model cluster profiles and provides a critical test of the algorithm.

3.3.2 By-Eye Cluster Candidates

To allow comparisons between our algorithm and the current gold standard, we visually identify clusters in a section of the galaxy on both the real data and the inserted artificial clusters. Three people separately identified star clusters, each person finding about 100 clusters in the real data. These clusters were then crossmatched, with 51 clusters matching. This crossmatching is a vital step to minimize individual misidentifications, as visual inspection becomes challenging as single stars and foreground stars can be mistaken for small clusters. For the artificial clusters, 386 clusters matched between the three coauthors, with each person identifying 430-480 clusters. Because our dataset comprises mostly of young clusters that are not centrally concentrated, we purposefully did not inform each person of what parameters they should be looking for within a cluster. This way, we can appropriately compare the nonparametric algorithm results to similar quality data as the by-eye identified samples. Each person was allowed to change the color stretch of the images and zoom in and out as well as select the size they believe each cluster should be.

3.3.3 Description of Algorithm

The algorithm, based on Canny edge detection (Canny, 1986), is summarized as follows- for details, see Tran et al. (2022). First, we use the photometric centroids (in pixels, Figure 3.2, top left) of sources in the catalog described in Section 3.2 to create a relative stellar density map (Figure 3.2, top second from the left). We determine the probability density distribution of stars in the dataset using 2-D Gaussian kernel density estimation. This is further described in Scikit-Learn's KernelDensity Function [1]. We choose a narrow bandwidth and finely divide the region into 16000 bins x 16000 bins to get the probability density distribution of roughly

[1]https://scikit-learn.org/stable/modules/density.html

each pixel. We utilize the probability density distribution as an analog for the stellar density distribution, as only relative values matter for the algorithm. Second, we perform unsharp masking on the stellar density map. We utilize the same Gaussian kernel density function described above, with a wider bandwidth to smooth over the stars (Figure 3.2, top third from the left). We then subtract the smoothed stellar density map from the original stellar density map to sharpen the edges of the clusters (Figure 3.2, top right). Third, we take the gradient of the sharpened stellar density map using a Sobel kernel (Sobel & Feldman, 1968) to obtain both the magnitude and direction of the gradient of stellar density (Figure 3.2, bottom left). Fourth, we thin the edges by performing non-maximum suppression of the gradient (Figure 3.2, bottom second from the left). We find the maxima of the gradient and interpolate over the edges. Fifth, we then determine a high and low threshold for an edge to be considered (Figure 3.2, bottom third from the left). Anything above the high threshold is a strong edge, and anything between the high and low thresholds are is a weak edge. For edges below the low threshold, it is not considered an edge. We utilize Otsu's method (Otsu, 1979) to perform automatic thresholding, with the value determined by this method for the low threshold and three times Otsu's threshold for the high threshold, which we have found optimal for our dataset. These chosen thresholds optimizes the number of real clusters previously detected by eye.

With the edges obtained from the Canny-based algorithm, we must ensure they are closed loops with no chords. Unfortunately, the usual method of applying morphological transformations (Bradski, 2000) didn't work with the high resolution of this dataset. Instead, we use the Felzenszwalb image segmentation algorithm to efficiently group the edges (Felzenszwalb & Huttenlocher, 2004). We then take the convex hull, or the smallest convex set containing the retrieved vertices, of the set of vertices (or the smallest convex set that contains the set of vertices). This gives us the vertices of the polygons that encompass the clusters. Because Felzenszwalb image segmentation produces oversegmented polygons on the more massive clusters, we merge the oversegmented polygons by taking the unary union of the polygons. We then remove all polygons containing foreground stars, flagged in the FUVS catalog based

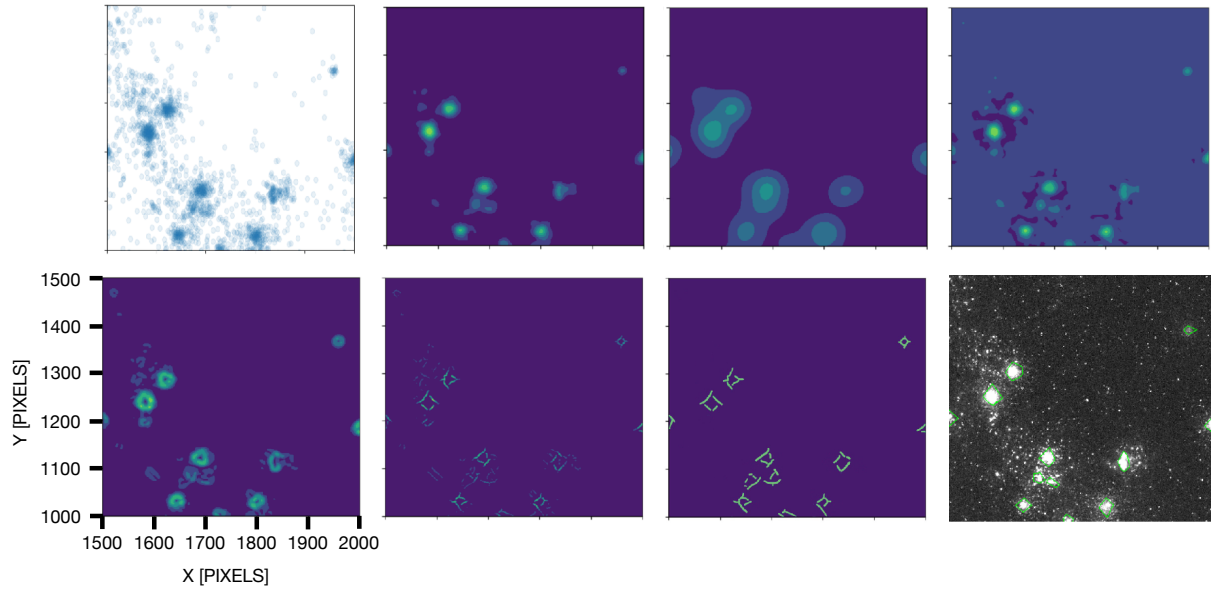

Figure 3.2 Top left: Centroids from FUVS photometry catalog; Top second from the left: Stellar density map from KDE; Top third from the left: Smoothed stellar density map; Top right: Unsharp masked stellar density map; Bottom left: Gradient of stellar density map; Bottom second from the left: Non-maximum suppression with interpolation to get edges to be one-pixel width. Bottom third from the left: Double threshold hysteresis to connect edges. Bottom Right: Final vertices of cluster/association candidates overlaid on the corresponding section of the F275W image. Each image displays the same section of the field in the eastern edge of NGC 6946 at different steps of the algorithm. For more details on the algorithm, see Section 3.3.3

on whether they have a measured proper motion from *Gaia* Data Release 2 (Gaia Collaboration et al. (2016); Gaia Collaboration et al. (2018)) and their measured color and magnitude. Additionally, we remove polygons containing less than 4 high-quality stars, as these polygons were determined using the high SNR catalog. See Figure 3.3 for the clusters/associations for a selection of cluster candidates that have been identified by eye and Figure 3.2 (bottom right panel) for the edges detected overlaid on the original image.

We then test this cluster candidate catalog by seeing if the clusters we've identified by eye as well as the artificial clusters we insert into the image are retrieved. Of the 822 inserted fake clusters, 337 were found by eye (crossmatched between three people), 409 were found by the algorithm. See Figure 3.3 for a region with clusters identified by the algorithm, clusters identified by eye, and the fake clusters that were not identified by either algorithm (false positives). Figure 3.4 shows an example of the artificial clusters detected by algorithm along with the color-magnitude diagrams of the recovered stellar photometry.

3.3.4 False Positives

We find 39 false positives of the 407 candidates the algorithm identifies in the data. We have fairly strict definitions of false positives, where anything candidate identified with a centroid is over two percent of the input radius away from the input fake cluster centroid (this percentage is fairly small because some clusters are overlapping), is considered a false positive. Since the fake clusters were inserted into real data, some of these false positives are potential cluster and association candidates. Figure 3.3 shows examples of the false positives identified by the algorithm (pink polygons). Another category included in the false positives are the fake clusters inserted have been merged into one cluster. The final category of false positive are the clusters that have been oversegmented, with the algorithm identifying multiple clusters instead of the one inserted artificial cluster.

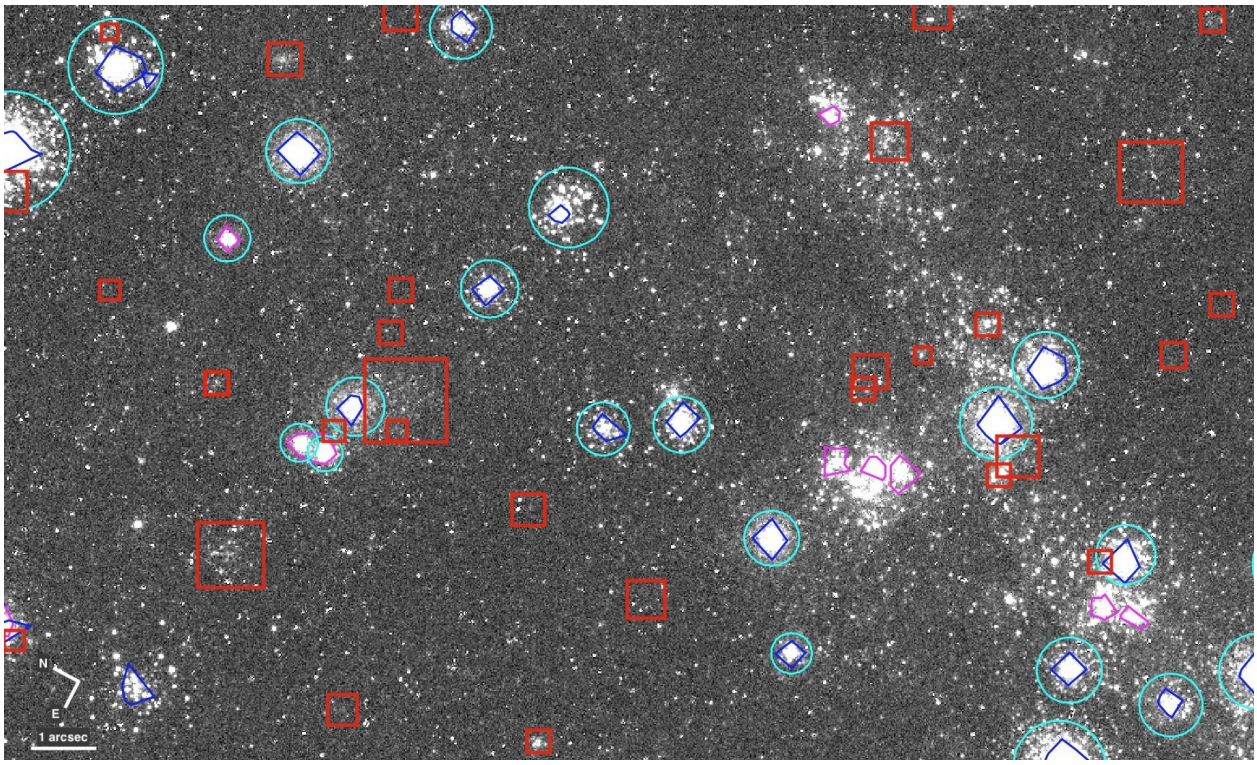

Figure 3.3 The cyan circles are the artificial clusters identified by eye (crossmatched between 3 people), the blue polygons are artificial clusters identified by the algorithm, the red squares are artificial clusters not detected by the algorithm or by eye, and the pink polygons are objects not inserted as fake clusters, but are identified by the algorithm. We consider these objects false positives. Some of these are potentially cluster/association candidates from the real data and some of these are fake clusters that have been combined into one cluster by the algorithm. The clusters missed by the algorithm are also not recovered by eye. There are a few objects ID'ed by the algorithm or by eye that was missed by the other.

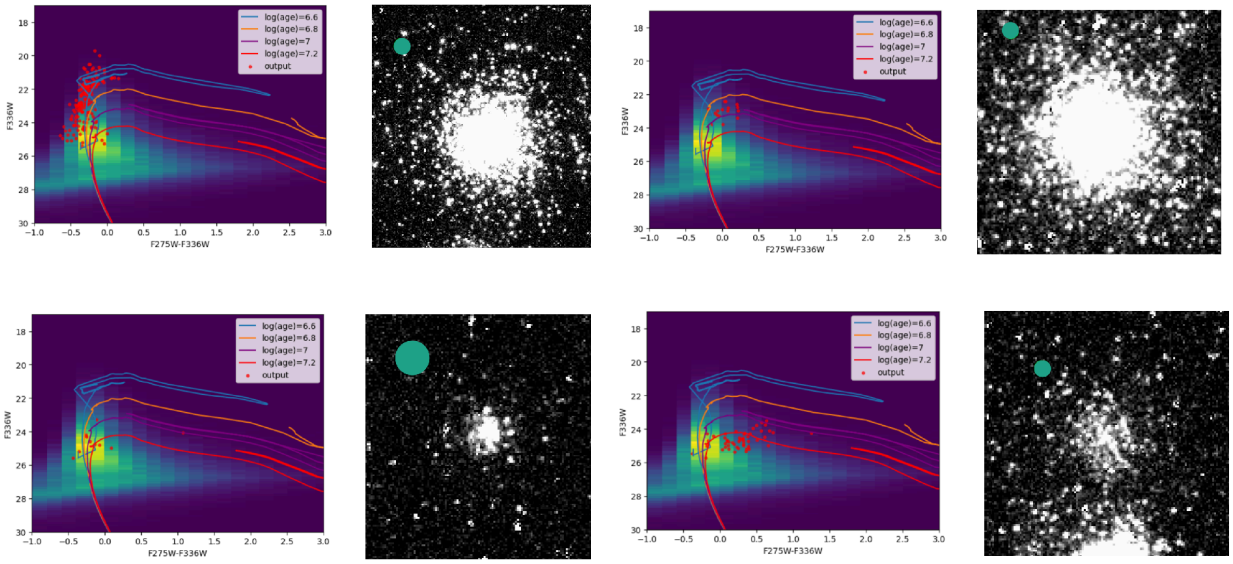

Figure 3.4 Color-magnitude diagrams (first and third columns from the right) and postage stamps (second and fourth columns from the right) of a selection of fake clusters identified by the algorithm. Each CMD is plotted over a Hess diagram of all the fake stars with SNR $\geq$ 4 inserted into the image. The red dots labeled "output" are the output F275W-F336W color and F336W magnitude of the inserted fake stars recovered by PSF-ftting. Isochrones of log(age/yr) = 6.6, 6.8, 7, and 7.2 are overplotted on the CMDs to give context regarding the ages of these artificial clusters. The fake clusters shown in the postage stamps are examples of the clusters of a variety of ages and masses recovered by the algorithm. One arcsecond radius green circle in the top left of each postage stamp for scale.

3.3.5 Input versus Output Photometry

Prior to analyzing solely the performance of the algorithm, we must first compare how the photometry we recover from the fake clusters compares to the input photometry. We utilize recovered photometry with a SNR ≥ 4 to create our stellar density maps. To understand how this compares to the input photometry, we plot the high SNR output photometry against the high SNR input photometry with F275W and F336W magnitudes brighter the detection limit of 26 mag. This detection limit is determined from artificial star tests performed in Tran et al. (2023). In Figure 3.5 we see that as the input average stellar density of stars increase, the recovered average stellar density hits a plateau around 100 stars/$arcsecond^2$. The scatter above the black line indicating equal input and output density for input densities less than 100 stars/$arcsecond^2$ are likely due to the recovery of real stars that were in the image prior to inserting the fake clusters. For the entire range of input stellar densities, there generally is smaller average output density compared to the input density. This limitation on output density is likely due to the impacts of crowding on the photometry of central regions of clusters. It becomes challenging to resolve stars in the center, making the cluster appear to be less dense in the center and have an overall lower average density.

3.3.6 Completeness

We use fake clusters to test the accuracy of the algorithm and by-eye identification. Figure 3.6 shows that the algorithm is more likely to detect clusters if they are bright in either filter (Figure 3.6, bottom left), if they are more massive (Figure 3.6, top left), and if they are more dense (Figure 3.6, bottom right). While one might expect 100% of the brightest clusters to be well detected by the algorithm, due to crowding at the centers of the clusters and thus the lack of quality photometry in those locations, the algorithm tends to oversegement these brightest clusters, which does not count as a detection. There is less of a dependence on age (Figure 3.6, top right), color (Figure 3.6, bottom middle), and radius (Figure 3.6, top middle). While it seems like older clusters would be less likely to be detected in the NUV

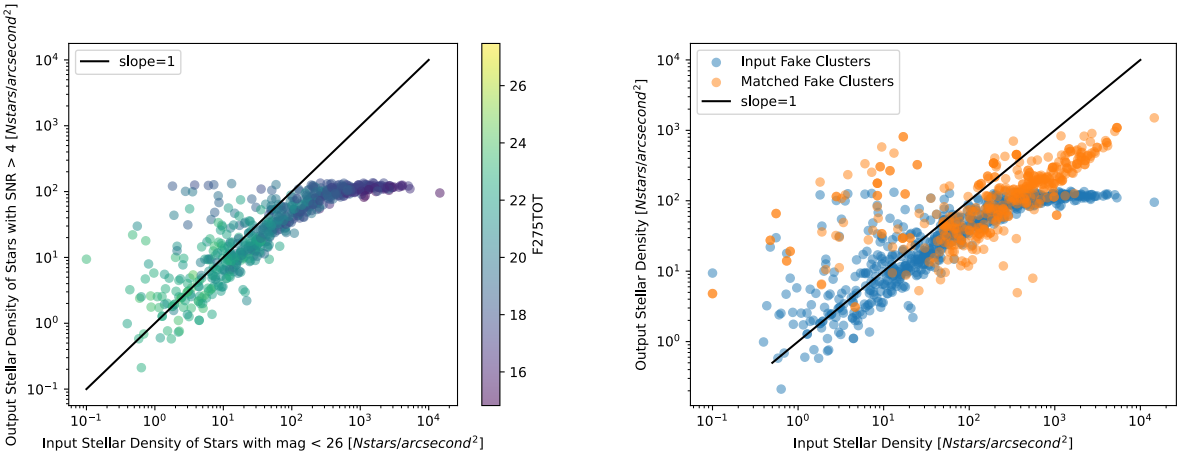

Figure 3.5 Input stellar density of clusters consisting of stars with signal to noise ratio above 4 and above the detection limit of 26 mag in both filters versus the output density of all clusters. This is the catalog of stars we utilized to make the stellar density maps utilized in the algorithm. The color of each point is the corresponding cluster's input integrated F275W magnitude, where the brightest clusters have the highest input densities and plateauing output densities.

filter, our oldest inserted clusters are quite bright in NUV. This in reality is unlikely to be true. These fake cluster simulations show that the algorithm is capable of detecting clusters at this distance (roughly 7.8 Mpc) and age (less than 25 Myr) with 50% completeness of masses at $10^{4.17}$ (or 14,800) $M_{\odot}$ and integrated F275W and F336W magnitudes of 19.44 and 19.5, respectively.

Finally, an important aspect of our analysis is to understand how the algorithm and stellar photometry impacts the integrated photometry of the clusters. Figure 3.7 shows the output integrated magnitude of each cluster as a function of their input integrated magnitude. There is a distinct and linear offset between the input and output magnitudes. The clusters recovered are dimmer by roughly a quarter of a magnitude. This could be due to the thousands of low-mass stars we just cannot observe in the near-UV. The outliers could be due to having small clusters inserted into noisy regions. However, it does appear that the radius is in fact generally overestimated, by up to a factor of 4 greater than the input radius (Figure 3.8).

Comparison to the clusters identified by-eye yield interesting results. While there are 386 objects that were in agreement between the three catalogs provided by three people identifying fake clusters by eye- these objects actually match up with 406 unique input fake clusters. This is due to some of the clusters identified by eye actually containing multiple clusters. In Figure 3.8, it appears that people overestimate the radius and cannot well resolve clusters that are too close together. The algorithm is able to distinguish close clusters as effective radii recovered by the algorithm are significantly smaller. Of the 39 false positives retrieved by the algorithm, 15 of the clusters were identified by both the algorithm and by-eye identification, affirming that some these clusters are more likely to be real cluster candidates.

3.4 Results

We present a catalog of 757 star cluster and association candidates in NGC 6946. Figure 3.9 shows examples of the postage stamps and color-magnitude diagrams (overplotted over

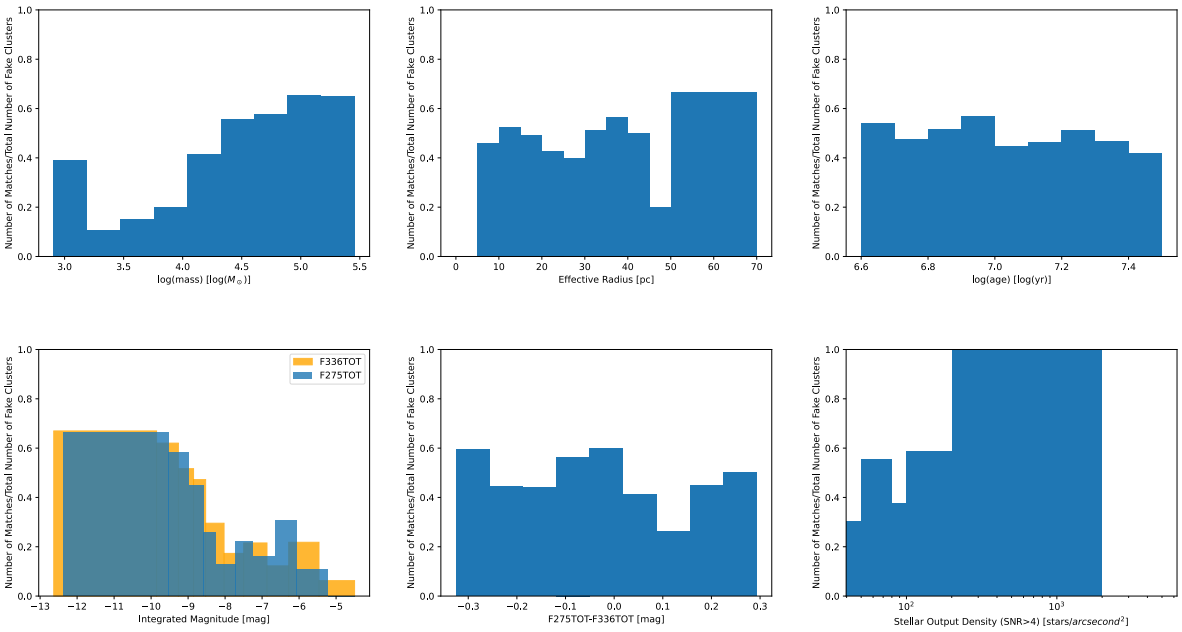

Figure 3.6 Top Left: The ratio of recovered to total fake clusters as a function of input mass. Due to the direct relationship between mass and luminosity, this ratio follows a similar pattern as the ratio as a function of integrated F275W and F336W magnitude plots. The more massive the cluster is, the more likely it is to be detected. Top Middle: The ratio of recovered to total fake clusters as a function of input effective radius. Top Left: The ratio of recovered to total fake clusters as a function of age. Bottom Left: The ratio of recovered to total fake clusters as a function of input integrated F275W and F336W magnitude. Unsurprisingly, the algorithm recovers clusters that are brighter in either filter - identifying more young massive stars within these clusters. Bottom Middle: The ratio of recovered to total fake clusters as a function of color. Bottom Right: The ratio of recovered to total fake clusters as a function of average stellar density within the cluster. The clusters that are most likely to be recovered are the clusters with the highest average stellar density. This is unsurprising - however the performance of this can likely be changed depending on the chosen thresholds in the algorithm

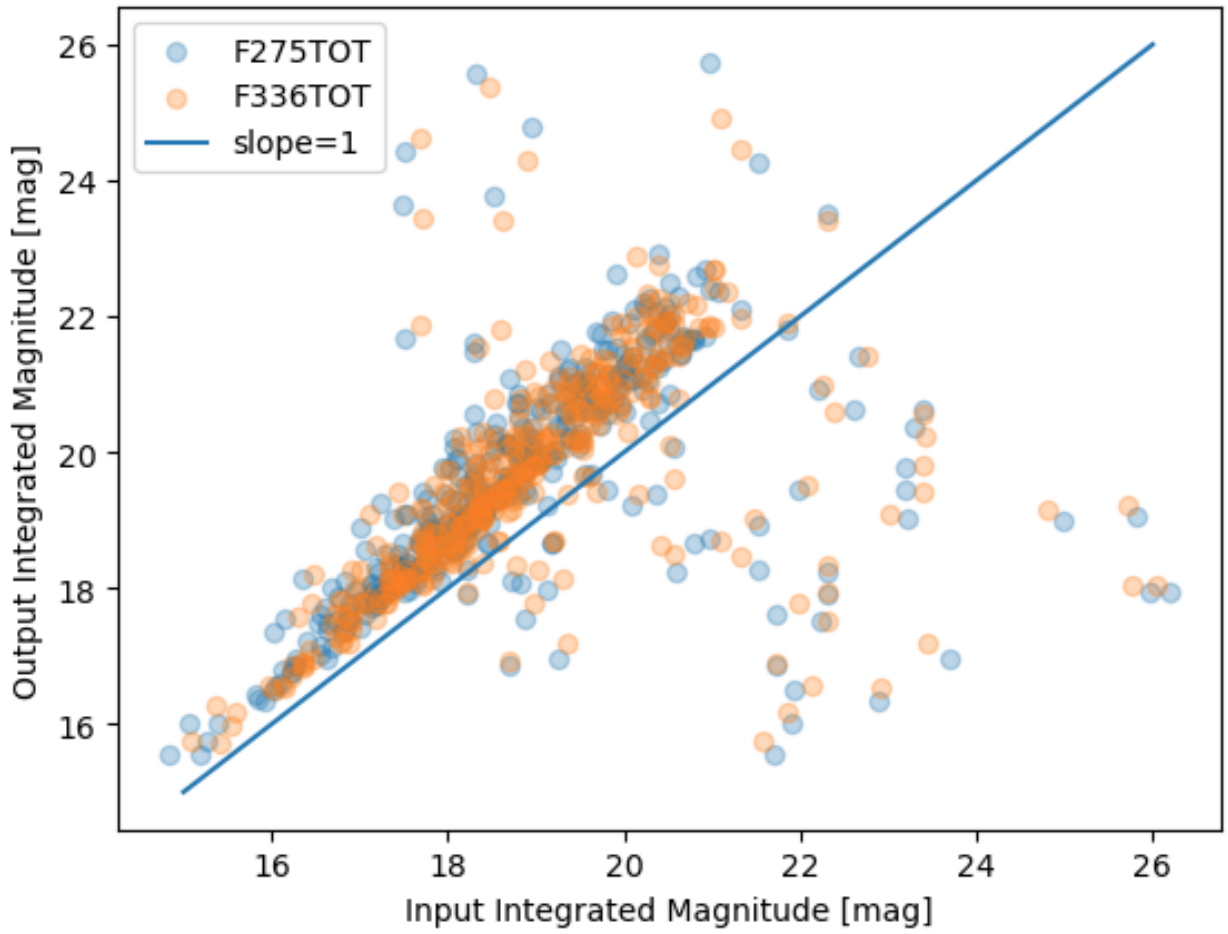

Figure 3.7 Input magnitude of each cluster versus its output magnitude in both F275W and F336W. The output magnitude is systematically offset by approximately quarter of a magnitude. This makes sense as the algorithm's contours do not fully encapsulate every star of the cluster. The outliers here are due to small clusters being inserted into areas of higher stellar density of the real stars.

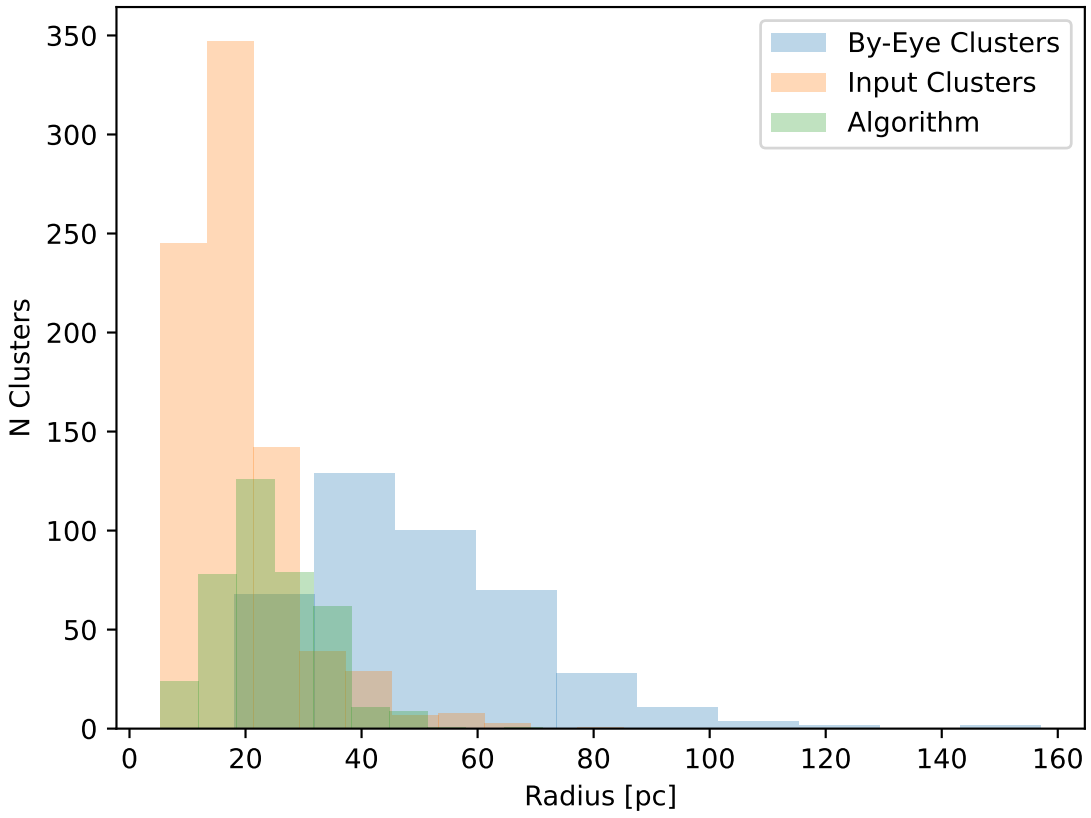

Figure 3.8 Histogram of the input radii versus the output radii recovered by the algorithm and by-eye identification.

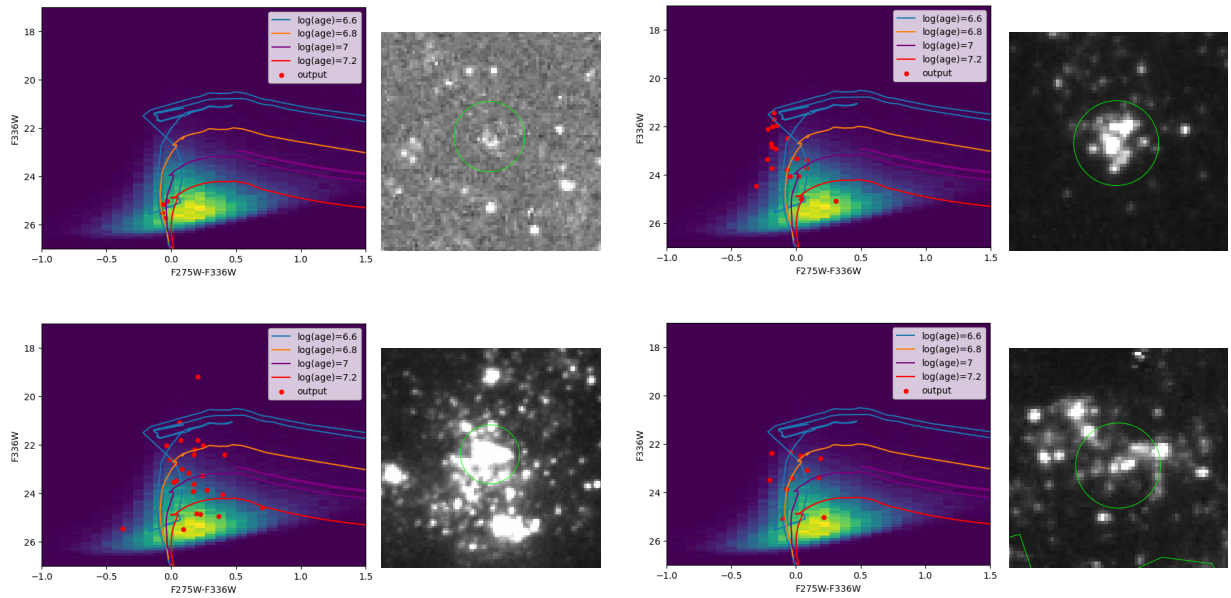

Figure 3.9 Color-magnitude diagrams (first and third columns from the right) and postage stamps (second and fourth columns from the right) of a selection of cluster or association candidates identified by the algorithm. Each CMD is plotted over a Hess diagram of all the high quality photometric sources from the FUVS catalog. Isochrones of log(age/yr) = 6.6, 6.8, 7, and 7.2 are overplotted on the CMDs to give context regarding the ages of these candidates. The red dots labeled "output" are the photometry of the sources identified to be within the cluster/association candidate. The candidates presented in the postage stamps provide an example of the diverse morphologies and integrated magnitudes. A half-arcsecond circle is added around the center of the cluster for scale.

a Hess diagram of all the high quality photometric sources in NGC 6946) of the high quality stars of four detected cluster/association candidates. A half arcsecond (18.9 pc) circle has been added to the images for scale. The locations of these clusters are superimposed on the F275W image of NGC 6946 in Figure 3.10.

Table 3.4 is a portion of the complete catalog available on MAST at doi: 10.17909/2rkn-xh93. The machine readable table will include the the vertices of the candidates detected by the algorithm in addition to the geometric centers, integrated photometry, radii, and color

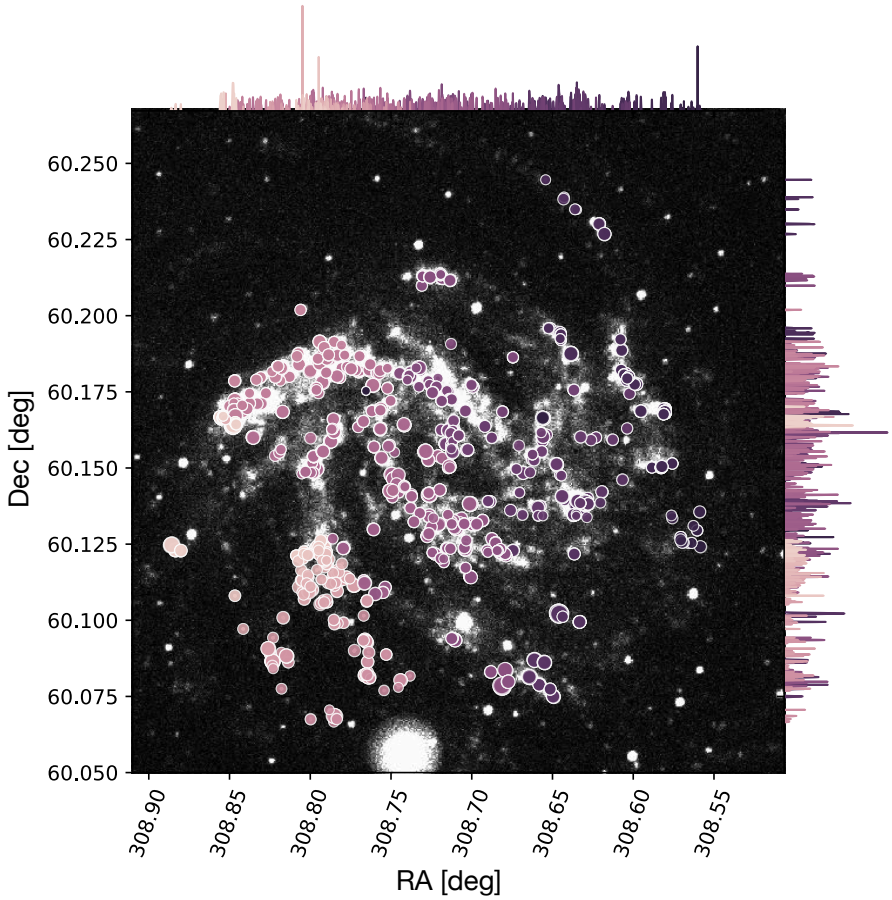

Figure 3.10 The spatial distribution of the cluster/association candidates detected overlaid on an F275W image of NGC 6946. A majority of these clusters are found in the spiral arms of NGC 6946. North is up and east is right.

Table 3.1. Summary of Cluster/Association Candidates in NGC 6946

Index	GeomCent RA [deg]	GeomCent Dec [deg]	IntPhot F275W [mag]	IntPhot F336W [mag]	Radius [parsecs]	F275W-F336W Color [mag]
0	308.847182	60.170139	20.64	20.43	19.8	0.2
1	308.855559	60.166659	18.10	17.87	32.6	0.2
2	308.853979	60.166999	20.75	20.62	12.4	0.1
3	308.853639	60.167010	18.76	18.69	26.7	0.07
4	308.855270	60.165963	17.97	17.89	23.8	0.08
5	308.846044	60.164662	22.04	21.88	9.8	0.2
6	308.854063	60.166430	19.56	19.41	21.5	0.2

Note. — This table is a sample of the first 7 clusters and associations identified by the algorithm. The geometric center coordinates are in decimal degrees. The radius is in parsecs. Color and integrated F275W and F336W magnitudes are in magnitudes. The remaining variables are unitless.

presented in the table below.

The radii of the detected cluster and association candidates had wide ranges from 3 to 76 pc with median radii of 22 pc (Figure 3.11, bottom right). The distribution is fairly continuous, making it challenging to distinguish which is a cluster and which is an association. The cluster candidates detected in Johnson et al. (2012) have radii ranging between 2-22 pc, assuming a distance of 785 kpc (McConnachie et al., 2005). The cluster and association candidates detected in Larson et al. (2023) range between 8-64 pc for NGC 3351 at 10 Mpc and NGC 1566 at 18 Mpc. With NGC 6946 at a distance of 7.8 Mpc, it makes sense to detect larger clusters, though it is likely a majority of these clusters have a smaller radius than estimated, given that the algorithm with our chosen thresholds returned output radii larger than the input radii for 73% of the detected fake clusters.

We present the integrated F275W, F336W, and color histograms of the detected cluster and association candidates (Figure 3.11, top row and bottom left). The median color of the clusters is roughly 0.24 mag. This reddening is likely due to the dust surrounding these younger clusters.

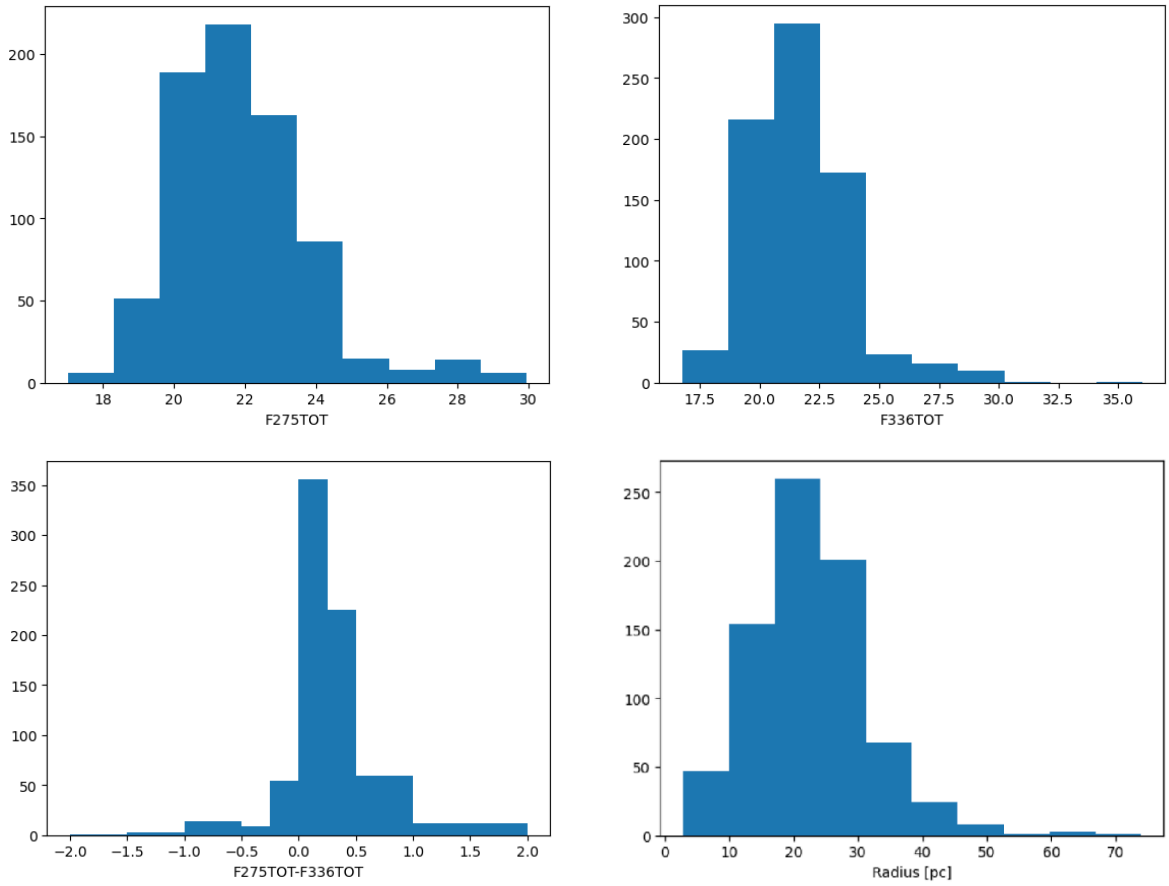

Figure 3.11 Top Left: Histogram of integrated F275W magnitude of the detected cluster and association candidates, with median magnitude of 19.84 mag. Top Right: Histogram of integrated F336W magnitude of the detected cluster and association candidates, with median magnitude of 19.5 mag. Bottom Left: Histogram of integrated F275W-F336W color of the detected cluster and association candidates, with median color of 0.24 mag. Bottom Right: Histogram of radius of the detected cluster and association candidates, with radii ranging between 3 to 76 pc. This plot has not been corrected for the bias towards estimating a larger radius.

3.5 Discussion

3.5.1 Inner vs Outer Disk Clusters

We examine the radii and integrated F275W and F336W magnitudes as a function of the galactocentric radii (Figures 3.12 and 3.13). There appears to be a significant amount of clusters detected around 6000-8000 pc from the galactic center with a wide range of integrated magnitudes. Upon further examination, we see in Figure 3.10, several groups of clusters are detected at different locations in the galaxy at those radii, which could point to the spread in cluster magnitudes in both filters at that radius, as one tip of the spiral arm has a region of intense formation while the others do not. The local environment containing the clusters has more of an impact on the effective radii of each clusters than the radius of the galaxy at which they are found. Still, while the spread is quite large, there seems to be a trend of smaller and dimmer cluster and association candidates as the distance from the center increases. As shown in Figures 3.12 and 3.13, we fit a line by minimizing the sum of the squared residuals of the least squares fit. This gives us a slope of $-3.3 \times 10^{-4}, 1.39 \times 10^{-4}$, and 1.52×10^{-4} for effective radius, integrated F275W magnitude, and integrated F336W magnitude versus distance in parsecs, respectively. This is consistent with results from Scheepmaker et al. (2007); Bastian et al. (2012); Yadav et al. (2021), where they find the clusters at the outer regions of the galaxy are more compact than those in the inner disk. In addition, previous resolved star formation history analysis done in Tran et al. (2023), show lower star formation rate surface densities in the outer disk of NGC 6946 by an order of two magnitudes. Bastian et al. (2012) attribute this difference to an underlying age-size relation, while Yadav et al. (2021) postulate that this is evidence the inner disk is a more favorable environment for star formation. We will further investigate a potential age-size relation in Tran et al., in prep.

3.5.2 SFR versus Brightest Clusters

We compare the number of clusters detected to the total star formation rate. In NGC 6946, we detect 757 cluster/association candidates less than 25 Myr old (see Tran et al. (2023))

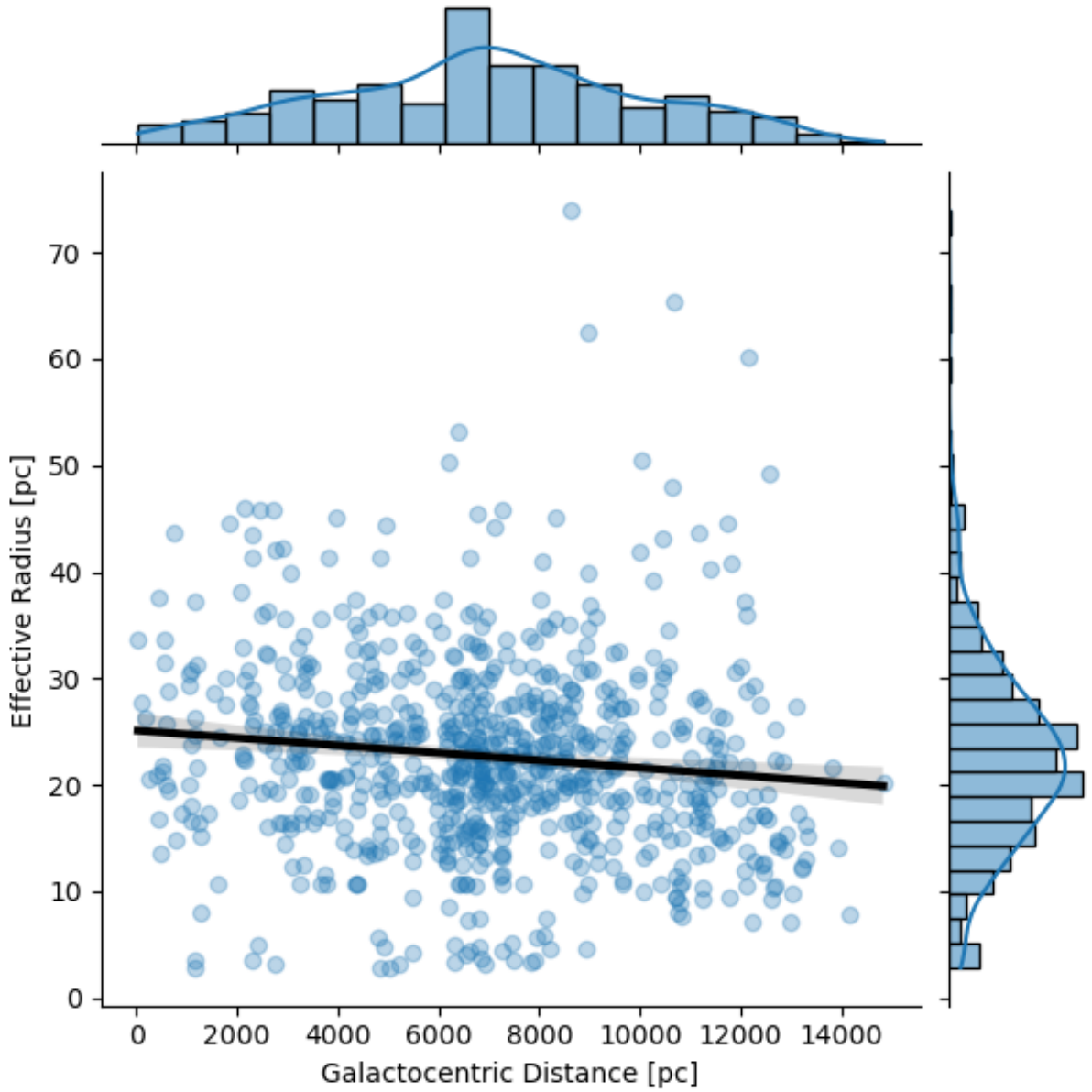

Figure 3.12 Radius of clusters as a function of their galactocentric radii. The black line is the corresponding linear regression model fit.

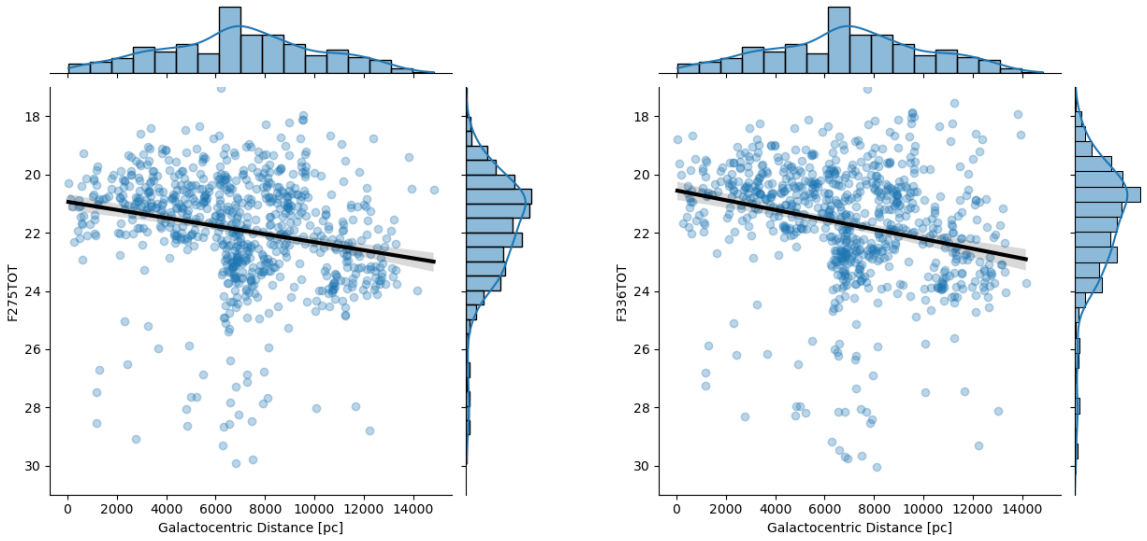

Figure 3.13 Integrated F275W and F336W magnitudes as a function of galactocentric distance for each cluster. The black line on each plot is the corresponding linear regression model fit.

on completeness of this dataset as a function of age) and a total star formation rate (SFR) of 13.16 $M_{\odot}$/yr (Tran et al., 2023) over the last 25 Myr. While Johnson et al. (2022) find 1214 star clusters in M33 with a total SFR of 0.32 $M_{\odot}$/yr over the past 100 Myr and 106 clusters with a total SFR of 0.2 $M_{\odot}$/yr over the past 10 Myr (Lazzarini et al., 2022). We are detecting a significantly smaller number of clusters despite the higher rate of star formation in NGC 6946. This is likely due to NGC 6946 being significantly farther away, limiting the size of clusters we can detect as well as the large amount of foreground extinction. We are also limited in the near UV to only observe the most massive young stars, which with any IMF distribution, there are significantly fewer in each cluster than the fainter, smaller stars. This is consistent with the completeness limits we derive from the fake clusters, where there are potentially more than half of the clusters that we are not able to detect. We quantify these limits by comparing the number of star clusters in the M33 catalog with masses greater than our 50% mass completeness limit ($\log(\text{mass}/M_{\odot})$=4.17) and younger than the ages we can detect (log(age/yr)=7.4), which gives us a ratio of number of clusters to SFR of 3 clusters to an SFR of $0.26 M_{\odot}/yr$ in the last 25 Myr, which is the same order of magnitude as that in NGC 6946.

3.5.3 Luminosity Function

We fit the cluster luminosity using the absolute magnitudes, using a distance of 7.8 Mpc (Anand et al., 2018; Murphy et al., 2018; Johnson et al., 2023), in F275W and F336W following Equation 3.1, converting the obtained slope β to the slope of the luminosity function (Equation 3.2) using Equation 3.3. We use variable bin sizes, with each bin containing the same number of clusters. The dimmer end of the luminosity distribution (faintward of F336W and F275W integrated absolute magnitude of -9) appears to have more scatter due to the completeness dropping below 50%. We attempted different bin sizes to minimize the scatter overall, however due to the poor completeness faintward of absolute magnitudes of -9, we only fit the luminosity function for magnitudes brighter than -9 in both F275W and F336W. The uncertainties are derived using the Poisson uncertainties from the number of clusters

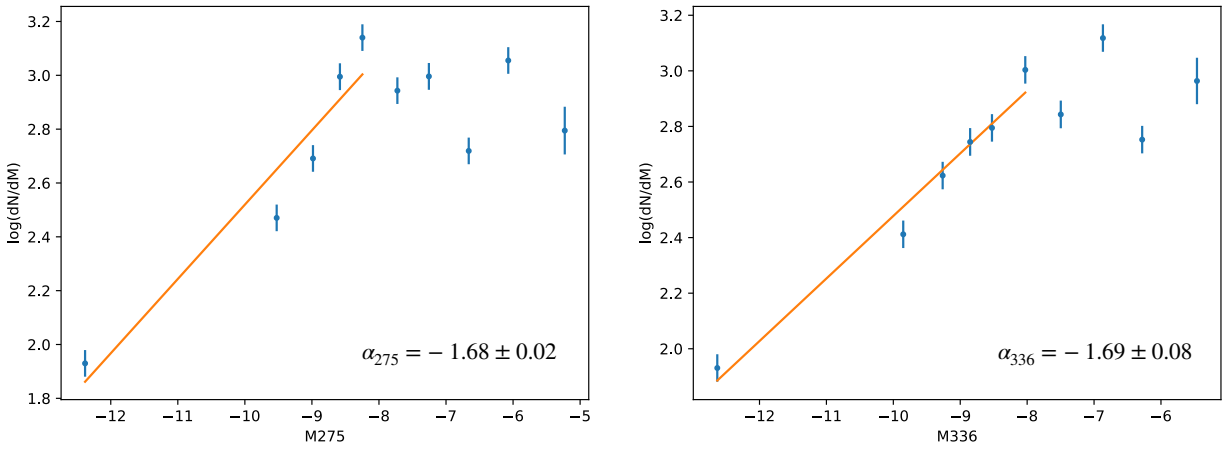

Figure 3.14 Cluster luminosity functions of NGC 6946 in F275W and F336W, fit using absolute magnitudes, then converted to α using Equation 3.3.

in each magnitude bin. These absolute magnitudes were corrected for completeness, using the values we find in Section 3.3.6. We derive a slope of $\alpha_{275} = 1.68 \pm 0.02$ for F275W and $\alpha_{336} = 1.69 \pm 0.08$ for F336W (Figure 3.14).

$$NdM = A10^{\beta M} dM \tag{3.1}$$

$$NdL \propto L^{-\alpha} dL \tag{3.2}$$

$$-\alpha = -2.5\beta - 1 \tag{3.3}$$

These results appear to be consistent with less steep luminosity functions derived for other galaxies in near UV filters, such as the LEGUS galaxies: $\alpha_{275} = 1.76 \pm 0.02$, $\alpha_{336} = 1.86 \pm 0.03$ (class 1 and 2), $\alpha_{275} = 1.74 \pm 0.04$, $\alpha_{336} = 1.89 \pm 0.04$ (class 3) (Adamo et al., 2017); NGC3610: $\alpha_{336} = 1.78 \pm 0.05$ or 1.9 ± 0.07 if corrected for observational scatter (Whitmore et al., 2002); M31: $\alpha_{336} = 1.65 - 1.73$ and $\alpha_{275} = 1.58 - 1.72$ (Johnson et al., 2012, 2015),

M83: $\alpha_{336} = 1.79 - 1.86$ (inner versus outer field, respectively) (Bastian et al., 2012). Gieles et al. (2006) fit the luminosity function of NGC 6946 with a Schechter function determining $\alpha_V = 1.7 \pm 0.05$ faintward of the break at $M_V = -8.9 \pm 0.04$, and $\alpha_V = 2.4 \pm 0.1$ brightward of the break. Others have determined a steeper slope in M51 and the Large and Small Magellanic Clouds of $\alpha = 2 - 2.4$ (Hunter et al., 2003; Whitmore et al., 2014; Messa et al., 2018).

3.6 Summary and Conclusions

- We utilize a modified computer vision algorithm to non-parametrically detect clusters as a function of their stellar density distributions. This allows us to not impose ideas of what clusters "should" look like, as many young clusters are not centrally-peaked like older globular clusters.

- This methodology performs on par with or slightly better than by-eye detection for at higher speeds. The cons of this methodology is that it requires careful selection thresholds and bandwidth parameters to ensure accurate stellar density maps down to cluster scales and to ensure cluster detection in crowded regions.

- We detect 757 cluster and association candidates in NGC 6946 with a 50% completeness down to $10^{4.17} M_\odot$, roughly 19 mag in F275W and F336W. We can only detect the brightest and largest young clusters and associations at this distance.

- We determine a slope of 1.68 ± 0.07 and 1.69 ± 0.02 for the cluster luminosity functions in F275W and F336W, respectively.

- We find trend towards dimmer and smaller cluster candidates as a function of galactocentric radius.

- This algorithm and cluster/association dataset will be made available for public use.

The following chapter will constrain the mass and age functions of the presented clusters and associations in NGC 6946, providing observational constraints on cluster formation on galactic scales and spiral arm formation in disk galaxies. In terms of future work with the algorithm, we will be improving the non-maximum suppression algorithm, where it makes the retrieved contours boxy looking.

Chapter 4

AGES AND MASSES OF CLUSTER AND ASSOCIATION CANDIDATES IN THE FIREWORKS GALAXY

In this chapter, I build on the work done in the previous chapter by measuring the cluster mass and age functions of the 470 cluster and association candidates in NGC 6946. The bulk of this work will be submitted for peer-reviewed publication.

4.1 Introduction

Stellar clusters tell us a lot of information about star formation on galactic scales (Kruijssen et al., 2019; Massari et al., 2019) and on individual cluster scales (Grudić et al., 2021). Studying large, complete datasets of clusters, can tell us generally about what fraction of stars form in clusters, what kinds of stars form in clusters, and how long it takes for stars in cluster to disperse and populate the field. With a large enough sample, we can further study how clusters change as a function of their environment, particularly when there are complimentary datasets measuring the molecular gas in the surrounding environment. We can examine whether certain temperatures, gas densities, molecular cloud mass, etc. are more conducive to forming more massive clusters, how close these stars can be to one another to continue star formation, how long-lived clusters are, stellar multiplicity, and more.

Two benchmarks used to study these areas of star formation are the cluster mass function (CMF) and the cluster age function. Many have measured the slope of the age function to understand the timescales on which clusters last (Fall et al., 2005; Gieles, 2009; Chandar et al., 2010; Silva-Villa et al., 2014; Messa et al., 2018). Others have extensively characterized the CMF to understand the properties of the natal clouds from which these clusters formed, whether star formation happens in a hierarchical manner (Elmegreen et al. (2006); Elmegreen

(2010), and references therein). Generally the mass function is well fit by a single power law with a slope of 2 (de Grijs & Anders, 2006; Chandar et al., 2010; Whitmore et al., 2010; Fouesneau et al., 2014), which is consistent with hierarchical star formation. However, as more cluster data is gathered, there have been significant differences in their measured slopes, if a single power law is assumed, as well as large discussions on whether a Schecter function is a better fit to these distributions particularly at the high-mass end. Some attribute the high-mass cutoff observed to incomplete sample sizes (Chandar et al., 2010; Whitmore et al., 2010), while others believe this high mass truncation exists (Bastian, 2008; Gieles, 2009; Larsen, 2009; Bastian et al., 2012; Konstantopoulos et al., 2013; Adamo et al., 2015; Wainer et al., 2022). The complex selection effects due to the way these clusters are detected and incomplete samples, makes it challenging to compare measurements in between catalogs and in between different galaxies.

NGC 6946 is a nearby (7.8 Mpc Murphy et al. (2018)), nearly face-on galaxy with at least 757 cluster candidates (Tran et al. submitted) with a high rate of recent star formation and a near-UV photometric catalog. With the combination of both cluster candidate and photometric catalogs, we can measure the cluster age and mass functions using the photometry of the stars within the clusters.

This chapter is structured as follows. In Section 4.2, we discuss the NUV HST observations and selection of sources and clusters used. In Section 4.3, we discuss the artificial star tests we performed to measure the completeness of our sample. In Section 4.4, we present the methods for obtaining the age and mass of each cluster. In Section 2.3, we present masses and ages of each cluster. In Section 4.7, we discuss the spatial distribution of ages and masses of the clusters, their age and mass functions, the relationship between radius and age, the relationship between mass, age, and the galactocentric radius, and cluster formation efficiency. We compare these results with those measured in different galaxies.

4.2 Observations and Source Selection

For this work, we combine two catalogs: 1. a catalog of resolved NUV photometry of stars in NGC 6946 in Hubble Space Telescope (HST) Wide Field Camera 3 (WFC3) ultraviolet and visible light channel in filters F275W and F336W (The Fireworks UltraViolet Survey Cluster Candidate Catalog (FUVS-CCC) 10.17909/2rkn-xh93)and 2. a catalog of clusters and association candidates in NGC 6946 identified using a computer vision-based algorithm and the first catalog (The Fireworks UltraViolet Survey Catalog 10.17909/gveq-8820). For more details on the observations (GO-15877; PI Levesque et al. (2019)), source detection, and resulting photometry associated with the first catalog, see Tran et al. (2023). For details on the methods used to identify the candidates used in this paper, please see our companion paper, Tran et. al in prep.

We identify all high quality photometric sources from FUVS found within the cluster and association candidate vertices from the Fireworks UltraViolet Survey - Cluster Candidate Catalog (FUVS-CCC). We then select clusters with at least 3 high quality sources with sharpness^2 < 0.2; crowding < 0.7; signal-to-noise ratio (SNR) > 4 in both F275W and F336W; and F275W-F336W color $>$ -1.3, which have the high quality flag (QF1) in FUVS. Because one of the primary sources of uncertainty in our methods is the number of stars used in each fit, we want at least 3 sources to decrease the uncertainty. This leaves us with 470 cluster and association candidates, each with 3 to 77 high quality photometric sources that we use in this paper.

4.3 Artificial Star Tests

We perform artificial star tests (ASTs) for two reasons. Our catalog of cluster and association candidates is very young (less than 25 Myr (Tran et al., 2023)), with a majority of the candidates having a non-centrally concentrated stellar distribution. Because where the stars are located in each candidate is unique, we must understand how the stellar density impacts the F275W and F336W completeness of each candidate. First, the ASTs allow us to measure

the photometric completeness limits of each individual cluster, as the completeness is highly density-dependent (Lazzarini et al., 2022; Tran et al., 2023). Second, the number of stars in each cluster/association is relatively small, we convolve the artificial stars with the real data in our fitting process in Section 4.4.

Custom artificial star tests were performed for each cluster. For each cluster, we generate 50,000 artificial stars, randomly sampling the CMD, with a F275W-F336W color range of -0.5 to 1.0 mag, and a F275 magnitude 1 mag dimmer than the dimmest detected star and the 0.3 mag brighter than the brightest star to properly test the completeness limit of the stellar photometry in each cluster and to capture all the blends.

4.4 Measurement of Ages and Masses

We used the CMD-fitting code, MATCH (Dolphin, 2002), to measure the ages of each cluster by fitting a single stellar population to each cluster/association candidate, assuming the stars have the same age and metallicity. For each cluster, MATCH creates Hess-diagrams or binned CMDs of stars within the cluster, as well as Hess-diagrams for the background population of stars. MATCH then takes user-defined ranges in age, metallicity, distance, extinction, IMF, and binary fraction to create individual synthetic CMDs for each possible combination of parameters. The individual CMDs generated from given parameters are linearly combined to form composite CMDs, which are compared to the observed CMDs with the background population CMD subtracted out. The best-fit composite synthetic CMDs are then used to infer the age of each cluster.

We assume a Kroupa IMF (Kroupa, 2001), binary fraction of 0.35, and the Padova stellar evolutionary models (Marigo et al., 2008; Girardi et al., 2010). We fix the distance of 7.83 $\pm$ 0.29 Mpc to be consistent with Murphy et al. (2018); Tran et al. (2023), who used the same CMD-fitting technique. We fit the metalliciities to be between log(Z)= -0.4 to 0.1. Following the age constraints detailed in Tran et al. (2023), we fit ages between log(age)=6.6 and log(age)=7.4. We utilize the best fit values of foreground extinction (A_V) and differential, or circumstellar, extinction (dA_V) from the extinction maps in Tran et al. (2023) to constrain

the range of A_V for each cluster. We first fit the foreground extinction from a range of 0.8 to the best fit A_V+dA_V for each cluster, assuming no differential extinction as the cluster sizes are small, using a coarse grid of A_V. Finding the highest likelihood value of A_V, we then redo the same age calculations over a finer grid of values in 0.05 increments to find the best fit A_V, described in detail in Lewis et al. (2015). The background population of each cluster is characterized by the stars within an annulus with an outer radius 10 times the measured effective radius and an inner radius 2 times the effective radius taken from FUVS-CCC.

We create marginalized distributions of extinction, age, and metallicity. We obtain the best fit masses for each cluster by multiplying the best fit age with the associated star formation rate (SFR) measured of each bin and propagate the age and SFR uncertainties to get the mass uncertainties.

4.5 Completeness and Reliability

We check the completeness as a function of mass and age. We verify the age and mass recovered as the concern is that match is estimating the clusters to be younger than they are because they are too dense and the crowding boosts the brightness of the fake stars. Figure 4.1 shows the completeness as a function of mass and age. As the age of the cluster increases, the mass required for over 50% completeness increases. Below the 50% completeness line, the completeness drops off significantly.

We verify the ages recovered by running MATCH on the fake clusters detected by the algorithm (see the previous chapter for details). We find the uncertainty of the ages recovered to be 5% (Figure 4.2).

4.6 Results

We present the measured ages and masses of each cluster/association candidate in Table 4.6 below. Some numbers in this table have been rounded to save space, but the full machine readable table for all 470 cluster and association candidates contain the measurements with full precision along with the vertices, effective radius, and F275W and F336W magnitudes

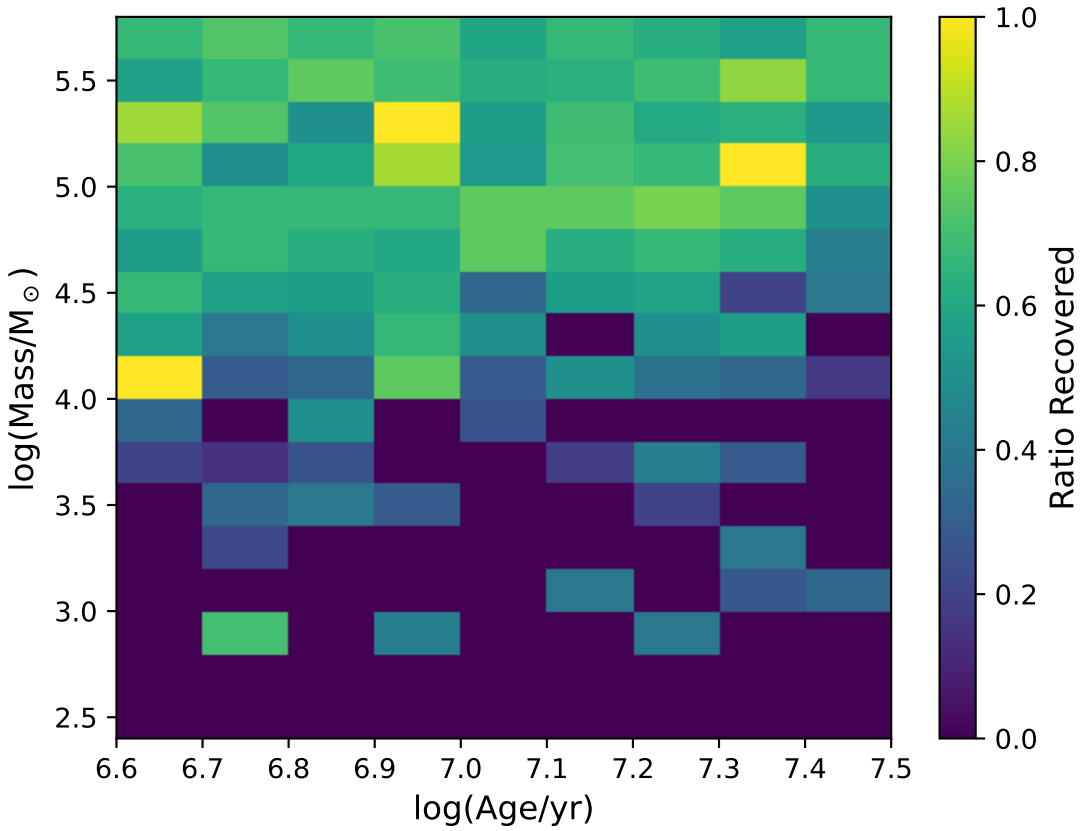

Figure 4.1 Completeness as a function of log(age) and log(mass), in bins of 0.1 and 0.2 dex respectively. As the age of the cluster increases, the mass required for over 50% completeness increases.

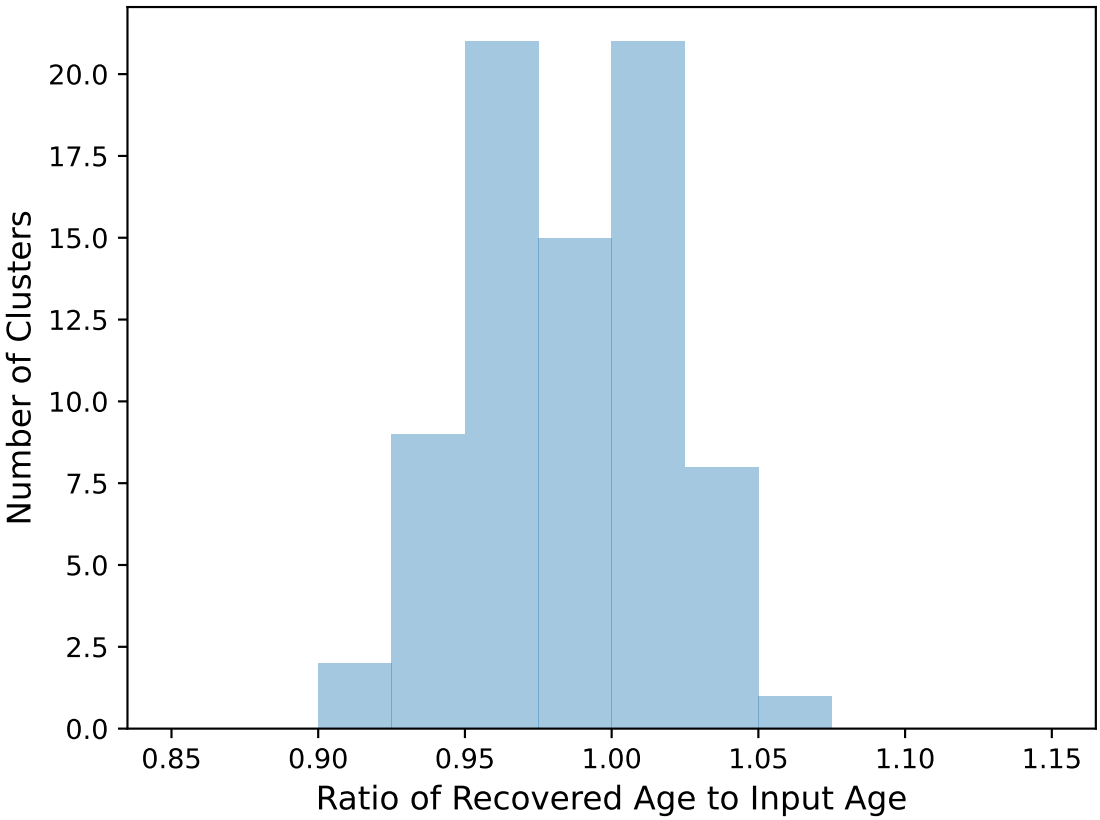

Figure 4.2 The ages recovered are roughly 0.95-1.05 of the input ages in log(age), showing that the uncertainty of the ages recovered with MATCH are within 5%.

Table 4.1. Summary of Cluster/Association Candidates in NGC 6946

Index	GeomCent RA [deg]	GeomCent Dec [deg]	Mass [log($M_\odot$)]	log(Age) [log(yr)]	N stars
0	308.847182	60.170139	$4.11^{+0.24}_{-0.26}$	$6.69^{+0}_{-6.69}$	11
23	308.855559	60.166659	$4.07^{+0.33}_{-0.17}$	$6.66^{+0}_{-6.66}$	26
98	308.853979	60.166999	$3.58^{+0.47}_{-0.23}$	$6.77^{+0}_{-6.77}$	5
109	308.853639	60.167010	$4.33^{+0.32}_{-0.18}$	$6.67^{+0}_{-6.67}$	21
151	308.846044	60.164663	$3.56^{+0.24}_{-0.26}$	$6.71^{+0}_{-6.71}$	13
155	308.854063	60.166430	$3.88^{+0.22}_{-0.28}$	$6.82^{+0.33}_{-0.27}$	3
187	308.846963	60.164339	$0^{+4.45}_{-2.65}$	$6.92^{+0}_{-0.6.92}$	13

Note. — This table is a sample of the first 7 rows of the clusters and associations identified by the algorithm. The geometric center coordinates are in decimal degrees. The mass is in log($M_\odot$) and age in log(yr). Many of the measured ages are upper limits as there were too few stars within the cluster to fit.

obtained in Tran et al. submitted. Some of the clusters had very few stars above the detection limit within them, and we were only able to place lower/upper limits on their ages and masses.

Figure 4.3 shows the age distribution for the cluster and association candidates in NGC 6946. The ages of the clusters peak at the youngest age bin of log(age)=0-6.7 and monotonically declines as a function of age. We present the distributions of the completeness-corrected ages, non-corrected ages, and the ages obtained by summing the individual age probability distribution functions (PDFs) of each cluster (see Appendix A). There appears to be a large number of young clusters we have not observed (likely the low-mass clusters). For all distributions, there appears to be a drop off in number of clusters after log(age/yr)=7.

Chandar et al. (2010) find that the clusters in M83 were disrupted quickly, with 80-90% disrupted each decade in age over time for clusters younger than 400 Myr. Messa et al. (2018), Silva-Villa et al. (2014), Chandar et al. (2006), and Whitmore et al. (2007) find a similar decline in number of clusters as a function of age in M51, M83, the Small Magellanic

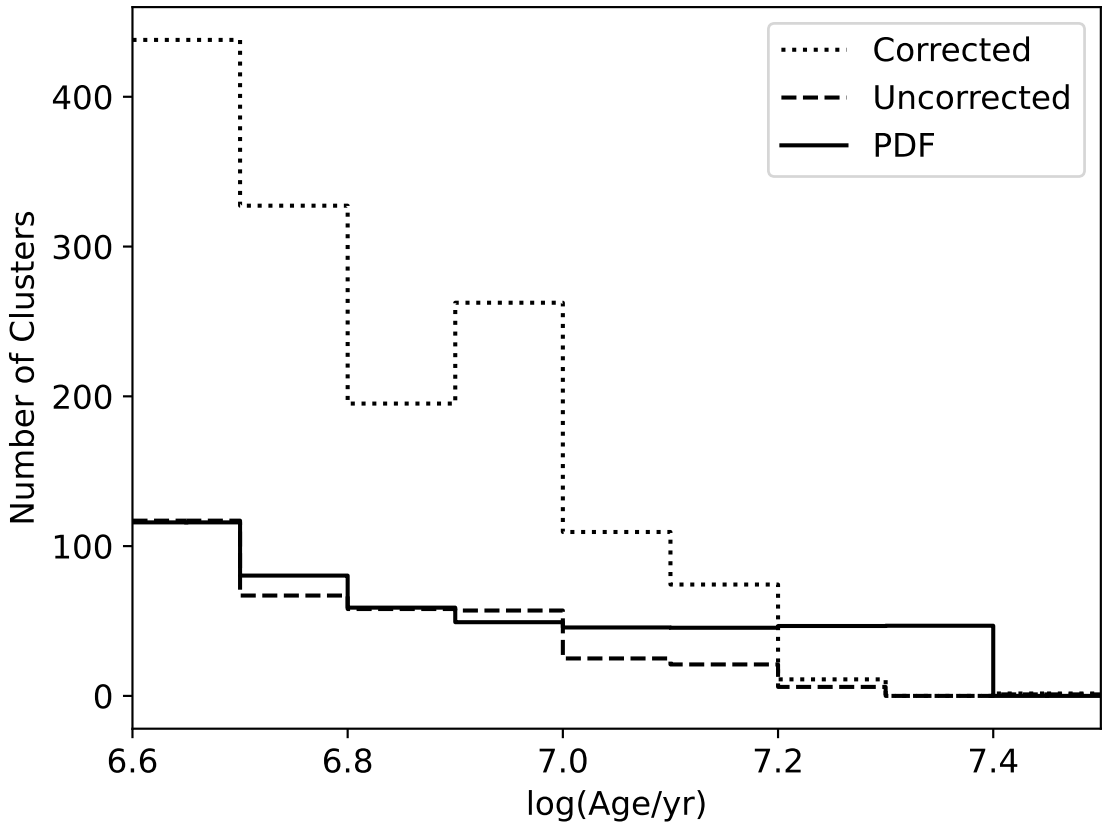

Figure 4.3 The distribution of measured ages of clusters. The dotted line shows the completeness-corrected age distribution, where we are potentially missing many young clusters. The age distribution not corrected for completeness (dashed line) and that calculated via summing the age PDFs of individual clusters (solid line) are roughly consistent with one another. Each of these functions shows a drop in number of clusters detected after log(age/yr)=7.0.

Cloud, and the Antennae Galaxies, respectively for a wide variety of age and mass ranges and cluster environments. Fall et al. (2005) similarly find that clusters in NGC 4038/9 (the Antennae Galaxies) have a steep decline over time. They interpret a young median age of log(age) = 7.0 as evidence for rapid disruption for young clusters, and that most young clusters are not gravitationally-bound and disrupted near the times they were formed. They propose that this disruption is due to the energy and momentum input from young stars to the interstellar medium of the protoclusters. We similarly find a decline in number of clusters with each subsequent decade. However, unlike previous studies, we observe a plateau in the age distribution obtained via summing individual PDFs after 10 Myr. Miholics et al. (2017) finds that the age distribution depends on the density and velocity distribution of the local ISM. Due to the limited age range we are able to measure reliably in the near-UV, we do not fit an age function to the clusters, unlike previous studies. Future work on longer-lived clusters will be done to accurately fit an age function and measure the impacts of two-body relaxation and the mortality rate of clusters in NGC 6946.

Figure 4.4 show the spatial distribution of ages of the clusters. The youngest clusters are found within the spiral arms of NGC 6946, with a high concentration of the clusters found in the tip of the northeast spiral arm and the Hodge Complex. This is consistent with the finding of an increased star formation rate in the past 5 million years (see Section 4.7.3 for further discussion).

Figure 4.5 shows the distribution of masses of clusters - the completeness-corrected masses, non-corrected masses, and the mass obtained by summing the individual mass probability distribution functions (PDFs) of each cluster (see Appendix A). A majority of the clusters line within the $\log(M/M_{\odot})$=3.5-4.5 range, with the completeness-corrected mass distribution showing a large number of low-mass clusters missing from our sample. However, these low-mass clusters (clusters with masses below $\log(\text{mass}/M_{\odot}) \leq 4$, are below our measured 50% completeness limit, so these measurements are far more uncertain.

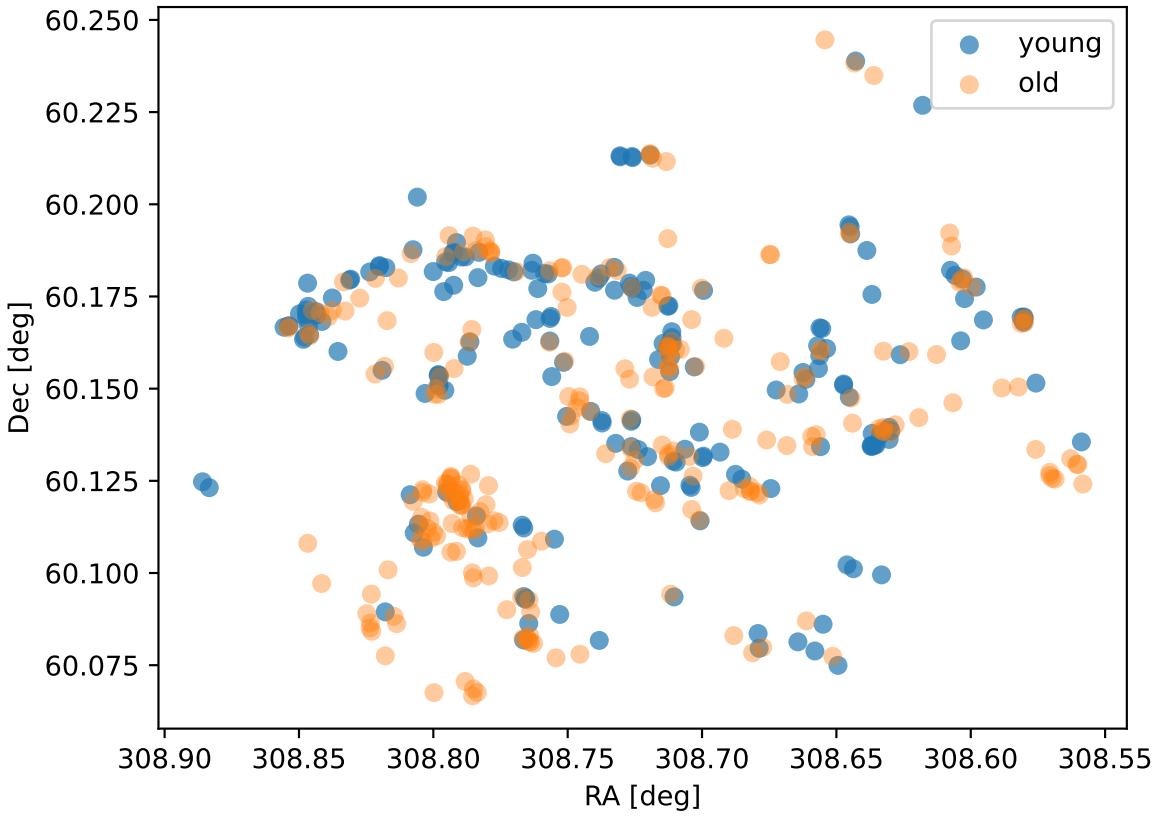

Figure 4.4 Locations of the young, log(age)¡6.8, clusters in NGC 6946. A majority of these clusters are within the spiral arms

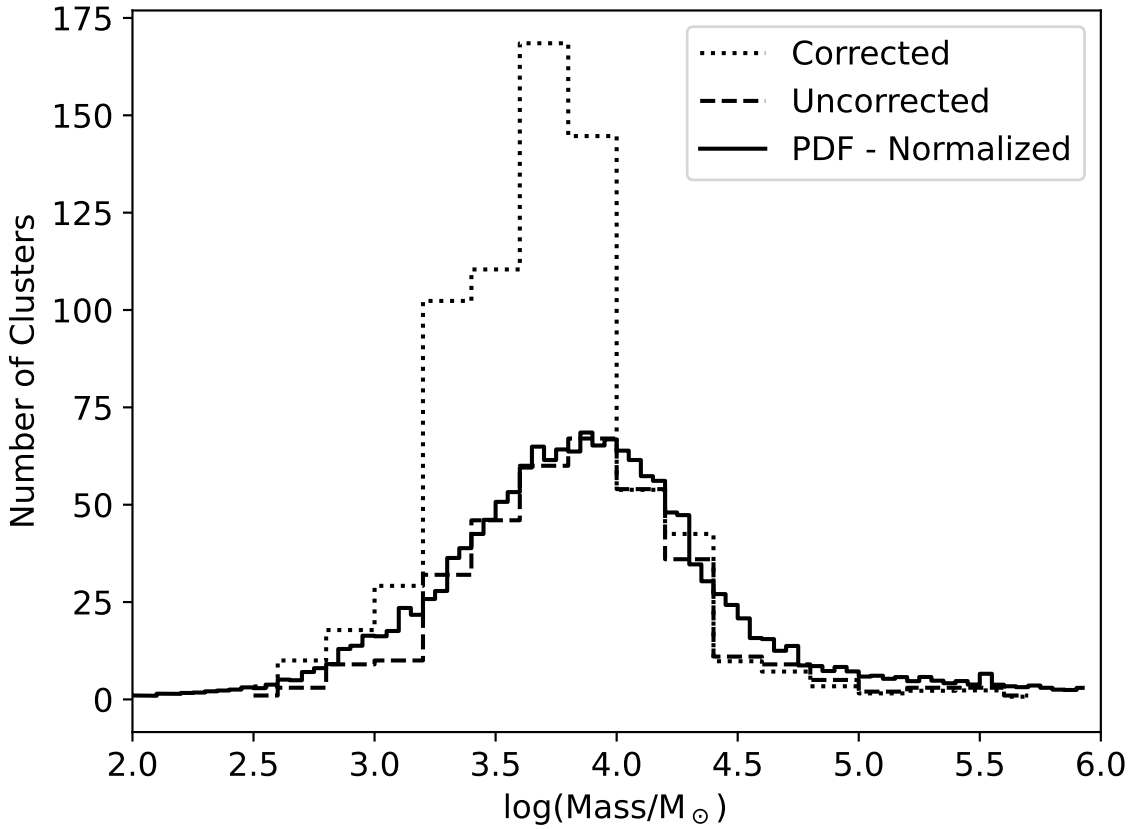

Figure 4.5 The distribution of measured masses of clusters. The dotted line is the mass distribution corrected for completeness, the dashed line is that not corrected for completeness. The solid line is calculated using the total of individual PDFs and normalized for the bin size easy comparison between distributions. Generally, there is a peak in the distribution between log(mass/M⊙)=3.5-4.5. The completeness-corrected distribution has an asymmetry, where there are more low-mass clusters. However, due to clusters of masses below 10,000 $M_\odot$ being below our 50% completeness limit, we gray out the the mass distribution below that, as the completeness correction makes this range of masses uncertain.

4.7 Discussion

4.7.1 Age vs. Mass

In Figure 4.6, we see that the older clusters tend to be more massive. This is in line with the idea that clusters with more mass are able to stay gravitationally bound for longer periods of time, and suggests lower mass clusters dissociate on a short (roughly 10 Myr) timescale. . After 10 Myr, the most massive clusters increase by an order of 1-2 magnitudes. This result in addition to the global star formation history as measured in Tran et al. (2023) (Figure 4.7) is consistent with the known positive correlation between the most massive cluster in a galaxy and its star formation rate Weidner & Kroupa (2006). They postulate that this is due to star clusters forming with massive stars being consecutively formed until feedback halts star formation. This results becomes more interesting as we see the number of clusters decrease while the star formation rate increases over lookback time (Figure 4.8). Even though the SFR is lower for the past 10 Myr, the number of clusters is high, then drops between the 10-25 Myr, even though the SFR rate was higher. Throughout the recent history of NGC 6946, as the star formation slows, the number of clusters formed decreases along with the formation of the massive clusters. The most recently formed clusters have at least an order of magnitude smaller masses.

4.7.2 Cluster Mass Function

We use linear least-squares to fit a single power law (Equation 4.1) to the mass distribution of NGC 6946, obtaining a slope of 1.83 $\pm$ 0.04 for masses greater than 10,000 $M_{\odot}$. This is a shallower slope than that obtained for other single power law fits, roughly between 2-2.3 (de Grijs & Anders, 2006; Chandar et al., 2010; Whitmore et al., 2010; Baumgardt et al., 2013; Konstantopoulos et al., 2013; Messa et al., 2018). Because there remains much debate between whether a single power law or a Schechter function is a better fit, we will be running Markov-Chain Monte Carlo simulations fitting the Schechter function and single power law to the distribution of masses above our 50% completeness limit of $10^4 M_{\odot}$. The bulk of this work

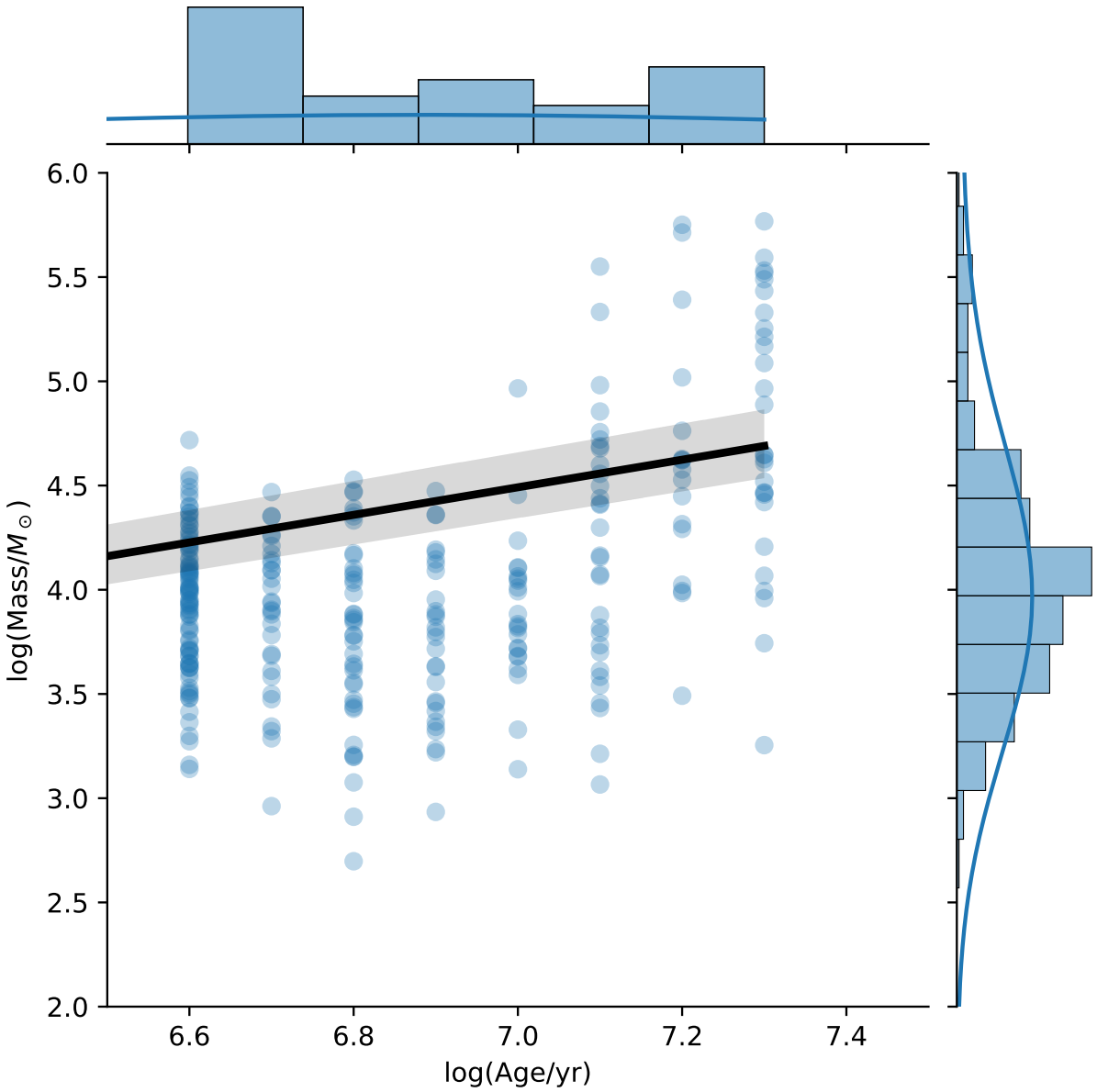

Figure 4.6 The distribution of masses versus ages of each cluster in NGC 6946. There appears to be a positive correlation between age and mass. This is likely due to more massive clusters being able to live longer.

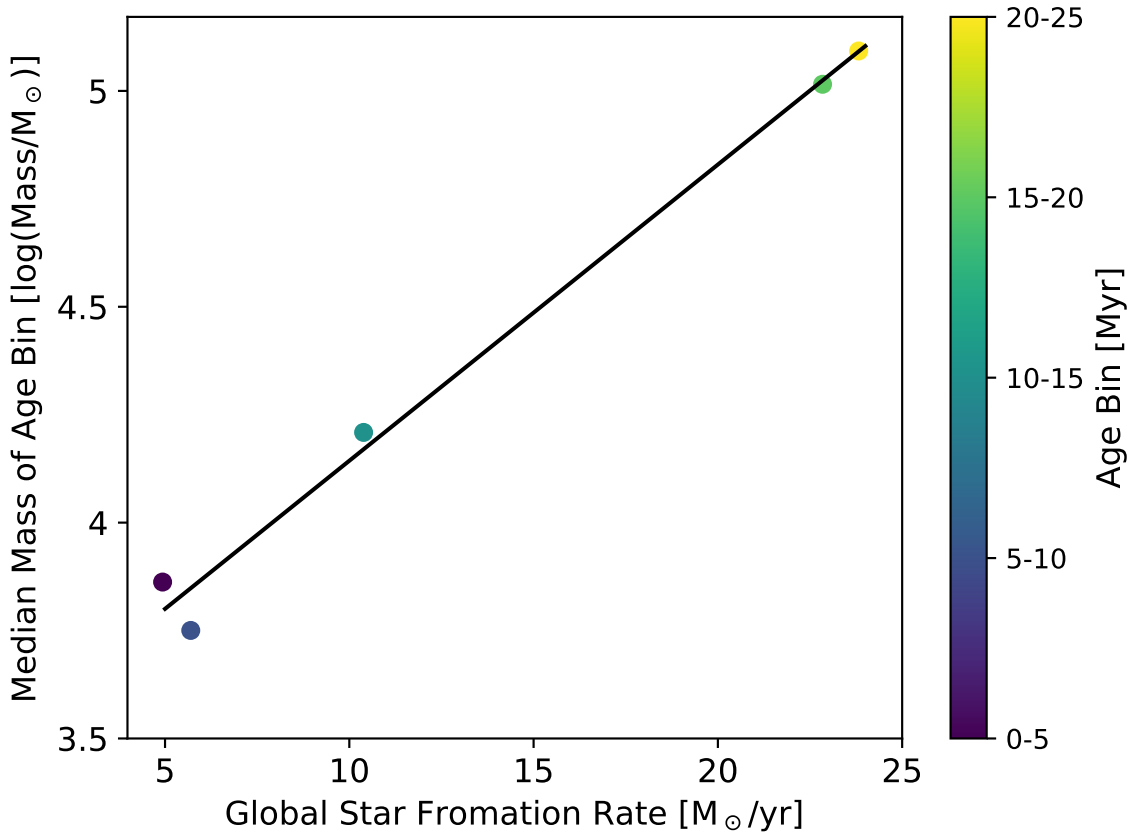

Figure 4.7 The median mass of clusters within each age bin as a function the global star formation rate at each age bin, color-coded by the age bin in linear time [Myr]. A line of best fit (solid black line) is added to help guide the eye.

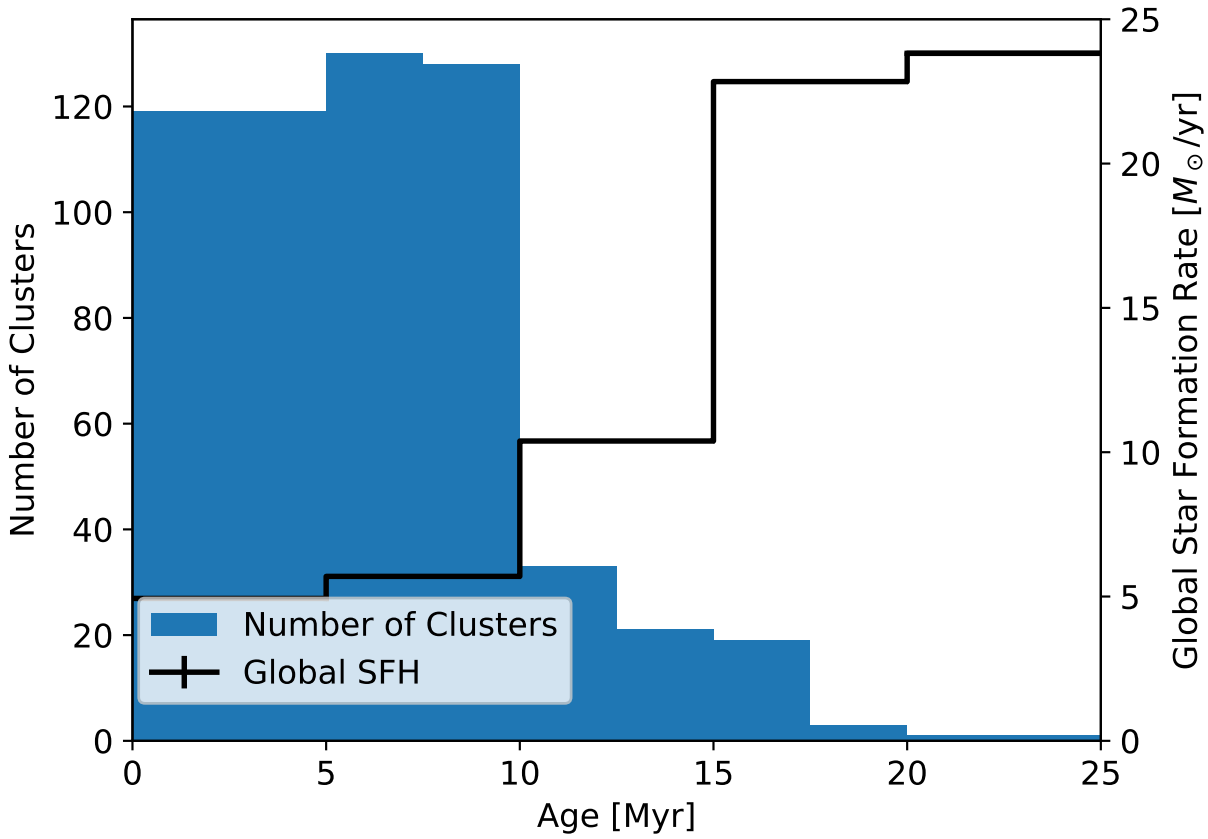

Figure 4.8 The measured age distribution of clusters in NGC 6946 relative to NGC 6946's global star formation history as a function of linear lookback time from 0-25 Myr. When the number of clusters and global SFR are compared with linear age bins, it becomes apparent that the drop in number of clusters is drastic after 10 Myr while the SFR increases after 10 Myr.

along with the additional mass fits will be presented in future peer-reviewed publication.

$$\frac{dN}{dM} \propto M^{-\alpha}, \alpha = ? \tag{4.1}$$

4.7.3 Cluster Formation Efficiency

Cluster formation efficiency (CFE, Γ) is fraction of star formation happening within bound clusters. Using Equation 4.2, we find that the overall CFE of NGC 6946 for clusters younger than 25 Myr, is 4.00 $\pm$ 2.3% for clusters with masses between log(mass/$M_\odot$)=2.5-6.0. We find a Γ of 4.00 $\pm$ 0.9 % for clusters younger than 5 Myr. The uncertainty in Γ is derived from the uncertainty in age, as MATCH has been used to measure both the star formation rate in each time bin (Tran et al., 2023) and the ages of each cluster, which has a measured uncertainty of 5%. The cluster formation efficiency is correlated with the star formation rate surface density, where an increase in star formation rate increases the fraction of stars forming in clusters.

Messa et al. (2018) find in M51 $\Gamma_{10-100Myr} = 18.6 \pm 2.4$, with a positive correlation with the galaxy's total star formation rate. Fall et al. (2005) find at least 20% and possibly all stars form in clusters and/or associations, including those that are unbound and short-lived. Johnson et al. (2016) find Γ = 4-8% for M31. Cook et al. (2023) finds a similarly low Γ = 3-5%. See Figure 4.9 for comparison to the model presented in Kruijssen (2012) and previous observations listed in Johnson et al. (2016). As shown in the Section 2.3, we observe a higher concentration of young clusters in areas with higher star formation rate surface density, particularly the Hodge Complex and the northeast tip of the spiral arm in NGC 6946 (Tran et al., 2023), showing consistency in the $\log(\Sigma_{SFR}) - \Gamma$ model presented in Kruijssen (2012) on both large and small scales.

$$\Gamma = \frac{M_{cl}}{M_{tot}} = \frac{M_{cl,tot}}{M_{tot}} \tag{4.2}$$

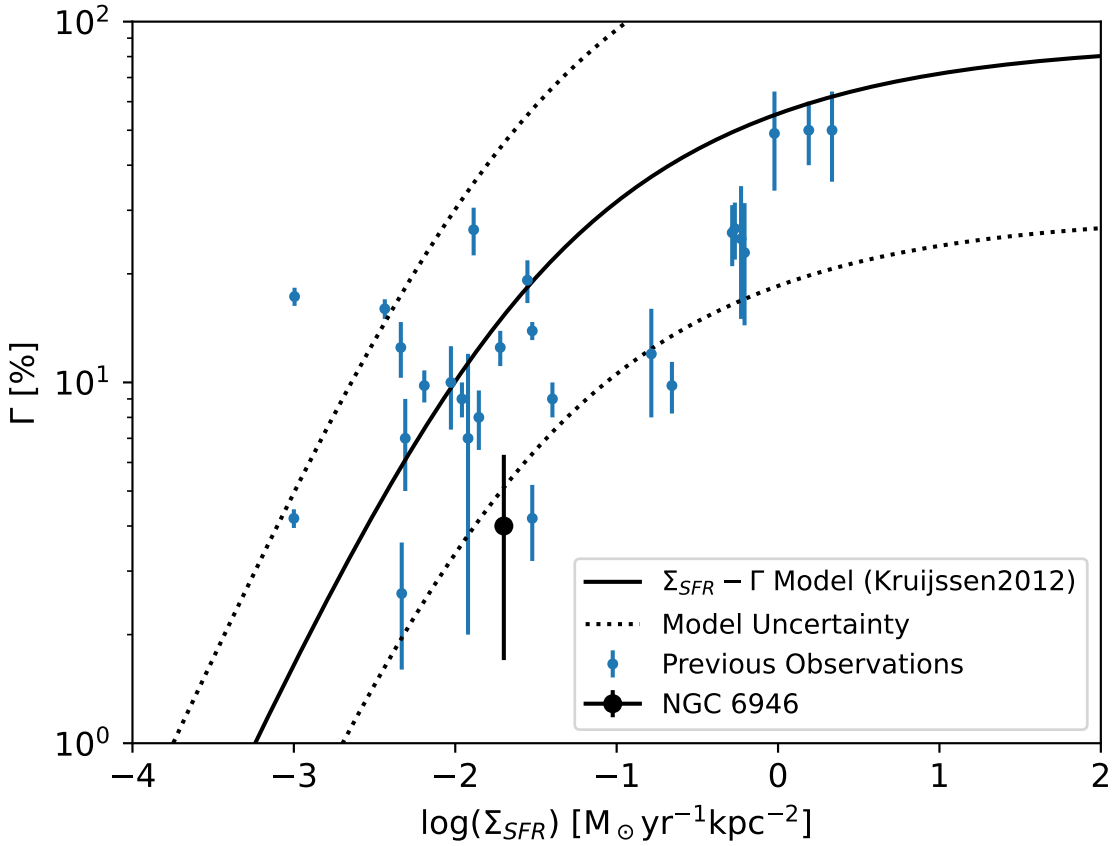

Figure 4.9 The cluster formation efficiency as a function of the star formation rate surface density. The model in the solid line is from Kruijssen (2012). The dotted lines are the uncertainties associated with the measurement of Γ, which can be uncertain to factors of 2-3 due to assumptions in their derivation. See Goddard et al. (2010a) for further discussion.

4.7.4 Age vs. Radius

Many have measured the median ages of star clusters as a function of spatial scale. Mackey & Gilmore (2003); Bastian (2008); Bastian et al. (2012); Larson et al. (2023) find the median ages of the population increase as spatial scale increases. (Bastian et al., 2012) postulate that this could be a physical effect, due to internal heating by stellar mass black holes, hard binaries and stellar evolution (e.g. Merritt et al. 2004; Mackey et al. 2007, 2008; Gieles et al. 2010a), or gas expulsion (Goodwin & Bastian 2006), or a combination of the above effects. Alternatively, it could be a selection effect due to the assumption of a single profile to fit all clusters, that is, ignoring mass segregation or the evolution of the profile shape (e.g. Gaburov & Gieles 2008), or a stochastic effect with the profile of the younger clusters being dominated by a few very bright stars, which tends to result in smaller derived radii than the true value (Silva-Villa & Larsen 2011). We however, do not find this trend with age as a function of radius.

4.7.5 Masses and Ages as a Function of Galactocentric Radius

Figures 4.12 and 4.11 show the mass and age of the clusters as a function of galactocentric radius, respectively. No correlation in our data.

Others have found that the star formation in the outer disk (Barnes et al. (2012), Tran et al. submitted) clusters are smaller than inner disk clusters, however this trend does not seem to be the case for the mass and radius as a function of the galaxy's radius.

4.8 Summary and Conclusions

- We measure the masses and ages of 470 clusters in NGC 6946.
- We determine the cluster formation efficiency (Γ) to be $4 \pm 0.9\%$ for clusters younger than 5 Myr and $4 \pm 2.3\%$ for clusters younger than 25 Myr.
- We find the relationship between Γ and the star formation rate surface density from

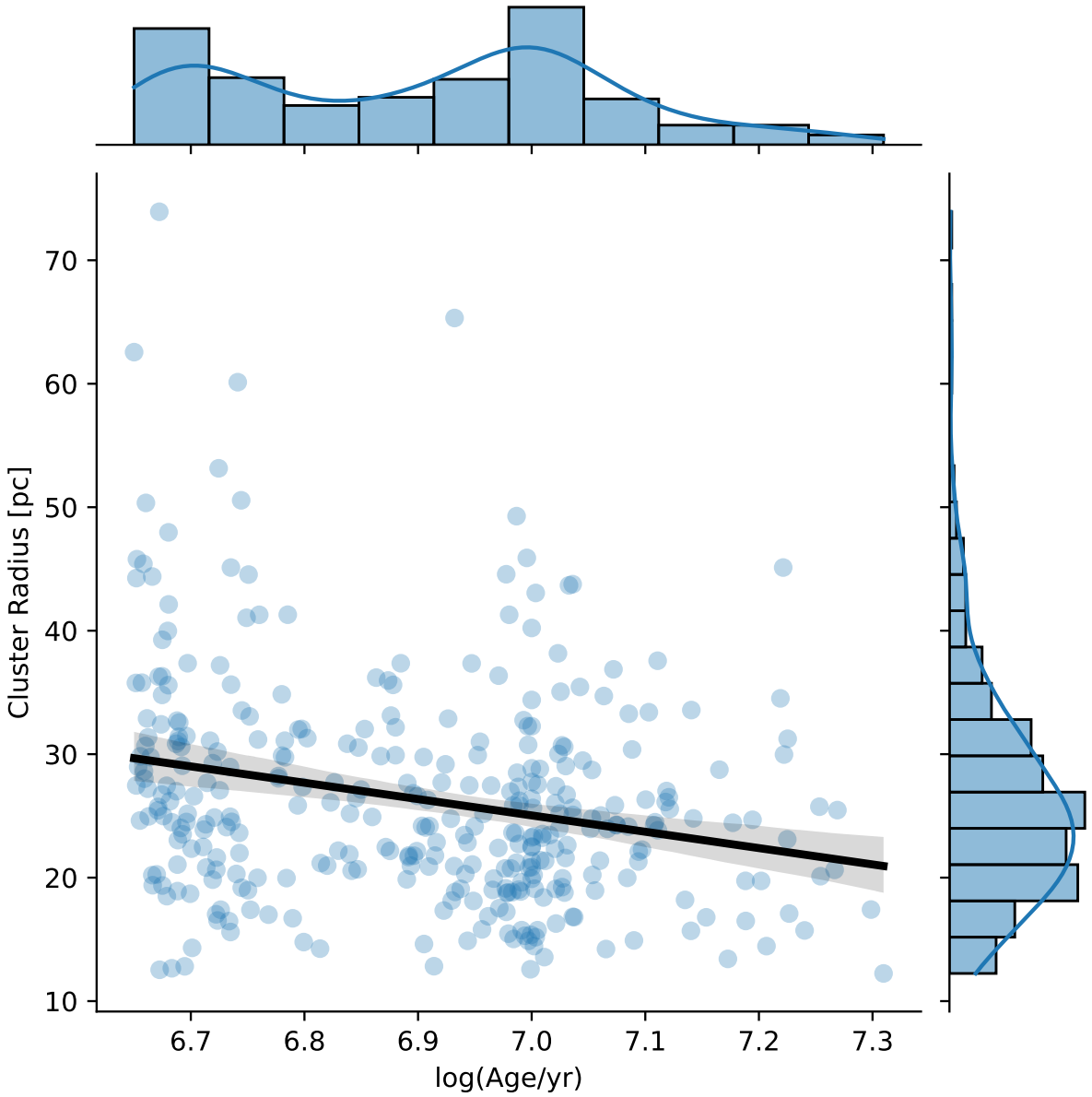

Figure 4.10 Radius as a function of age for each cluster. There appears to be a negative correlation between age and radius, however, there is large scatter in the radius. More data will be needed to determine any correlations further.

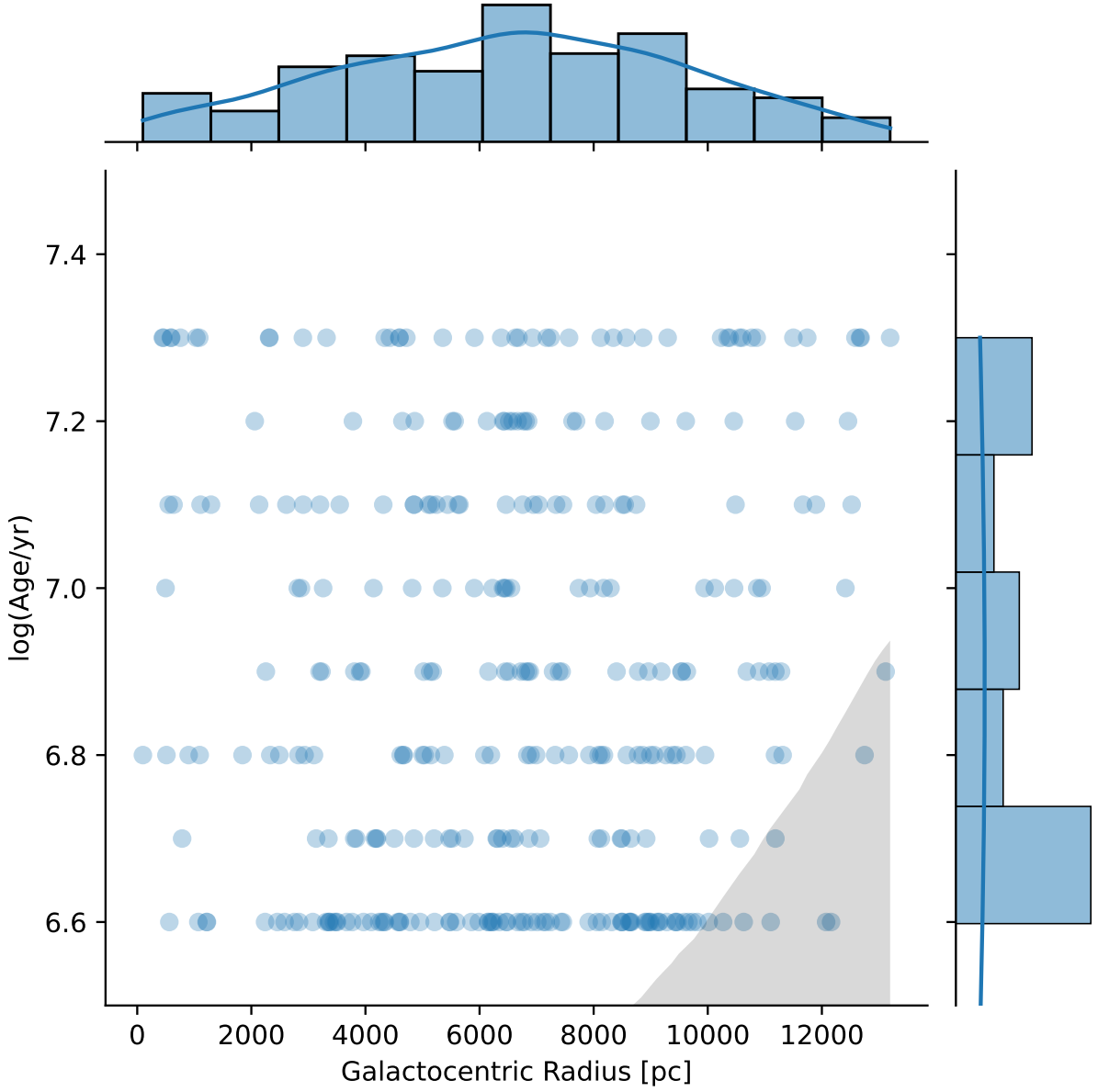

Figure 4.11 There appears to be no correlation in age as a function of galactocentric radius.

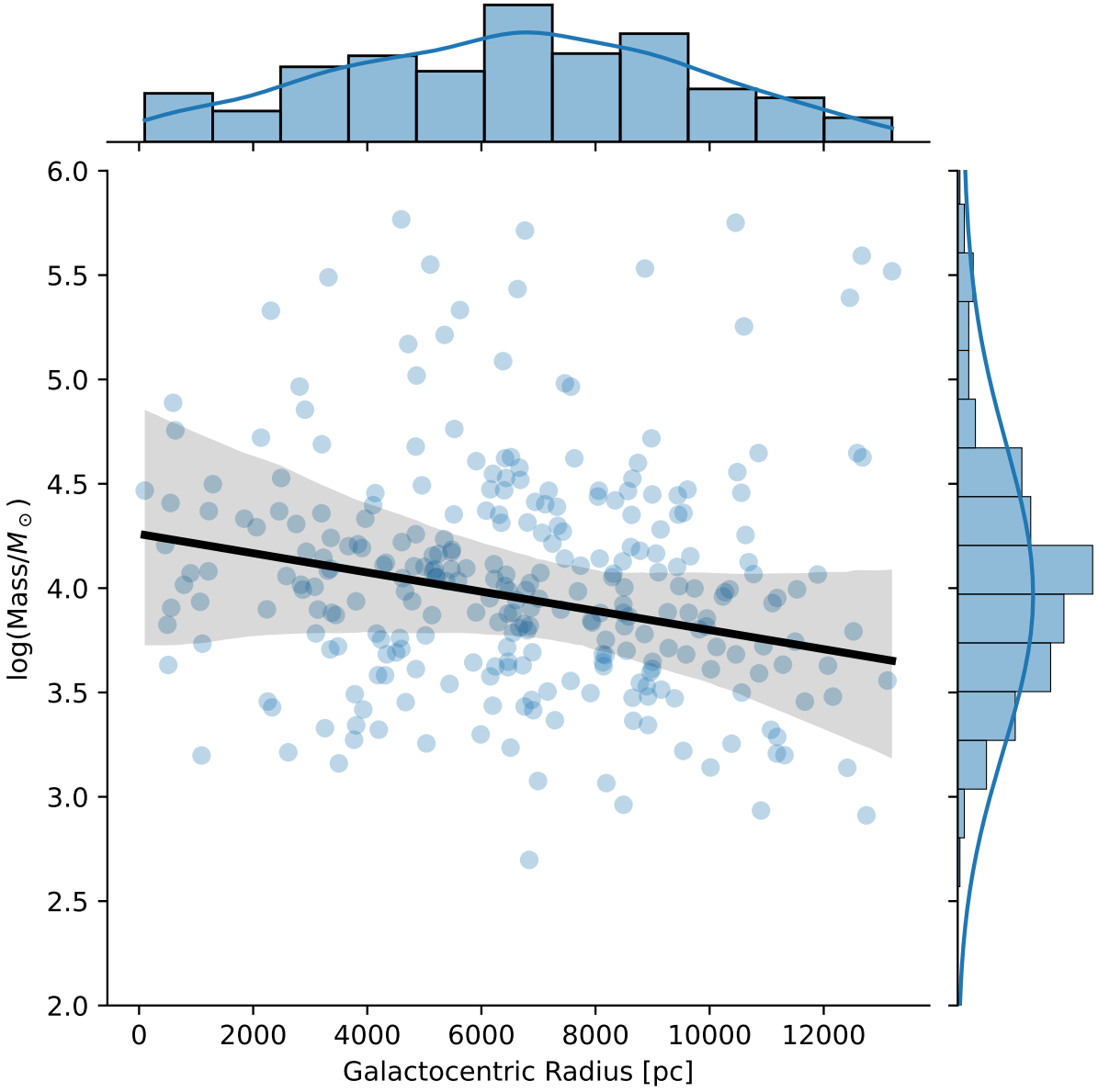

Figure 4.12 There appears to be no correlation in mass as a function of galactocentric radius.

Kruijssen (2012) to be scale-independent in NGC 6946.

- We find a positive correlation between cluster mass-radius, with more massive clusters living longer, while low-mass clusters dissolve over shorter timescales.

- We find a marked decrease in number of young clusters after 10 Myr in NGC 6946.

- We fit a single power law to the mass function in NGC 6946 obtaining a slope of 1.83 $\pm$ 0.04. This work will be submitted for peer-reviewed publication with comparisons in fit between the single power law and a Schechter function.

Chapter 5

CONCLUSIONS AND FUTURE WORK

5.1 Summary

The primary goal of this dissertation was to use resolved stellar photometry of star-forming galaxy NGC 6946 (The Fireworks Galaxy) taken with the Hubble Space Telescope's (HST) Wide Field Camera 3 (WFC3) with F275W and F336W filters to put new constraints on the relationships between the spatial distribution of ages, formation rate, masses, radii, colors, and luminosity for massive stars and massive star clusters.

In chapter 2, I measured the resolved recent ($\lesssim$ 25 Myr) star formation history of NGC 6946 using MATCH, a color magnitude diagram (CMD)-fitting code described in Dolphin (2002). To create maps of the young stellar populations at multiple time bins, I first divided the HST WFC3 NUV photometry obtained using DOLPHOT, a stellar photometry package using point spread function- (PSF-)fitting, into grids. I implemented a quadtree algorithm, which operates as follows. First, it counts the number of stars in a region. If the number of stars in the square is higher than a certain threshold, then it will subdivide into four equal parts. This iterates until it hits a minimum grid size, which is roughly 3 arcseconds by 3 arcseconds, chosen because that is the approximate size of clusters in NGC 6946. This gridding schema ensures the denser regions are divided into finer grids and the less dense regions into coarser grids. This saves computational time by having large less dense grids and ensures there are sufficient numbers of stars for statistics in the finer grids while maintaining high resolution in areas of high stellar density. I divide the grids into separated density bins and create at least 30,000 artificial stars per density bin to test the completeness of our photometry.

For each individual spatial bin (or grid), MATCH creates Hess-diagrams or binned CMDs

of stars in the bin. MATCH will then take user-defined ranges in age, metallicity, distance, and extinction as well as IMF and binary fraction to create individual synthetic CMDs for each possible combination of parameters. MATCH accounts for photometric errors and completeness using the artificial star tests from the section above. These individual CMDs are linearly combined to form composite CMDs, which are compared to the observed CMDs. These composite synthetic CMDs tell us exactly what ages and metallicities make up the observed region and its resulting star formation history. We will take the ages from each grid and stitch them together to form a resolved map of ages in NGC 6946. By dividing these spatially-resolved age maps into various time bins, essentially mapping where the oldest to youngest stars are, we can trace the structure in NGC 6946 over time and measure the age gradients.

In this work, we learned the global star formation rate ((age$\leq$25 Myr)=$13.17^{+0.91}_{-0.79} M_{\odot}$/yr) of NGC 6946 has been decreasing in the past 25 million years, save for a few highly active star forming regions in the tip of the northeast spiral arm and Hodge's Complex. We examined the stellar density as a function of age, showing the stellar density increases as the stellar population gets older. We find the frequent supernovae are consistent with the higher star formation rate 25 Myr, despite the low star formation rate found in measurements of the recent formation rate ($\leq$ 10 Myr).

In chapter 3, I created a cluster candidate-finding algorithm, tested it on NGC 6946 using the photometric catalog that was published alongside the previous chapter. It detects the areas of the steepest gradient in stellar density, thins the edges, and links the edges via hysteresis. This algorithm is based off of the cutting-edge Canny detection algorithm that does the same with image data, which is currently used for everything from detecting lines on roads for self-driving cars to cancerous tumors on x-rays. I extensively tested this algorithm using artificial clusters, finding that it detects 49.8% of the inserted clusters with a false positive rate of 7.8%. The clusters that are harder to detect are the fainter, less massive, and less dense clusters. We identified 767 new cluster and association candidates in NGC 6946 using this algorithm. I presented the integrated F275W and F336W magnitudes

of each cluster, fit the corrected cluster luminosity function for NGC 6946, finding a slope of $\alpha_{275} = 1.68 \pm 0.02$ for F275W and $\alpha_{336} = 1.69 \pm 0.08$ for F336W, which is consistent with the less steep slopes measured in NUV filters. I found that the radius and brightness of the clusters decreased as radius of the galaxy increased, showing that the outer parts of the galaxy have less favorable star forming environments.

In chapter 4, I utilized the stellar and cluster catalogs published alongside the previous chapters and fitted the color-magnitude diagrams of the stars within each cluster for a single stellar population. We determined the best-fit age for 552 cluster/association candidates. We found the cluster mass function slope to be 1.83 ± 0.04. We find a slight correlation between mass and age in the clusters detected, where longer-lived clusters are more likely to be massive. We find the cluster formation efficiency to be 4%, typical CFE values in the literature.

5.2 Future Work

To continue the work done in this dissertation, I will measure an additional 13 bands (∼200 visits) of archival optical and infrared (IR) HST WFC3 and Advanced Camera for Surveys (ACS) photometry of individual stars and clusters (Figure 5.1, Table 5.1). The photometry library of this massive star population will be used as a tool to probe star formation at galactic and cluster scales. With the stellar photometry, I will fit spectral energy distributions (SEDs) for over 8 million stars in NGC 6946 to investigate how local environments and large scale mechanisms influence the formation of stars. Specifically, we will test density wave theory by measuring the ages of the resolved stars in the spiral arms. With the cluster photometry, I will constrain the cluster mass-radius relation and age, mass, and luminosity functions of clusters. Additionally, we will be able to infer the relationship between age and density in the spiral arms and test diagnostics for star formation rate (SFR) and whether they are consistent with the unusually high observed rate of supernovae (10 in the past century).

I have begun this work by filtering through the large amount of archival data available and am removing the cosmic rays in the raw images to allow me to align the data. Following

Instrument	Filter	Number of Visits	Estimated Total Exposure Time [s]
WFC3/UVIS	F275W	15	84694
WFC3/UVIS	F336W	15	39525
WFC3/UVIS	F438W	3	8314
WFC3/UVIS	F547M	7	103111
WFC3/UVIS	F555W	5	4560
WFC3/UVIS	F606W	36	84392
WFC3/UVIS	F657N	7	19782
WFC3/UVIS	F658N	1	700
WFC3/UVIS	F673N	7	26971
WFC3/UVIS	F814W	26	64722
WFC3/IR	F110W	22	13837
WFC3/IR	F128N	9	12706
WFC3/IR	F160W	18	16574
WFC3/IR	F164N	9	21572
ACS/WFC	F435W	19	112365

Table 5.1 Estimates of the total exposure times available in the archive for WFC3 and ACS filter observations of NGC 6946.

this, I will analyze the data using techniques similar to those used by the Panchromatic Hubble Andromeda Treasury (PHAT; Williams et al. (2014)). I will perform crowded-field photometry on each individual exposure (>400 exposures) listed in Table 5.1 using the point spread function (PSF) fitting routine DOLPHOT (Dolphin, 2000). I will match the stars in the overlapping frames, measure the distance between the matched stars, apply those residuals to obtain accurate astrometry, and update the headers. We will flag the data with quality metrics, including signal to noise, crowding, and sharpness. We will perform artificial star tests to determine the 50% completeness of our sample in the different bands.

By obtaining matched UV, optical, and IR photometry, we will have 15 total bands to model the photometric spectral energy distributions of >8 million individual stars with the Bayesian Extinction and Stellar Tool (BEAST; Gordon et al. (2016)). The BEAST uses a probabilistic approach to SED-fittng, has been optimized for large multi-band surveys, and accounts for dust. The overlapping narrow and medium bands will provide additional

constraints which will ultimately give better SED fits. These SED fits will give us the resolved masses, ages, and temperatures of over 8 million stars in NGC 6946. We will use these parameters to create age and mass maps.

5.3 Legacy Value

With the publication of the results from this thesis, I have published a stellar photometric catalog (which will be expanded upon by 13 bands in my future work) and a young massive cluster and association catalog. Additionally, in my future work, I will be publishing the resulting SEDs of over 8 million stars and a globular cluster catalog for NGC 6946. These catalogs will enable the improvement of population synthesis models by providing observational constraints for interpreting spectra of unresolved regions in galaxies, i.e. with integral field spectrograph data. The cluster catalog, in particular, will be essential for comparing to simulations, like FIRE (Grudić et al., 2022) as the resolution of these simulations improves. Since NGC 6946 has existing maps of its molecular gas (Bigiel et al., 2020; Rebolledo et al., 2012), a comprehensive resolved map of the young stellar clusters born out of those giant molecular clouds will provide direct observational constraints on star formation. Additionally, we will make the well-tested computer vision algorithm open source so that others will be able to apply our cluster detection techniques to other galaxies.

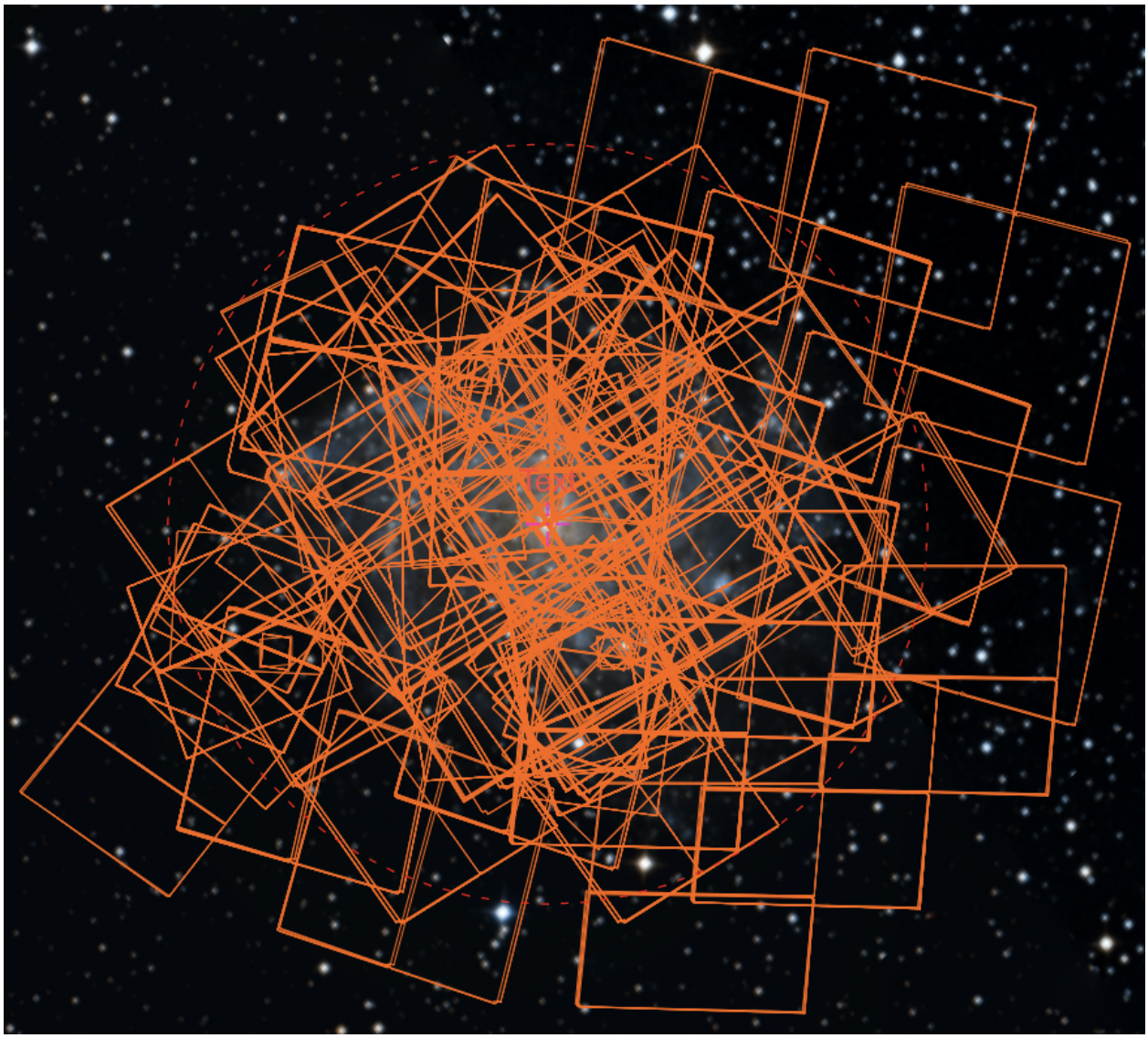

Figure 5.1 Footprints of the ∼200 visit coverage across NGC 6946. Specific bands and number of visits listed in Table 5.1.

BIBLIOGRAPHY

Adamo, A., Kruijssen, J. M. D., Bastian, N., Silva-Villa, E., & Ryon, J. 2015, MNRAS, 452, 246, doi: 10.1093/mnras/stv1203

Adamo, A., Östlin, G., & Zackrisson, E. 2011, MNRAS, 417, 1904, doi: 10.1111/j.1365-2966.2011.19377.x

Adamo, A., Östlin, G., Zackrisson, E., et al. 2010, MNRAS, 407, 870, doi: 10.1111/j.1365-2966.2010.16983.x

Adamo, A., Ryon, J. E., Messa, M., et al. 2017, ApJ, 841, 131, doi: 10.3847/1538-4357/aa7132

Adamo, A., Zeidler, P., Kruijssen, J. M. D., et al. 2020a, SSRv, 216, 69, doi: 10.1007/s11214-020-00690-x

Adamo, A., Hollyhead, K., Messa, M., et al. 2020b, MNRAS, 499, 3267, doi: 10.1093/mnras/staa2380

Alfaro, E. J., & Román-Zúñiga, C. G. 2018, MNRAS, 478, L110, doi: 10.1093/mnrasl/sly075

Anand, G. S., Rizzi, L., & Tully, R. B. 2018, AJ, 156, 105, doi: 10.3847/1538-3881/aad3b2

Aouad, C. J., James, P. A., & Chilingarian, I. V. 2020, MNRAS, 496, 5211, doi: 10.1093/mnras/staa1945

Astropy Collaboration, Robitaille, T. P., Tollerud, E. J., et al. 2013, A&A, 558, A33, doi: 10.1051/0004-6361/201322068

Astropy Collaboration, Price-Whelan, A. M., Sipőcz, B. M., et al. 2018, AJ, 156, 123, doi: 10.3847/1538-3881/aabc4f

Astropy Collaboration, Price-Whelan, A. M., Lim, P. L., et al. 2022, ApJ, 935, 167, doi: 10.3847/1538-4357/ac7c74

Bacchini, C., Fraternali, F., Pezzulli, G., et al. 2019, A&A, 632, A127, doi: 10.1051/0004-6361/201936559

Barnes, K. L., van Zee, L., Côté, S., & Schade, D. 2012, ApJ, 757, 64, doi: 10.1088/0004-637X/757/1/64

Bastian, N. 2008, MNRAS, 390, 759, doi: 10.1111/j.1365-2966.2008.13775.x

Bastian, N., Ercolano, B., Gieles, M., et al. 2007, MNRAS, 379, 1302, doi: 10.1111/j.1365-2966.2007.12064.x

Bastian, N., Gieles, M., Efremov, Y. N., & Lamers, H. J. G. L. M. 2005a, A&A, 443, 79, doi: 10.1051/0004-6361:20053165

Bastian, N., Gieles, M., Lamers, H. J. G. L. M., Scheepmaker, R. A., & de Grijs, R. 2005b, A&A, 431, 905, doi: 10.1051/0004-6361:20041078

Bastian, N., Adamo, A., Gieles, M., et al. 2012, MNRAS, 419, 2606, doi: 10.1111/j.1365-2966.2011.19909.x

Battinelli, P. 1991, A&A, 244, 69

Baumgardt, H., & Kroupa, P. 2007, MNRAS, 380, 1589, doi: 10.1111/j.1365-2966.2007.12209.x

Baumgardt, H., Parmentier, G., Anders, P., & Grebel, E. K. 2013, MNRAS, 430, 676, doi: 10.1093/mnras/sts667

Beroiz, M., Cabral, J., & Sanchez, B. 2020, Astronomy and Computing, 32, 100384, doi: 10.1016/j.ascom.2020.100384

Bertin, E., & Arnouts, S. 1996, A&AS, 117, 393, doi: 10.1051/aas:1996164

Bigiel, F., Leroy, A., Walter, F., et al. 2008, AJ, 136, 2846, doi: 10.1088/0004-6256/136/6/2846

Bigiel, F., de Looze, I., Krabbe, A., et al. 2020, ApJ, 903, 30, doi: 10.3847/1538-4357/abb677

Blanc, G., & Greggio, L. 2008, NewA, 13, 606, doi: 10.1016/j.newast.2008.03.010

Blitz, L. 1993, in Protostars and Planets III, ed. E. H. Levy & J. I. Lunine, 125

Bonnell, I. A., Bate, M. R., Clarke, C. J., & Pringle, J. E. 2001, MNRAS, 323, 785, doi: 10.1046/j.1365-8711.2001.04270.x

Boss, A. P., & Keiser, S. A. 2013, ApJ, 764, 136, doi: 10.1088/0004-637X/764/2/136

Botticella, M. T., Smartt, S. J., Kennicutt, R. C., et al. 2012, A&A, 537, A132, doi: 10.1051/0004-6361/201117343

Bourke, T. L., Myers, P. C., Robinson, G., & Hyland, A. R. 2001, ApJ, 554, 916, doi: 10.1086/321405

Boylan-Kolchin, M. 2018, MNRAS, 479, 332, doi: 10.1093/mnras/sty1490

Bradski, G. 2000, Dr. Dobb's Journal of Software Tools

Bresolin, F. 2019, MNRAS, 488, 3826, doi: 10.1093/mnras/stz1947

Bressan, A., Marigo, P., Girardi, L., et al. 2012, MNRAS, 427, 127, doi: 10.1111/j.1365-2966.2012.21948.x

Bressert, E., Bastian, N., Gutermuth, R., et al. 2010, MNRAS, 409, L54, doi: 10.1111/j.1745-3933.2010.00946.x

Brown, G., & Gnedin, O. Y. 2021, MNRAS, 508, 5935, doi: 10.1093/mnras/stab2907

Buat, V., Iglesias-Páramo, J., Seibert, M., et al. 2005, ApJL, 619, L51, doi: 10.1086/423241

Canizares, C. R., Kriss, G. A., & Feigelson, E. D. 1982, ApJL, 253, L17, doi: 10.1086/183728

Canny, J. 1986, IEEE Transactions on Pattern Analysis and Machine Intelligence, PAMI-8, 679, doi: 10.1109/TPAMI.1986.4767851

Cartwright, A., & Whitworth, A. P. 2004, Monthly Notices of the Royal Astronomical Society, 348, 589, doi: 10.1111/j.1365-2966.2004.07360.x

Chabrier, G. 2003, PASP, 115, 763, doi: 10.1086/376392

Chandar, R., Fall, S. M., & Whitmore, B. C. 2006, ApJL, 650, L111, doi: 10.1086/508890

—. 2015, ApJ, 810, 1, doi: 10.1088/0004-637X/810/1/1

Chandar, R., Fall, S. M., Whitmore, B. C., & Mulia, A. J. 2017, ApJ, 849, 128, doi: 10.3847/1538-4357/aa92ce

Chandar, R., Whitmore, B. C., Dinino, D., et al. 2016, ApJ, 824, 71, doi: 10.3847/0004-637X/824/2/71

Chandar, R., Whitmore, B. C., Kim, H., et al. 2010, ApJ, 719, 966, doi: 10.1088/0004-637X/719/1/966

Chevance, M., Kruijssen, J. M. D., Vazquez-Semadeni, E., et al. 2020a, SSRv, 216, 50, doi: 10.1007/s11214-020-00674-x

Chevance, M., Kruijssen, J. M. D., Hygate, A. P. S., et al. 2020b, MNRAS, 493, 2872, doi: 10.1093/mnras/stz3525

Chiappini, C., Matteucci, F., & Gratton, R. 1997, ApJ, 477, 765, doi: 10.1086/303726

Choi, Y., Dalcanton, J. J., Williams, B. F., et al. 2015, ApJ, 810, 9, doi: 10.1088/0004-637X/810/1/9

—. 2020, ApJ, 902, 54, doi: 10.3847/1538-4357/abb467

Choksi, N., & Kruijssen, J. M. D. 2021, MNRAS, 507, 5492, doi: 10.1093/mnras/stab2514

Clark, P. C., Glover, S. C. O., Klessen, R. S., & Bromm, V. 2011, ApJ, 727, 110, doi: 10.1088/0004-637X/727/2/110

Colombo, D., Kalinova, V., Utomo, D., et al. 2018, MNRAS, 475, 1791, doi: 10.1093/mnras/stx3233

Cook, D. O., Lee, J. C., Adamo, A., et al. 2019, Monthly Notices of the Royal Astronomical Society, 484, 4897, doi: 10.1093/mnras/stz331

Cook, D. O., Lee, J. C., Adamo, A., et al. 2023, MNRAS, 519, 3749, doi: 10.1093/mnras/stac3748

Corbelli, E., Braine, J., Bandiera, R., et al. 2017, A&A, 601, A146, doi: 10.1051/0004-6361/201630034

Costa, G., Girardi, L., Bressan, A., et al. 2019a, A&A, 631, A128, doi: 10.1051/0004-6361/201936409

—. 2019b, MNRAS, 485, 4641, doi: 10.1093/mnras/stz728

Crutcher, R. M. 1999, ApJ, 520, 706, doi: 10.1086/307483

Daddi, E., Elbaz, D., Walter, F., et al. 2010, ApJL, 714, L118, doi: 10.1088/2041-8205/714/1/L118

Dale, D. A., Roussel, H., Contursi, A., et al. 2004, ApJ, 601, 813, doi: 10.1086/380753

Dale, J. E., Ercolano, B., & Bonnell, I. A. 2013, MNRAS, 430, 234, doi: 10.1093/mnras/sts592

de Blok, W. J. G., Walter, F., Brinks, E., et al. 2008, AJ, 136, 2648, doi: 10.1088/0004-6256/136/6/2648

de Grijs, R., & Anders, P. 2006, MNRAS, 366, 295, doi: 10.1111/j.1365-2966.2005.09856.x

de la Fuente Marcos, R., & de la Fuente Marcos, C. 2009, ApJ, 700, 436, doi: 10.1088/0004-637X/700/1/436

de Rossi, M. E., Tissera, P. B., De Lucia, G., & Kauffmann, G. 2009, MNRAS, 395, 210, doi: 10.1111/j.1365-2966.2009.14560.x

Degioia-Eastwood, K., Grasdalen, G. L., Strom, S. E., & Strom, K. M. 1984, ApJ, 278, 564, doi: 10.1086/161823

Dib, S., Helou, G., Moore, T. J. T., Urquhart, J. S., & Dariush, A. 2012, ApJ, 758, 125, doi: 10.1088/0004-637X/758/2/125

Dib, S., Hennebelle, P., Pineda, J. E., et al. 2010, ApJ, 723, 425, doi: 10.1088/0004-637X/723/1/425

Dib, S., Walcher, C. J., Heyer, M., Audit, E., & Loinard, L. 2009, MNRAS, 398, 1201, doi: 10.1111/j.1365-2966.2009.15201.x

Dobbs, C. L. 2008, MNRAS, 391, 844, doi: 10.1111/j.1365-2966.2008.13939.x

Dobbs, C. L., Bonnell, I. A., & Pringle, J. E. 2006, MNRAS, 371, 1663, doi: 10.1111/j.1365-2966.2006.10794.x

Dobbs, C. L., & Pringle, J. E. 2010, MNRAS, 409, 396, doi: 10.1111/j.1365-2966.2010.17323.x

Dobbs, C. L., Krumholz, M. R., Ballesteros-Paredes, J., et al. 2014, in Protostars and Planets VI, ed. H. Beuther, R. S. Klessen, C. P. Dullemond, & T. Henning, 3–26, doi: 10.2458/azu_uapress_9780816531240-ch001

Dobbs, C. L., Adamo, A., Few, C. G., et al. 2017, MNRAS, 464, 3580, doi: 10.1093/mnras/stw2200

Dolphin, A. E. 2000, PASP, 112, 1383, doi: 10.1086/316630

—. 2002, MNRAS, 332, 91, doi: 10.1046/j.1365-8711.2002.05271.x

—. 2016, DOLPHOT: Stellar photometry, http://ascl.net/1608.013

Donas, J., Deharveng, J. M., Laget, M., Milliard, B., & Huguenin, D. 1987, A&A, 180, 12

Downes, D., & Solomon, P. M. 1998, ApJ, 507, 615, doi: 10.1086/306339

Duane, S., Kennedy, A., Pendleton, B. J., & Roweth, D. 1987, Physics Letters B, 195, 216, doi: https://doi.org/10.1016/0370-2693(87)91197-X

Efremov, Y. N., & Elmegreen, B. G. 1998, MNRAS, 299, 588, doi: 10.1046/j.1365-8711.1998.01819.x

Efremov, Y. N., & Moiseev, A. V. 2016, MNRAS, 461, 2993, doi: 10.1093/mnras/stw1469

Efremov, Y. N., Afanasiev, V. L., Alfaro, E. J., et al. 2007, MNRAS, 382, 481, doi: 10.1111/j.1365-2966.2007.12260.x

Eibensteiner, C., Barnes, A. T., Bigiel, F., et al. 2022, A&A, 659, A173, doi: 10.1051/0004-6361/202142624

Ekström, S., Georgy, C., Eggenberger, P., et al. 2012, A&A, 537, A146, doi: 10.1051/0004-6361/201117751

Eldridge, J. J., & Xiao, L. 2019, MNRAS, 485, L58, doi: 10.1093/mnrasl/slz030

Elmegreen, B. G. 2008, ApJ, 672, 1006, doi: 10.1086/523791

—. 2010, ApJL, 712, L184, doi: 10.1088/2041-8205/712/2/L184

—. 2018, ApJ, 853, 88, doi: 10.3847/1538-4357/aaa252

Elmegreen, B. G., & Efremov, Y. N. 1997, ApJ, 480, 235, doi: 10.1086/303966

Elmegreen, B. G., & Elmegreen, D. M. 2019, ApJS, 245, 14, doi: 10.3847/1538-4365/ab4903

Elmegreen, B. G., Elmegreen, D. M., Chandar, R., Whitmore, B., & Regan, M. 2006, ApJ, 644, 879, doi: 10.1086/503797

Elmegreen, B. G., & Falgarone, E. 1996, ApJ, 471, 816, doi: 10.1086/178009

Elmegreen, B. G., Hurst, R., & Koenig, X. 2014, ApJL, 782, L1, doi: 10.1088/2041-8205/782/1/L1

Elmegreen, B. G., & Scalo, J. 2004, ARA&A, 42, 211, doi: 10.1146/annurev.astro.41.011802.094859

Elmegreen, B. G., Adamo, A., Boquien, M., et al. 2020, ApJL, 888, L27, doi: 10.3847/2041-8213/ab632a

Elmegreen, D. M., Chromey, F. R., & Santos, M. 1998, AJ, 116, 1221, doi: 10.1086/300522

Engargiola, G., Plambeck, R. L., Rosolowsky, E., & Blitz, L. 2003, ApJS, 149, 343, doi: 10.1086/379165

Engelbracht, C. W., Rieke, M. J., Rieke, G. H., & Latter, W. B. 1996, ApJ, 467, 227, doi: 10.1086/177598

Escala, A., & Larson, R. B. 2008, ApJL, 685, L31, doi: 10.1086/592271

Evans, N. J., Kim, J.-G., & Ostriker, E. C. 2022, The Astrophysical Journal Letters, 929, L18, doi: 10.3847/2041-8213/ac6427

Fall, S. M., Chandar, R., & Whitmore, B. C. 2005, ApJL, 631, L133, doi: 10.1086/496878

Faucher-Giguère, C.-A., Quataert, E., & Hopkins, P. F. 2013, MNRAS, 433, 1970, doi: 10.1093/mnras/stt866

Federrath, C. 2013, MNRAS, 436, 3167, doi: 10.1093/mnras/stt1799

Federrath, C. 2013, MNRAS, 436, 1245, doi: 10.1093/mnras/stt1644

Feitzinger, J. V., & Galinski, T. 1987, A&A, 179, 249

Feldmann, R., Gnedin, N. Y., & Kravtsov, A. V. 2011, ApJ, 732, 115, doi: 10.1088/0004-637X/732/2/115

Felzenszwalb, P. F., & Huttenlocher, D. P. 2004, International Journal of Computer Vision, 59, 167

Fleck, Robert C., J. 1996, ApJ, 458, 739, doi: 10.1086/176853

Fouesneau, M., Johnson, L. C., Weisz, D. R., et al. 2014, ApJ, 786, 117, doi: 10.1088/0004-637X/786/2/117

Foyle, K., Rix, H. W., Walter, F., & Leroy, A. K. 2010, ApJ, 725, 534, doi: 10.1088/0004-637X/725/1/534

Fukui, Y., Mizuno, N., Yamaguchi, R., Mizuno, A., & Onishi, T. 2001, PASJ, 53, L41, doi: 10.1093/pasj/53.6.L41

Gaia Collaboration, Prusti, T., de Bruijne, J. H. J., et al. 2016, A&A, 595, A1, doi: 10.1051/0004-6361/201629272

Gaia Collaboration, Brown, A. G. A., Vallenari, A., et al. 2018, A&A, 616, A1, doi: 10.1051/0004-6361/201833051

Gallagher, M. J., Leroy, A. K., Bigiel, F., et al. 2018, ApJ, 858, 90, doi: 10.3847/1538-4357/aabad8

Geen, S., Rosdahl, J., Blaizot, J., Devriendt, J., & Slyz, A. 2015, MNRAS, 448, 3248, doi: 10.1093/mnras/stv251

Gentry, E. S., Krumholz, M. R., Dekel, A., & Madau, P. 2017, MNRAS, 465, 2471, doi: 10.1093/mnras/stw2746

Genzel, R., Tacconi, L. J., Gracia-Carpio, J., et al. 2010, MNRAS, 407, 2091, doi: 10.1111/j.1365-2966.2010.16969.x

Ghita, O., & Whelan, P. F. 2002, Journal of Electronic Imaging, 11, 479 , doi: 10.1117/1.1501574

Gieles, M. 2009, MNRAS, 394, 2113, doi: 10.1111/j.1365-2966.2009.14473.x

Gieles, M., Larsen, S. S., Bastian, N., & Stein, I. T. 2006, A&A, 450, 129, doi: 10.1051/0004-6361:20053589

Gieles, M., & Renaud, F. 2016, MNRAS, 463, L103, doi: 10.1093/mnrasl/slw163

Gil de Paz, A., Boissier, S., Madore, B. F., et al. 2007, ApJS, 173, 185, doi: 10.1086/516636

Girardi, L., Williams, B. F., Gilbert, K. M., et al. 2010, ApJ, 724, 1030, doi: 10.1088/0004-637X/724/2/1030

Girichidis, P., Federrath, C., Banerjee, R., & Klessen, R. S. 2011, MNRAS, 413, 2741, doi: 10.1111/j.1365-2966.2011.18348.x

—. 2012, MNRAS, 420, 613, doi: 10.1111/j.1365-2966.2011.20073.x

Girichidis, P., Walch, S., Naab, T., et al. 2016, MNRAS, 456, 3432, doi: 10.1093/mnras/stv2742

Girichidis, P., Offner, S. S. R., Kritsuk, A. G., et al. 2020, SSRv, 216, 68, doi: 10.1007/s11214-020-00693-8

Gnedin, N. Y. 2016, Saas-Fee Advanced Course, 43, 1, doi: 10.1007/978-3-662-47890-5_1

Goddard, Q. E., Bastian, N., & Kennicutt, R. C. 2010a, MNRAS, 405, 857, doi: 10.1111/j.1365-2966.2010.16511.x

—. 2010b, MNRAS, 405, 857, doi: 10.1111/j.1365-2966.2010.16511.x

Goldreich, P., & Lynden-Bell, D. 1965, Monthly Notices of the Royal Astronomical Society, 130, 125, doi: 10.1093/mnras/130.2.125

Gordon, K. D., Fouesneau, M., Arab, H., et al. 2016, ApJ, 826, 104, doi: 10.3847/0004-637X/826/2/104

Gorski, M., Ott, J., Rand, R., et al. 2018, ApJ, 856, 134, doi: 10.3847/1538-4357/aab3cc

Gouliermis, D. A. 2018, PASP, 130, 072001, doi: 10.1088/1538-3873/aac1fd

Gouliermis, D. A., Schmeja, S., Klessen, R. S., de Blok, W. J. G., & Walter, F. 2010, ApJ, 725, 1717, doi: 10.1088/0004-637X/725/2/1717

Gouliermis, D. A., Elmegreen, B. G., Elmegreen, D. M., et al. 2017, MNRAS, 468, 509, doi: 10.1093/mnras/stx445

Grasha, K., Calzetti, D., Adamo, A., et al. 2017a, ApJ, 840, 113, doi: 10.3847/1538-4357/aa6f15

Grasha, K., Elmegreen, B. G., Calzetti, D., et al. 2017b, ApJ, 842, 25, doi: 10.3847/1538-4357/aa740b

Grasha, K., Calzetti, D., Bittle, L., et al. 2018, MNRAS, 481, 1016, doi: 10.1093/mnras/sty2154

Grasha, K., Calzetti, D., Adamo, A., et al. 2019, MNRAS, 483, 4707, doi: 10.1093/mnras/sty3424

Greif, T. H., Springel, V., White, S. D. M., et al. 2011, ApJ, 737, 75, doi: 10.1088/0004-637X/737/2/75

Grudić, M. Y., Guszejnov, D., Offner, S. S. R., et al. 2022, MNRAS, 512, 216, doi: 10.1093/mnras/stac526

Grudić, M. Y., Kruijssen, J. M. D., Faucher-Giguère, C.-A., et al. 2021, MNRAS, 506, 3239, doi: 10.1093/mnras/stab1894

Gusev, A. S., & Shimanovskaya, E. V. 2019, MNRAS, 488, 3045, doi: 10.1093/mnras/stz1881

Gusev, A. S., Shimanovskaya, E. V., & Zaitseva, N. A. 2022, MNRAS, 514, 3953, doi: 10.1093/mnras/stac1592

Hagberg, A. A., Schult, D. A., & Swart, P. J. 2008, in Proceedings of the 7th Python in Science Conference, ed. G. Varoquaux, T. Vaught, & J. Millman, Pasadena, CA USA, 11 – 15

Hannon, S., Lee, J. C., Whitmore, B. C., et al. 2019, MNRAS, 490, 4648, doi: 10.1093/mnras/stz2820

Harris, C. R., Millman, K. J., van der Walt, S. J., et al. 2020, Nature, 585, 357, doi: 10.1038/s41586-020-2649-2

Harris, J., & Zaritsky, D. 2004, AJ, 127, 1531, doi: 10.1086/381953

—. 2009, AJ, 138, 1243, doi: 10.1088/0004-6256/138/5/1243

Hayward, C. C., & Hopkins, P. F. 2017, MNRAS, 465, 1682, doi: 10.1093/mnras/stw2888

Hennebelle, P., & Falgarone, E. 2012, A&A Rv, 20, 55, doi: 10.1007/s00159-012-0055-y

Herbig, G. H., & Terndrup, D. M. 1986, ApJ, 307, 609, doi: 10.1086/164447

Heyer, M., & Dame, T. M. 2015, ARA&A, 53, 583, doi: 10.1146/annurev-astro-082214-122324

Hill, A. S., Joung, M. R., Mac Low, M.-M., et al. 2012, ApJ, 750, 104, doi: 10.1088/0004-637X/750/2/104

Hillenbrand, L. A. 1997, AJ, 113, 1733, doi: 10.1086/118389

Hirano, S., Hosokawa, T., Yoshida, N., et al. 2014, ApJ, 781, 60, doi: 10.1088/0004-637X/781/2/60

Ho, L. C., Greene, J. E., Filippenko, A. V., & Sargent, W. L. W. 2009, ApJS, 183, 1, doi: 10.1088/0067-0049/183/1/1

Hocuk, S., & Spaans, M. 2011, A&A, 536, A41, doi: 10.1051/0004-6361/201117431

Hodge, P. W. 1967, PASP, 79, 29, doi: 10.1086/128432

Holtzman, J. A., Faber, S. M., Shaya, E. J., et al. 1992, AJ, 103, 691, doi: 10.1086/116094

Hopkins, P. F., Kereš, D., Oñorbe, J., et al. 2014, MNRAS, 445, 581, doi: 10.1093/mnras/stu1738

Hunter, D. A., Elmegreen, B. G., Dupuy, T. J., & Mortonson, M. 2003, AJ, 126, 1836, doi: 10.1086/378056

Hunter, J. D. 2007, Computing in Science and Engineering, 9, 90, doi: 10.1109/MCSE.2007.55

Jennings, Z. G., Williams, B. F., Murphy, J. W., et al. 2014, ApJ, 795, 170, doi: 10.1088/0004-637X/795/2/170

Jiménez-Donaire, M. J., Bigiel, F., Leroy, A. K., et al. 2019, ApJ, 880, 127, doi: 10.3847/1538-4357/ab2b95

Johnson, J. R., Koplitz, B., Williams, B. F., et al. 2023, ApJ, 945, 108, doi: 10.3847/1538-4357/acb775

Johnson, L. C., Seth, A. C., Dalcanton, J. J., et al. 2012, ApJ, 752, 95, doi: 10.1088/0004-637X/752/2/95

—. 2015, ApJ, 802, 127, doi: 10.1088/0004-637X/802/2/127

Johnson, L. C., Seth, A. C., Dalcanton, J. J., et al. 2016, The Astrophysical Journal, 827, 33, doi: 10.3847/0004-637X/827/1/33

Johnson, L. C., Seth, A. C., Dalcanton, J. J., et al. 2017, ApJ, 839, 78, doi: 10.3847/1538-4357/aa6a1f

Johnson, L. C., Wainer, T. M., Torresvillanueva, E. E., et al. 2022, ApJ, 938, 81, doi: 10.3847/1538-4357/ac8def

Jordahl, K., den Bossche, J. V., Fleischmann, M., et al. 2020, geopandas/geopandas: v0.8.1, v0.8.1, Zenodo, doi: 10.5281/zenodo.3946761

Julian, W. H., & Toomre, A. 1966, ApJ, 146, 810, doi: 10.1086/148957

Kang, Y., Bianchi, L., & Rey, S. C. 2009, Astrophysical Journal, 703, 614, doi: 10.1088/0004-637X/703/1/614

Karachentsev, I. D., Sharina, M. E., & Huchtmeier, W. K. 2000, A&A, 362, 544. https://arxiv.org/abs/astro-ph/0010148

Kauffmann, G., & Haehnelt, M. 2000, MNRAS, 311, 576, doi: 10.1046/j.1365-8711.2000.03077.x

Kennicutt, R. C., J. 1983, ApJ, 272, 54, doi: 10.1086/161261

Kennicutt, Robert C., J. 1989, ApJ, 344, 685, doi: 10.1086/167834

—. 1998a, ApJ, 498, 541, doi: 10.1086/305588

—. 1998b, ARA&A, 36, 189, doi: 10.1146/annurev.astro.36.1.189

Kennicutt, Robert C., J., Calzetti, D., Walter, F., et al. 2007, ApJ, 671, 333, doi: 10.1086/522300

Kennicutt, R. C., & Evans, N. J. 2012, ARA&A, 50, 531, doi: 10.1146/annurev-astro-081811-125610

Kennicutt, R. C., Calzetti, D., Aniano, G., et al. 2011, PASP, 123, 1347, doi: 10.1086/663818

Kim, C.-G., Kim, W.-T., & Ostriker, E. C. 2011, ApJ, 743, 25, doi: 10.1088/0004-637X/743/1/25

Kim, C.-G., & Ostriker, E. C. 2015, ApJ, 802, 99, doi: 10.1088/0004-637X/802/2/99

Kim, H., Whitmore, B. C., Chandar, R., et al. 2012, ApJ, 753, 26, doi: 10.1088/0004-637X/753/1/26

Kim, J., Chevance, M., Kruijssen, J. M. D., et al. 2023, ApJL, 944, L20, doi: 10.3847/2041-8213/aca90a

King, I. 1962, AJ, 67, 471, doi: 10.1086/108756

Klessen, R. S., & Glover, S. C. O. 2016, Saas-Fee Advanced Course, 43, 85, doi: 10.1007/978-3-662-47890-5_2

Konstantopoulos, I. S., Smith, L. J., Adamo, A., et al. 2013, AJ, 145, 137, doi: 10.1088/0004-6256/145/5/137

Koplitz, B., Johnson, J., Williams, B. F., et al. 2021, ApJ, 916, 58, doi: 10.3847/1538-4357/abfb7b

Kormendy, J., Drory, N., Bender, R., & Cornell, M. E. 2010, ApJ, 723, 54, doi: 10.1088/0004-637X/723/1/54

Kovesi, P. D. 2023, MATLAB and Octave Functions for Computer Vision and Image Processing, https://www.peterkovesi.com/matlabfns/

Krause, M. G. H., Offner, S. S. R., Charbonnel, C., et al. 2020, SSRv, 216, 64, doi: 10.1007/s11214-020-00689-4

Kravtsov, A. V. 2003, ApJL, 590, L1, doi: 10.1086/376674

Kreckel, K., Faesi, C., Kruijssen, J. M. D., et al. 2018, ApJL, 863, L21, doi: 10.3847/2041-8213/aad77d

Kroupa, P. 2001, MNRAS, 322, 231, doi: 10.1046/j.1365-8711.2001.04022.x

Kruijssen, J. M. D. 2012, MNRAS, 426, 3008, doi: 10.1111/j.1365-2966.2012.21923.x

Kruijssen, J. M. D., & Longmore, S. N. 2014, MNRAS, 439, 3239, doi: 10.1093/mnras/stu098

Kruijssen, J. M. D., Maschberger, T., Moeckel, N., et al. 2012, MNRAS, 419, 841, doi: 10.1111/j.1365-2966.2011.19748.x

Kruijssen, J. M. D., Schruba, A., Hygate, A. P. S., et al. 2018, MNRAS, 479, 1866, doi: 10.1093/mnras/sty1128

Kruijssen, J. M. D., Schruba, A., Chevance, M., et al. 2019, Nature, 569, 519, doi: 10.1038/s41586-019-1194-3

Krumholz, M. R., Burkhart, B., Forbes, J. C., & Crocker, R. M. 2018, MNRAS, 477, 2716, doi: 10.1093/mnras/sty852

Krumholz, M. R., Dekel, A., & McKee, C. F. 2012, ApJ, 745, 69, doi: 10.1088/0004-637X/745/1/69

Krumholz, M. R., & McKee, C. F. 2005, ApJ, 630, 250, doi: 10.1086/431734

Krumholz, M. R., McKee, C. F., & Bland-Hawthorn, J. 2019, ARA&A, 57, 227, doi: 10.1146/annurev-astro-091918-104430

Krumholz, M. R., McKee, C. F., & Tumlinson, J. 2009a, ApJ, 693, 216, doi: 10.1088/0004-637X/693/1/216

—. 2009b, ApJ, 699, 850, doi: 10.1088/0004-637X/699/1/850

Lada, C. J., & Lada, E. A. 2003, ARA&A, 41, 57, doi: 10.1146/annurev.astro.41.011802.094844

Lahén, N., Naab, T., Johansson, P. H., et al. 2019, ApJL, 879, L18, doi: 10.3847/2041-8213/ab2a13

Lamers, H. J. G. L. M., Baumgardt, H., & Gieles, M. 2010, MNRAS, 409, 305, doi: 10.1111/j.1365-2966.2010.17309.x

Larsen, S. S. 1999, A&AS, 139, 393, doi: 10.1051/aas:1999509

—. 2002, AJ, 124, 1393, doi: 10.1086/342381

—. 2004, A&A, 416, 537, doi: 10.1051/0004-6361:20034533

Larsen, S. S. 2006, in Planets to Cosmology: Essential Science in the Final Years of the Hubble Space Telescope, ed. M. Livio & S. Casertano, Vol. 18, 35

—. 2009, A&A, 494, 539, doi: 10.1051/0004-6361:200811212

Larsen, S. S., & Brodie, J. P. 2000, AJ, 120, 2938, doi: 10.1086/316847

Larsen, S. S., Brodie, J. P., Huchra, J. P., Forbes, D. A., & Grillmair, C. J. 2001, AJ, 121, 2974, doi: 10.1086/321081

Larsen, S. S., & Richtler, T. 1999a, A&A, 345, 59. https://arxiv.org/abs/astro-ph/9902227

—. 1999b, A&A, 345, 59, doi: 10.48550/arXiv.astro-ph/9902227

—. 2000, A&A, 354, 836, doi: 10.48550/arXiv.astro-ph/0001198

Larson, K. L., Díaz-Santos, T., Armus, L., et al. 2020, The Astrophysical Journal, 888, 92, doi: 10.3847/1538-4357/ab5dc3

Larson, K. L., Lee, J. C., Thilker, D. A., et al. 2023, MNRAS, 523, 6061, doi: 10.1093/mnras/stad1600

Larson, R. B. 1974, MNRAS, 166, 585, doi: 10.1093/mnras/166.3.585

Lazzarini, M., Williams, B. F., Durbin, M. J., et al. 2022, arXiv e-prints, arXiv:2206.11393. https://arxiv.org/abs/2206.11393

Lee, J. C., Whitmore, B. C., Thilker, D. A., et al. 2022, ApJS, 258, 10, doi: 10.3847/1538-4365/ac1fe5

Leroy, A. K., Walter, F., Brinks, E., et al. 2008, AJ, 136, 2782, doi: 10.1088/0004-6256/136/6/2782

Leroy, A. K., Walter, F., Sandstrom, K., et al. 2013, AJ, 146, 19, doi: 10.1088/0004-6256/146/2/19

Leroy, A. K., Sandstrom, K. M., Lang, D., et al. 2019, ApJS, 244, 24, doi: 10.3847/1538-4365/ab3925

Levesque, E., Dalcanton, J., Khan, R., et al. 2019, A Complete Inventory of the Fireworks Galaxy's O-Type Stars, HST Proposal. Cycle 27, ID. #15877

Lewis, A. R., Dolphin, A. E., Dalcanton, J. J., et al. 2015, ApJ, 805, 183, doi: 10.1088/0004-637X/805/2/183

Lewis, A. R., Simones, J. E., Johnson, B. D., et al. 2017, ApJ, 834, 70, doi: 10.3847/1538-4357/834/1/70

Li, Y., Mac Low, M.-M., & Klessen, R. S. 2005, ApJL, 620, L19, doi: 10.1086/428497

Lilly, S. J., Tresse, L., Hammer, F., Crampton, D., & Le Fevre, O. 1995, ApJ, 455, 108, doi: 10.1086/176560

Lin, C. C., & Shu, F. H. 1964, ApJ, 140, 646, doi: 10.1086/147955

Lindblad, B. 1963, Stockholms Observatoriums Annaler, 5, 5

Liu, D., Daddi, E., Schinnerer, E., et al. 2021, ApJ, 909, 56, doi: 10.3847/1538-4357/abd801

Liu, G., Koda, J., Calzetti, D., Fukuhara, M., & Momose, R. 2011, ApJ, 735, 63, doi: 10.1088/0004-637X/735/1/63

Longmore, S. N., Kruijssen, J. D., Bastian, N., et al. 2014, Protostars and planets VI, 291

Lopez, L. A., Krumholz, M. R., Bolatto, A. D., et al. 2014, ApJ, 795, 121, doi: 10.1088/0004-637X/795/2/121

Lucke, P. B., & Hodge, P. W. 1970, AJ, 75, 171, doi: 10.1086/110959

Mac Low, M.-M., & Klessen, R. S. 2004, Reviews of Modern Physics, 76, 125, doi: 10.1103/RevModPhys.76.125

Mackey, A. D., & Gilmore, G. F. 2003, MNRAS, 338, 85, doi: 10.1046/j.1365-8711.2003.06021.x

Madau, P., Ferguson, H. C., Dickinson, M. E., et al. 1996, MNRAS, 283, 1388, doi: 10.1093/mnras/283.4.1388

Maíz-Apellániz, J. 2001, ApJ, 563, 151, doi: 10.1086/323775

Marigo, P., Girardi, L., Bressan, A., et al. 2008, A&A, 482, 883, doi: 10.1051/0004-6361:20078467

Martell, S. L., Smolinski, J. P., Beers, T. C., & Grebel, E. K. 2011, A&A, 534, A136, doi: 10.1051/0004-6361/201117644

Martin, D., Fowlkes, C., & Malik, J. 2004, IEEE Transactions on Pattern Analysis and Machine Intelligence, 26, 530, doi: 10.1109/TPAMI.2004.1273918

Massari, D., Koppelman, H. H., & Helmi, A. 2019, A&A, 630, L4, doi: 10.1051/0004-6361/201936135

McConnachie, A. W., Irwin, M. J., Ferguson, A. M. N., et al. 2005, MNRAS, 356, 979, doi: 10.1111/j.1365-2966.2004.08514.x

McIlhagga, W. 2018, Vision Research, 153, 30, doi: 10.1016/j.visres.2018.09.007

McKee, C. F., & Ostriker, E. C. 2007, ARA&A, 45, 565, doi: 10.1146/annurev.astro.45.051806.110602

McKinney, W. 2010, in Proceedings of the 9th Python in Science Conference, ed. Stéfan van der Walt & Jarrod Millman, 56 – 61, doi: 10.25080/Majora-92bf1922-00a

Meidt, S. E., Schinnerer, E., García-Burillo, S., et al. 2013, ApJ, 779, 45, doi: 10.1088/0004-637X/779/1/45

Meidt, S. E., Glover, S. C. O., Kruijssen, J. M. D., et al. 2020, ApJ, 892, 73, doi: 10.3847/1538-4357/ab7000

Meier, D. S., & Turner, J. L. 2004, AJ, 127, 2069, doi: 10.1086/382904

Meisner, A. M., Lang, D., Schlafly, E. F., & Schlegel, D. J. 2022, Research Notes of the American Astronomical Society, 6, 188, doi: 10.3847/2515-5172/ac913e

Menon, S. H., Grasha, K., Elmegreen, B. G., et al. 2021, MNRAS, 507, 5542, doi: 10.1093/mnras/stab2413

Messa, M., Adamo, A., Östlin, G., et al. 2018, MNRAS, 473, 996, doi: 10.1093/mnras/stx2403

Miholics, M., Kruijssen, J. M. D., & Sills, A. 2017, MNRAS, 470, 1421, doi: 10.1093/mnras/stx1312

Miville-Deschênes, M.-A., Murray, N., & Lee, E. J. 2017, ApJ, 834, 57, doi: 10.3847/1538-4357/834/1/57

Mouschovias, T. C. 1987, in NATO Advanced Study Institute (ASI) Series C, Vol. 210, Physical Processes in Interstellar Clouds, ed. G. E. Morfill & M. Scholer, 453–489, doi: 10.1007/978-94-009-3945-5_27

Moyano Loyola, G. R. I., Flynn, C., Hurley, J. R., & Gibson, B. K. 2015, MNRAS, 449, 4443, doi: 10.1093/mnras/stv550

Murphy, E. J., Condon, J. J., Schinnerer, E., et al. 2011, ApJ, 737, 67, doi: 10.1088/0004-637X/737/2/67

Murphy, J. W., Khan, R., Williams, B., et al. 2018, ApJ, 860, 117, doi: 10.3847/1538-4357/aac2be

Murray, N., Quataert, E., & Thompson, T. A. 2010, ApJ, 709, 191, doi: 10.1088/0004-637X/709/1/191

Naab, T., & Ostriker, J. P. 2017, ARA&A, 55, 59, doi: 10.1146/annurev-astro-081913-040019

Nguyen, C. T., Costa, G., Girardi, L., et al. 2022, A&A, 665, A126, doi: 10.1051/0004-6361/202244166

Oey, M. S., King, N. L., & Parker, J. W. 2004, AJ, 127, 1632, doi: 10.1086/381926

Olivier, G. M., Lopez, L. A., Rosen, A. L., et al. 2021, ApJ, 908, 68, doi: 10.3847/1538-4357/abd24a

Onodera, S., Kuno, N., Tosaki, T., et al. 2010, ApJL, 722, L127, doi: 10.1088/2041-8205/722/2/L127

Orr, M. E., Hayward, C. C., Hopkins, P. F., et al. 2018, MNRAS, 478, 3653, doi: 10.1093/mnras/sty1241

Ostriker, E. C., McKee, C. F., & Leroy, A. K. 2010, ApJ, 721, 975, doi: 10.1088/0004-637X/721/2/975

Ostriker, E. C., & Shetty, R. 2011, ApJ, 731, 41, doi: 10.1088/0004-637X/731/1/41

Otsu, N. 1979, IEEE Transactions on Systems, Man, and Cybernetics, 9, 62, doi: 10.1109/TSMC.1979.4310076

Padoan, P., Jimenez, R., Juvela, M., & Nordlund, Å. 2004, ApJL, 604, L49, doi: 10.1086/383308

pandas development team, T. 2020, pandas-dev/pandas: Pandas, latest, Zenodo, doi: 10.5281/zenodo.3509134

Pedregosa, F., Varoquaux, G., Gramfort, A., et al. 2011, Journal of Machine Learning Research, 12, 2825

Perets, H. B., & Mastrobuono-Battisti, A. 2014, ApJL, 784, L44, doi: 10.1088/2041-8205/784/2/L44

Péroux, C., & Howk, J. C. 2020, ARA&A, 58, 363, doi: 10.1146/annurev-astro-021820-120014

Peters, T., Klessen, R. S., Mac Low, M.-M., & Banerjee, R. 2010a, ApJ, 725, 134, doi: 10.1088/0004-637X/725/1/134

Peters, T., Mac Low, M.-M., Banerjee, R., Klessen, R. S., & Dullemond, C. P. 2010b, ApJ, 719, 831, doi: 10.1088/0004-637X/719/1/831

Popescu, B., Hanson, M. M., & Elmegreen, B. G. 2012, ApJ, 751, 122, doi: 10.1088/0004-637X/751/2/122

Portegies Zwart, S. F., McMillan, S. L. W., & Gieles, M. 2010, ARA&A, 48, 431, doi: 10.1146/annurev-astro-081309-130834

Prieto, J. L., Kistler, M. D., Thompson, T. A., et al. 2008, ApJL, 681, L9, doi: 10.1086/589922

Ptak, A., Serlemitsos, P., Yaqoob, T., & Mushotzky, R. 1999, ApJS, 120, 179, doi: 10.1086/313179

Rahner, D., Pellegrini, E. W., Glover, S. C. O., & Klessen, R. S. 2017, MNRAS, 470, 4453, doi: 10.1093/mnras/stx1532

Rebolledo, D., Wong, T., Leroy, A., Koda, J., & Donovan Meyer, J. 2012, ApJ, 757, 155, doi: 10.1088/0004-637X/757/2/155

Regan, M. W., & Vogel, S. N. 1995, ApJL, 452, L21, doi: 10.1086/309699

Reina-Campos, M., Kruijssen, J. M. D., Pfeffer, J., Bastian, N., & Crain, R. A. 2018, MNRAS, 481, 2851, doi: 10.1093/mnras/sty2451

Rodríguez, M. J., Baume, G., & Feinstein, C. 2019, A&A, 626, A35, doi: 10.1051/0004-6361/201935291

Rogstad, D. H., & Shostak, G. S. 1972, ApJ, 176, 315, doi: 10.1086/151636

Rosolowsky, E., & Blitz, L. 2005, ApJ, 623, 826, doi: 10.1086/428897

Rubner, Y., & Tomasi, C. 1996, in ARPA Image Understanding Workshop, 927–935

Ryon, J. E., Gallagher, J. S., Smith, L. J., et al. 2017, ApJ, 841, 92, doi: 10.3847/1538-4357/aa719e

San Roman, I., Sarajedini, A., & Aparicio, A. 2010, ApJ, 720, 1674, doi: 10.1088/0004-637X/720/2/1674

Sana, H., de Mink, S. E., de Koter, A., et al. 2012, Science, 337, 444, doi: 10.1126/science.1223344

Sánchez Gil, M. C., Alfaro, E. J., & Pérez, E. 2009, ApJ, 702, 141, doi: 10.1088/0004-637X/702/1/141

Sauty, S., Gerin, M., & Casoli, F. 1998, A&A, 339, 19. https://arxiv.org/abs/astro-ph/9806214

Scalo, J. M. 1985, in Protostars and Planets II, ed. D. C. Black & M. S. Matthews, 201–296

Schaye, J. 2004, ApJ, 609, 667, doi: 10.1086/421232

Schechter, P. 1976, ApJ, 203, 297, doi: 10.1086/154079

Scheepmaker, R. A., Haas, M. R., Gieles, M., et al. 2007, A&A, 469, 925, doi: 10.1051/0004-6361:20077511

Schinnerer, E., Böker, T., Emsellem, E., & Downes, D. 2007, A&A, 462, L27, doi: 10.1051/0004-6361:20066711

Schinnerer, E., Hughes, A., Leroy, A., et al. 2019, ApJ, 887, 49, doi: 10.3847/1538-4357/ab50c2

Schlafly, E. F., & Finkbeiner, D. P. 2011, ApJ, 737, 103, doi: 10.1088/0004-637X/737/2/103

Schmeja, S. 2011, Astronomische Nachrichten, 332, 172, doi: 10.1002/asna.201011484

Schmidt, M. 1959, ApJ, 129, 243, doi: 10.1086/146614

—. 1963, ApJ, 137, 758, doi: 10.1086/147553

Schruba, A., Leroy, A. K., Walter, F., Sandstrom, K., & Rosolowsky, E. 2010, ApJ, 722, 1699, doi: 10.1088/0004-637X/722/2/1699

Seigar, M. S. 2005, Monthly Notices of the Royal Astronomical Society: Letters, 361, L20, doi: 10.1111/j.1745-3933.2005.00056.x

Semenov, V. A., Kravtsov, A. V., & Gnedin, N. Y. 2017, ApJ, 845, 133, doi: 10.3847/1538-4357/aa8096

—. 2019, ApJ, 870, 79, doi: 10.3847/1538-4357/aaf163

Shabani, F., Grebel, E. K., Pasquali, A., et al. 2018, MNRAS, 478, 3590, doi: 10.1093/mnras/sty1277

Shadmehri, M., Nejad-Asghar, M., & Khesali, A. 2010, Astrophysics and Space Science, 326, 83, doi: 10.1007/s10509-009-0210-8

Shivaei, I., Reddy, N. A., Shapley, A. E., et al. 2015, ApJ, 815, 98, doi: 10.1088/0004-637X/815/2/98

Shu, F. H., Adams, F. C., & Lizano, S. 1987, ARA&A, 25, 23, doi: 10.1146/annurev.aa.25.090187.000323

Silk, J. 1997, ApJ, 481, 703, doi: 10.1086/304073

Silva-Villa, E., Adamo, A., Bastian, N., Fouesneau, M., & Zackrisson, E. 2014, MNRAS, 440, L116, doi: 10.1093/mnrasl/slu028

Smartt, S. J. 2009, ARA&A, 47, 63, doi: 10.1146/annurev-astro-082708-101737

Smith, M. V., van Zee, L., Salim, S., et al. 2021, MNRAS, 505, 3998, doi: 10.1093/mnras/stab1530

Sobel, I., & Feldman, G. 1968, A 3x3 Isotropic Gradient Operator for Image Processing

Somerville, R. S., & Davé, R. 2015, ARA&A, 53, 51, doi: 10.1146/annurev-astro-082812-140951

Stacy, A., & Bromm, V. 2013, MNRAS, 433, 1094, doi: 10.1093/mnras/stt789

Stacy, A., Bromm, V., & Lee, A. T. 2016, MNRAS, 462, 1307, doi: 10.1093/mnras/stw1728

Sun, J., Leroy, A. K., Schruba, A., et al. 2018, ApJ, 860, 172, doi: 10.3847/1538-4357/aac326

Susa, H. 2013, ApJ, 773, 185, doi: 10.1088/0004-637X/773/2/185

Tacconi, L. J., Genzel, R., & Sternberg, A. 2020, Annual Review of Astronomy and Astrophysics, 58, 157, doi: https://doi.org/10.1146/annurev-astro-082812-141034

Tan, J. C. 2000, ApJ, 536, 173, doi: 10.1086/308905

Tassis, K., & Mouschovias, T. C. 2004, ApJ, 616, 283, doi: 10.1086/424901

Thilker, D. A., Whitmore, B. C., Lee, J. C., et al. 2022, MNRAS, 509, 4094, doi: 10.1093/mnras/stab3183

Tinsley, B. M. 1980, FCPh, 5, 287, doi: 10.48550/arXiv.2203.02041

Toomre, A. 1964, ApJ, 139, 1217, doi: 10.1086/147861

Tran, D., Tuttle, S. E., Kadlec, K., et al. 2022, Journal of Astronomical Telescopes, Instruments, and Systems, 8, 045004, doi: 10.1117/1.JATIS.8.4.045004

Tran, D., Williams, B., Levesque, E., et al. 2023, ApJ, 954, 211, doi: 10.3847/1538-4357/aced44

Tsai, C.-W., Turner, J. L., Beck, S. C., Meier, D. S., & Wright, S. A. 2013, ApJ, 776, 70, doi: 10.1088/0004-637X/776/2/70

Turner, J. A., Dale, D. A., Lee, J. C., et al. 2021, MNRAS, 502, 1366, doi: 10.1093/mnras/stab055

van der Walt, S., Schönberger, J. L., Nunez-Iglesias, J., et al. 2014, PeerJ, 2, e453, doi: 10.7717/peerj.453

Veilleux, S., Cecil, G., & Bland-Hawthorn, J. 2005, ARA&A, 43, 769, doi: 10.1146/annurev.astro.43.072103.150610

Virtanen, P., Gommers, R., Oliphant, T. E., et al. 2020, Nature Methods, 17, 261, doi: 10.1038/s41592-019-0686-2

Wada, K., Spaans, M., & Kim, S. 2000, ApJ, 540, 797, doi: 10.1086/309347

Wainer, T. M., Johnson, L. C., Seth, A. C., et al. 2022, arXiv e-prints, arXiv:2201.04161. https://arxiv.org/abs/2201.04161

Walch, S., Girichidis, P., Naab, T., et al. 2015, MNRAS, 454, 238, doi: 10.1093/mnras/stv1975

Walch, S. K., Whitworth, A. P., Bisbas, T., Wünsch, R., & Hubber, D. 2012, MNRAS, 427, 625, doi: 10.1111/j.1365-2966.2012.21767.x

Walsh, W., Beck, R., Thuma, G., et al. 2002, A&A, 388, 7, doi: 10.1051/0004-6361:20020467

Ward, J. L., & Kruijssen, J. M. D. 2018, MNRAS, 475, 5659, doi: 10.1093/mnras/sty117

Ward, J. L., Kruijssen, J. M. D., & Rix, H.-W. 2020, Monthly Notices of the Royal Astronomical Society, 495, 663, doi: 10.1093/mnras/staa1056

Waskom, M. L. 2021, Journal of Open Source Software, 6, 3021, doi: 10.21105/joss.03021

Webb, J. J., Reina-Campos, M., & Kruijssen, J. M. D. 2019, MNRAS, 486, 5879, doi: 10.1093/mnras/stz1264

Weidner, C., Bonnell, I. A., & Zinnecker, H. 2010, ApJ, 724, 1503, doi: 10.1088/0004-637X/724/2/1503

Weidner, C., & Kroupa, P. 2006, MNRAS, 365, 1333, doi: 10.1111/j.1365-2966.2005.09824.x

Weisz, D. R., Johnson, L. C., Foreman-Mackey, D., et al. 2015, ApJ, 806, 198, doi: 10.1088/0004-637X/806/2/198

Whitcomb, C. M., Sandstrom, K., Murphy, E. J., & Linden, S. 2020, ApJ, 901, 47, doi: 10.3847/1538-4357/abaef6

Whitmore, B. C. 2003, in A Decade of Hubble Space Telescope Science, ed. M. Livio, K. Noll, & M. Stiavelli, Vol. 14, 153–178

Whitmore, B. C., Chandar, R., Bowers, A. S., et al. 2014, AJ, 147, 78, doi: 10.1088/0004-6256/147/4/78

Whitmore, B. C., Chandar, R., & Fall, S. M. 2007, AJ, 133, 1067, doi: 10.1086/510288

Whitmore, B. C., & Schweizer, F. 1995, AJ, 109, 960, doi: 10.1086/117334

Whitmore, B. C., Schweizer, F., Kundu, A., & Miller, B. W. 2002, AJ, 124, 147, doi: 10.1086/340808

Whitmore, B. C., Schweizer, F., Leitherer, C., Borne, K., & Robert, C. 1993, AJ, 106, 1354, doi: 10.1086/116732

Whitmore, B. C., Zhang, Q., Leitherer, C., et al. 1999, AJ, 118, 1551, doi: 10.1086/301041

Whitmore, B. C., Chandar, R., Schweizer, F., et al. 2010, AJ, 140, 75, doi: 10.1088/0004-6256/140/1/75

Whitmore, B. C., Chandar, R., Kim, H., et al. 2011, ApJ, 729, 78, doi: 10.1088/0004-637X/729/2/78

Whitmore, B. C., Chandar, R., Lee, J., et al. 2020, ApJ, 889, 154, doi: 10.3847/1538-4357/ab59e5

Whitmore, B. C., Lee, J. C., Chandar, R., et al. 2021, MNRAS, 506, 5294, doi: 10.1093/mnras/stab2087

Whitmore, B. C., Chandar, R., Rodríguez, M. J., et al. 2023, ApJL, 944, L14, doi: 10.3847/2041-8213/acae94

Williams, B. F. 2003, AJ, 126, 1312, doi: 10.1086/377347

Williams, B. F., Lang, D., Dalcanton, J. J., et al. 2014, Astrophysical Journal, Supplement Series, 215, doi: 10.1088/0067-0049/215/1/9

Wilson, C. D. 1991, AJ, 101, 1663, doi: 10.1086/115796

Wright, N. J. 2020, New Astronomy Reviews, 90, 101549, doi: https://doi.org/10.1016/j.newar.2020.101549

Yadav, J., Das, M., Patra, N. N., et al. 2021, ApJ, 914, 54, doi: 10.3847/1538-4357/abf8c1

Yajima, Y., Sorai, K., Miyamoto, Y., et al. 2021, PASJ, 73, 257, doi: 10.1093/pasj/psaa119

Zapartas, E., de Mink, S. E., Justham, S., et al. 2021, A&A, 645, A6, doi: 10.1051/0004-6361/202037744

Facilities: HST(WFC3/UVIS)

astropy (Astropy Collaboration et al., 2013, 2018, 2022), GeoPandas (Jordahl et al., 2020), Matplotlib (Hunter, 2007), NetworkX (Hagberg et al., 2008), NumPy (Harris et al., 2020), OpenCV (Bradski, 2000), Pandas (McKinney, 2010; pandas development team, 2020), Scikit-Image (van der Walt et al., 2014), Scikit-Learn (Pedregosa et al., 2011), SciPy (Virtanen et al., 2020), Seaborn (Waskom, 2021)

Appendix A

APPENDIX A

This section provides sample tables of the individual age and mass probability distribution functions measured for each cluster/association candidate that were used to calculate the total age and mass distribution of young and massive cluster/association candidates in NGC 6946. The full machine readable tables with full precision will be made available upon the expanded, peer-reviewed publication of Chapter 4 of this dissertation.

Table A.1. Probability Distribution Functions of the Ages of Clusters/Associations

Index	P6.6-6.7	P6.7-6.8	P6.8-6.9	P6.9-7.0	P7.1-7.2	P7.2-7.3	P7.3-7.4	P7.4-7.5
0	0.454	0.241	0.091	0.079	0.038	0.024	0.035	0.038
1	0.386	0.107	0.082	0.082	0.082	0.083	0.083	0.084
2	0.175	0.149	0.120	0.122	0.115	0.104	0.110	0.107
3	0.670	0.290	0.008	0.006	0.006	0.006	0.006	0.006
5	0.217	0.146	0.106	0.106	0.106	0.106	0.106	0.106
6	0.191	0.241	0.126	0.108	0.087	0.082	0.082	0.082

Note. — This table is a sample of the age probability distribution functions of the clusters and associations identified by the algorithm. These individual probability distribution functions were used to calculate the age distribution of the clusters identified in the galaxy. PX.X-Y.Y stands for the probability of the candidate's age being between log(age)=X.X and log(age)=Y.Y for the rightmost eight columns.

Table A.2. Columns of Mass PDF Table

Number	Column Name
0	Index
1	Probability at $\log(\mathrm{Mass}/\mathrm{M}_\odot) = 2.0\text{-}2.05$
2	Probability at $\log(\mathrm{Mass}/\mathrm{M}_\odot) = 2.05\text{-}2.1$
3	Probability at $\log(\mathrm{Mass}/\mathrm{M}_\odot) = 2.1\text{-}2.15$
4	Probability at $\log(\mathrm{Mass}/\mathrm{M}_\odot) = 2.15\text{-}2.2$
5	Probability at $\log(\mathrm{Mass}/\mathrm{M}_\odot) = 2.2\text{-}2.25$
6	Probability at $\log(\mathrm{Mass}/\mathrm{M}_\odot) = 2.25\text{-}2.3$
7	Probability at $\log(\mathrm{Mass}/\mathrm{M}_\odot) = 2.3\text{-}2.35$
8	Probability at $\log(\mathrm{Mass}/\mathrm{M}_\odot) = 2.35\text{-}2.4$
9	Probability at $\log(\mathrm{Mass}/\mathrm{M}_\odot) = 2.4\text{-}2.45$
10	Probability at $\log(\mathrm{Mass}/\mathrm{M}_\odot) = 2.45\text{-}2.5$
11	Probability at $\log(\mathrm{Mass}/\mathrm{M}_\odot) = 2.5\text{-}2.55$
12	Probability at $\log(\mathrm{Mass}/\mathrm{M}_\odot) = 2.55\text{-}2.6$
13	Probability at $\log(\mathrm{Mass}/\mathrm{M}_\odot) = 2.6\text{-}2.65$
14	Probability at $\log(\mathrm{Mass}/\mathrm{M}_\odot) = 2.65\text{-}2.7$
15	Probability at $\log(\mathrm{Mass}/\mathrm{M}_\odot) = 2.7\text{-}2.75$
16	Probability at $\log(\mathrm{Mass}/\mathrm{M}_\odot) = 2.75\text{-}2.8$
17	Probability at $\log(\mathrm{Mass}/\mathrm{M}_\odot) = 2.8\text{-}2.85$
18	Probability at $\log(\mathrm{Mass}/\mathrm{M}_\odot) = 2.85\text{-}2.9$
19	Probability at $\log(\mathrm{Mass}/\mathrm{M}_\odot) = 2.9\text{-}2.95$
20	Probability at $\log(\mathrm{Mass}/\mathrm{M}_\odot) = 2.95\text{-}3.0$

Table A.2 (cont'd)

Number	Column Name
21	Probability at log(Mass/$M_\odot$) = 3.0-3.05
22	Probability at log(Mass/$M_\odot$) = 3.05-3.1
23	Probability at log(Mass/$M_\odot$) = 3.1-3.15
24	Probability at log(Mass/$M_\odot$) = 3.15-3.2
25	Probability at log(Mass/$M_\odot$) = 3.2-3.25
26	Probability at log(Mass/$M_\odot$) = 3.25-3.3
27	Probability at log(Mass/$M_\odot$) = 3.3-3.35
28	Probability at log(Mass/$M_\odot$) = 3.35-3.4
29	Probability at log(Mass/$M_\odot$) = 3.4-3.45
30	Probability at log(Mass/$M_\odot$) = 3.45-3.5
31	Probability at log(Mass/$M_\odot$) = 3.5-3.55
32	Probability at log(Mass/$M_\odot$) = 3.55-3.6
33	Probability at log(Mass/$M_\odot$) = 3.6-3.65
34	Probability at log(Mass/$M_\odot$) = 3.65-3.7
35	Probability at log(Mass/$M_\odot$) = 3.7-3.75
36	Probability at log(Mass/$M_\odot$) = 3.75-3.8
37	Probability at log(Mass/$M_\odot$) = 3.8-3.85
38	Probability at log(Mass/$M_\odot$) = 3.85-3.9
39	Probability at log(Mass/$M_\odot$) = 3.9-3.95
40	Probability at log(Mass/$M_\odot$) = 3.95-4.0
41	Probability at log(Mass/$M_\odot$) = 4.0-4.05

Table A.2 (cont'd)

Number	Column Name
42	Probability at log(Mass/$M_\odot$) = 4.05-4.1
43	Probability at log(Mass/$M_\odot$) = 4.1-4.15
44	Probability at log(Mass/$M_\odot$) = 4.15-4.2
45	Probability at log(Mass/$M_\odot$) = 4.2-4.25
46	Probability at log(Mass/$M_\odot$) = 4.25-4.3
47	Probability at log(Mass/$M_\odot$) = 4.3-4.35
48	Probability at log(Mass/$M_\odot$) = 4.35-4.4
49	Probability at log(Mass/$M_\odot$) = 4.4-4.45
50	Probability at log(Mass/$M_\odot$) = 4.45-4.5
51	Probability at log(Mass/$M_\odot$) = 4.5-4.55
52	Probability at log(Mass/$M_\odot$) = 4.55-4.6
53	Probability at log(Mass/$M_\odot$) = 4.6-4.65
54	Probability at log(Mass/$M_\odot$) = 4.65-4.7
55	Probability at log(Mass/$M_\odot$) = 4.7-4.75
56	Probability at log(Mass/$M_\odot$) = 4.75-4.8
57	Probability at log(Mass/$M_\odot$) = 4.8-4.85
58	Probability at log(Mass/$M_\odot$) = 4.85-4.9
59	Probability at log(Mass/$M_\odot$) = 4.9-4.95
60	Probability at log(Mass/$M_\odot$) = 4.95-5.0
61	Probability at log(Mass/$M_\odot$) = 5.0-5.05
62	Probability at log(Mass/$M_\odot$) = 5.05-5.1

Table A.2 (cont'd)

Number	Column Name
63	Probability at log(Mass/$M_\odot$) = 5.1-5.15
64	Probability at log(Mass/$M_\odot$) = 5.15-5.2
65	Probability at log(Mass/$M_\odot$) = 5.2-5.25
66	Probability at log(Mass/$M_\odot$) = 5.25-5.3
67	Probability at log(Mass/$M_\odot$) = 5.3-5.35
68	Probability at log(Mass/$M_\odot$) = 5.35-5.4
69	Probability at log(Mass/$M_\odot$) = 5.4-5.45
70	Probability at log(Mass/$M_\odot$) = 5.45-5.5
71	Probability at log(Mass/$M_\odot$) = 5.5-5.55
72	Probability at log(Mass/$M_\odot$) = 5.55-5.6
73	Probability at log(Mass/$M_\odot$) = 5.6-5.65
74	Probability at log(Mass/$M_\odot$) = 5.65-5.7
75	Probability at log(Mass/$M_\odot$) = 5.7-5.75
76	Probability at log(Mass/$M_\odot$) = 5.75-5.8
77	Probability at log(Mass/$M_\odot$) = 5.8-5.85
78	Probability at log(Mass/$M_\odot$) = 5.85-5.9
79	Probability at log(Mass/$M_\odot$) = 5.9-5.95
80	Probability at log(Mass/$M_\odot$) = 5.95-6.0

Note. — This table provides the column names to Table A.3 below.

Table A.3. Probability Distribution Functions of the Masses of Clusters/Associations

0	1	2	3	4	5	6	7	8	9	10	11	12	13
0	0	1e-4	0	0	0	0	0	0	1e-4	0	0	1e-4	3e-4
1	0	0	1e-3	0	1e-3	0	1e-3	1e-3	0	0	0	0	0
2	0	0	2e-3	0	2e-3	0	0	0	0	4e-3	2e-3	7e-3	7e-3
3	0	0	0	0	0	0	0	0	0	8e-5	0	9e-5	0
5	3e-3	0	0	3e-3	0	0	0	0	0	3e-3	3e-3	3e-3	0
6	0	2e-3	2e-3	3e-3	2e-3	0	5e-3	5e-3	3e-3	3e-3	3e-3	3e-3	3e-3

Table A.3. Probability Distribution Functions of the Masses of Clusters/Associations - (cont'd)

14	15	16	17	18	19	20	21	22	23	24	25	26	27
3e-4	0	3e-4	3e-4	4e-4	5e-4	2e-4	5e-4	2e-4	2e-4	7e-4	0	2e-3	7e-4
1e-3	1e-3	1e-3	0	3e-3	2e-3	0	1e-3	1e-3	0	0	5e-3	3e-3	0
7e-3	7e-3	7e-3	7e-3	5e-3	2e-2	1e-2	7e-3	7e-3	2e-3	2e-3	9e-3	2e-2	5e-3
9e-5	0	0	0	0	0	0	0	0	1e-4	1e-4	3e-4	0	2e-4
3e-3	3e-3	3e-3	1e-2	3e-3	1e-2	2e-2	5e-2	5e-2	3e-2	3e-2	6e-2	4e-2	4e-2
3e-3	3e-3	1e-2	1e-2	3e-3	7e-3	1e-2	5e-3	5e-3	1e-2	1e-2	1e-2	1e-2	3e-2

Table A.3. Probability Distribution Functions of the Masses of Clusters/Associations - (cont'd)

28	29	30	31	32	33	34	35	36	37	38	39	40	41
1e-3	3e-3	3e-3	1e-3	8e-4	7e-4	4e-4	2e-3	2e-3	2e-3	3e-3	1e-2	9e-3	0.2
1e-2	9e-3	8e-3	8e-3	8e-3	2e-2	2e-2	1e-2	2e-2	2e-2	2e-2	4e-2	5e-2	4e-2
1e-2	2e-2	2e-2	5e-2	7e-2	0.1	9e-2	0.1	0.1	3e-2	1e-2	3e-3	1e-2	1e-2
2e-4	1e-4	1e-4	0	3e-4	4e-4	2e-4	8e-4	5e-4	5e-4	6e-4	1e-3	3e-3	2e-3
5e-2	5e-2	1e-2	0.2	0.2	0.1	2e-2	0	0	0	0	0	0	0
2e-2	2e-2	2e-2	3e-2	3e-2	3e-2	4e-2	5e-2	7e-2	4e-2	0.2	0.1	7e-2	0.1

Table A.3. Probability Distribution Functions of the Masses of Clusters/Associations - (cont'd)

42	43	44	45	46	47	48	49	50	51	52	53	54	55
0.2	0.2	0.1	7e-2	3e-2	3e-2	3e-2	1e-2	8e-3	7e-3	6e-3	3e-3	3e-3	4e-3
9e-2	0.2	0.2	0.2	6e-2	0	3e-3	3e-3	1e-3	0	1e-3	1e-3 0	3e-3	0
8e-3	1e-2	0	1e-2	7e-3	5e-3	8e-3	6e-3	2e-3	5e-3	8e-3	8e-3	2e-3	5e-3
2e-3	2e-3	2e-2	1e-2	8e-2	0.1	0.3	0.4	2e-2	0	0	0	0	0
0	0	0	0	0	0	0	0	0	0	0	0	0	0
0	0	0	0	0	0	0	0	0	0	0	0	0	0

Table A.3. Probability Distribution Functions of the Masses of Clusters/Associations - (cont'd)

56	57	58	59	60	61	62	63	64	65	66	67	68
1e-3	2e-3	3e-3	2e-3	2e-3	2e-3	1e-3	4e-3	1e-3	2e-3	2e-3	4e-3	7e-4
0	0	0	3e-3	3e-3	1e-3	1e-3	1e-3	1e-3	0	2e-3	0	1e-3
6e-3	5e-3	7e-3	3e-3	6e-3	3e-3	1e-2	6e-3	2e-3	8e-3	0	6e-3	0
0	0	0	0	0	0	0	0	0	0	0	0	0
0	0	0	0	0	0	0	0	0	0	0	0	0
0	0	0	0	0	0	0	0	0	0	0	0	0

Table A.3. Probability Distribution Functions of the Masses of Clusters/Associations - (cont'd)

69	70	71	72	73	74	75	76	77	78	79	80
2e-3	3e-3	2e-3	5e-3	2e-3	3e-3	2e-3	1e-3	2e-3	2e-3	1e-3	2e-3
0	2e-3	0	2e-3	0	0	2e-3	2e-3	0	0	0	0
2e-3	4e-3	0	6e-3	3e-3	2e-3	3e-3	3e-3	3e-3	0	4e-3	0
0	0	0	0	0	0	0	0	0	0	0	0
0	0	0	0	0	0	0	0	0	0	0	0
0	0	0	0	0	0	0	0	0	0	0	0

Note. — This table is a sample of the mass probability distribution functions of the clusters and associations identified by the algorithm. These individual probability distribution functions were used to calculate the mass distribution of the clusters identified in the galaxy. Precision has been reduced to one significant figure to save space. Full precision is available in a machine readable table.